Aziz Nasuti

Using geophysical methods to characterize the Møre-Trøndelag Fault Complex, Mid Norway

NTNU – Trondheim
Norwegian University of
Science and Technology

To my wife Kurdistan

Abstract

Møre-Trøndelag Fault Complex (MTFC) is one of the most prominent fault complexes in Scandinavia. The MTFC appears to have controlled the tectonic evolution of Mid Norway and its shelf for the past 400 Myr and has experienced repeated reactivation during Paleozoic (Devonian to Permian), Mesozoic (Jurassic) and presumably Cenozoic times. Geological and geophysical observations demonstrate that the MTFC exerted a strong control in shaping the basins offshore but also in influencing the development of the landscape onshore, and continues today in modifying the regional stress pattern. Regional gravity and aeromagnetic data are used to map regional-scale faults and, in particular, to delineate the main geophysical features related to the MTFC. The advantage of potential field data is to provide an almost continuous coverage and to tie bedrock mapping onshore to seismic interpretation offshore. Potential field transformations were applied to focus on the regional and deep-seated structures in order to extract new geological information. Also the tilt derivative technique (TDR) is applied to gravity and magnetic data with the aim of enhancing linear trends. The results indicate the possible onshore-offshore links of large scale structural elements like the MTFC and late-Caledonian detachments (e.g. Kollstraumen Detachment). The locations of different segments of the MTFC are detected and possible new faults/lineaments are depicted. Correlating petrophysical data with gravity and magnetic maps explains the influence of the MTFC on the deformation and mineralization of bedrock along its strike. In addition, the structural pattern seen in the enhanced lineaments is diagnostic for the sinistral strike-slip movements that are known to have occurred in Devonian time along the MTFC. This confirms the important role of the MTFC in the tectonic setting and geological evolution of Mid Norway.

Regional gravity and aeromagnetic data are used for mapping the MTFC at the regional scale, while new and multidisciplinary geophysical data sets such as 2D resistivity, gravity, magnetic and seismic profiles are utilized to characterize one of the fault zones in a much more focused area. Rock sampling and petrophysical measurements on densities, suceptibilities and seismic velocities constrain the geophysical models. 2D models are built from selected local profiles in order to provide

further insights on the fault characteristics. As a final step, we use the commercial numerical code Flac3D in order to model the development of the observed brittle structures related to the MTFC.

Acknowledgements

Chapter 1. Introduction

1.1 Thesis objectives

The main objective of the thesis work was to study the Møre-Trøndelag Fault Complex (MTFC) with different geophysical methods to unravel its expression in depth. The Møre-Trøndelag Fault Complex is one of the most prominent fault zones in Norway, onshore and offshore (Gabrielsen et al. 1999). The MTFC is considered to be a long-lived structural zone whose tectonic history included sinistral strike slip and normal faulting (Grønlie and Roberts 1989, Watts 2001). The MTFC appears to have exerted a strong influence on the evolution of the offshore basins, in particular in controlling their structural and depositional styles through time (Osmundsen et al. 2006). The MTFC strikes ENE-WSW, paralleling the coastline of south central Norway, and separates the northern North Sea basin system from the deep Mesozoic Møre and Vøring Basins (Doré et al. 1997) (Fig. 1). However the proposed locations of the different segments of the MTFC are mainly based on their topographic expression and on interpolation between very few outcrops of fault cores (e.g. Gabrielsen & Ramberg, 1979, Grønlie & Roberts 1989, Redfield et al. 2004). Therefore, there was a crucial need to improve our knowledge on the geometry (dip and depth) and location of the fault segments of the MTFC in order to further investigate its tectonics.

1.2 Contribution of thesis

The main focus of this study is to characterize the location and depth extension of the MTFC by using potential field data together with seismic and resistivity imaging. Detailed analysis of potential field data helps to evaluate previous interpretations and to shed new lights on the location of the fault segments where they remain unexposed. Lineaments and boundaries of major structures in mid Norway are extracted from gravity and magnetic data, in particular, to examine the possible onshore-offshore links of large scale structural elements. Petrophysical information is utilized in order to link the potential field data with geological structures. Correlating petrophysical data with gravity and magnetic maps potentially explains the influence of the MTFC on the

deformation and mineralisation of bedrock along its strike. In addition, the structural pattern seen in the enhanced lineaments is diagnostic for the sinistral strike–slip movements that are known to have occurred in Devonian times along the MTFC. This confirms the important role of the MTFC in the tectonic setting and geological evolution of Mid Norway.
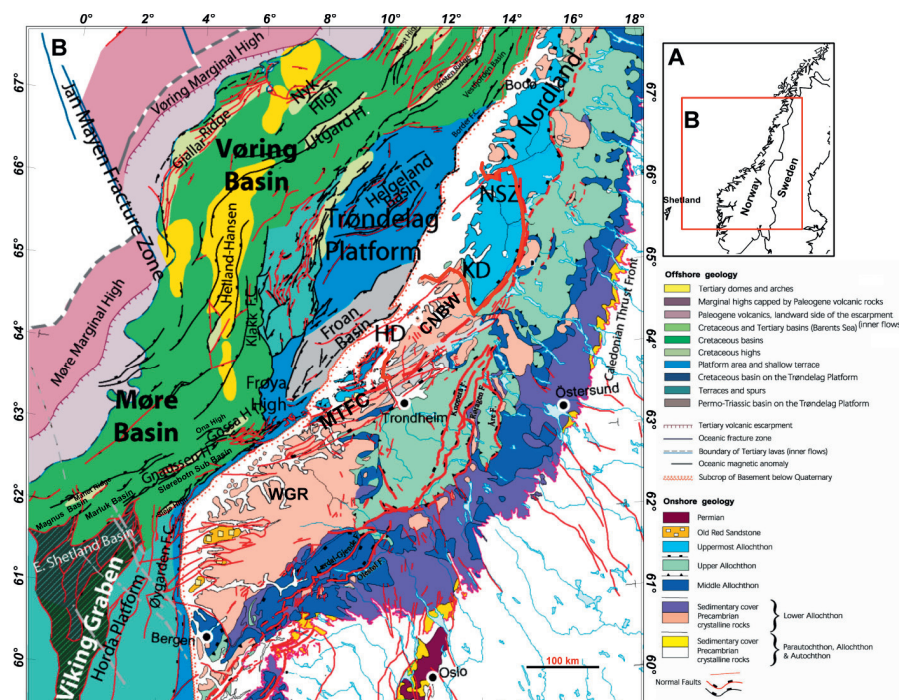
Fig. 1 (A) Location of study area. (B) Tectonic map (modified from Mosar et al. 2002). HD=Høybakken Detachment, KD=Kollstraumen Detachment, NSZ=Nesna Shear Zone, CNBW= Central Norway Basement Window, WGR = Western Gneiss Region.

A set of new geophysical datasets have been acquired across two of the major segments of the MTFC, the so-called Tjellefonna and Bæverdalen faults. Gravity, magnetic, DC resistivity, refraction seismic and reflection seismic data were acquired and jointly interpreted to construct 2D and 3D models along one segment of the MTFC.

The 2D modeling shows that the Tjellefonna fault has a relatively steep dip of 65° towards the south. This is in disagreement with previous interpretations in which a northward dip was assumed for this fault (Redfield and Osmundsen 2009). Furthermore, the newly acquired data revealed the existence of additional fault strands near the

interpreted main fault. In the 3D model, based on seismic and potential field data, a clearer image of the fault is produced. Seismic and 2D resistivity profiles were used to identify highly fractured fault zone in the study area. Seismic travel-time modeling of reflections associated with the fault were used to establish the geometry of the fault structure at depth and detailed analyses of first P-wave arrivals in shot-gathers were used to define the near surface geometry of the fault zone. A continuation to the northern side of the Tingvollfjord is anticipated by correlation of an in strike direction P-S converted reflection (most likely generated by a fracture zone) seen on the reflection data from that side of the Tingvollfjord.

As a final step, a 3D numerical model was constructed in order to model the development of the observed brittle structures related to the MTFC. The results of the following study suggested a new explanation for existing perpendicular structures to the segments of MTFC.

1.3 Thesis layout

The thesis contains seven chapters. A short introduction to the thesis together with a brief overview of the geology of study area is presented in **Chapter 1.**

Chapter 2 gives a short introduction to the fundamentals of the geophysical methods used during the thesis work. The methods are described briefly and the advantages and disadvantages of each geophysical method used to image the faults are discussed.

Application of potential field data for a large scale study of the MTFC and related major structural elements in Mid Norway are discussed in **Chapter 3**. Regional gravity and aeromagnetic data are used to map regional-scale faults and, in particular, to delineate the main geophysical features related to the MTFC. This study has been published in Tectonophysics (Nasuti et al. 2012). The article is based on my own work with support from Christophe Pascal and Jörg Ebbing.

Chapter 4 presents a local scale study of the MTFC. Gravity, magnetic, refraction seismic, and geoelectric data are used to determine the structure of the uppermost 100-200 m around one of the most important faults of the MTFC. A 2D model based on this study is presented and the assumed dip and strike of the studied

fault are discussed. The main effort in this study consists in the integration of multiple geophysical data in order to achieve the most reliable interpretation. This study has been published in Solid Earth (Nasuti et al. 2011). The main work was done by me with support from Christophe Pascal and Jörg Ebbing. Seismic data processing and interpretation was carried out by Jan Fredrik Tønnesen.

Results of the new reflection seismic data in the study area are presented in **Chapter 5**. This chapter is from an article which has been published in Solid Earth (Lundberg et al., 2012). The main contribution to the manuscript, e.g. seismic data processing and interpretation, was done by Emil Lundberg and Chris Juhlin (Uppsala University). My input for this article was, in addition to the participation to the seismic fieldwork, the description of the 2D resistivity profiles and their interpretation.

Chapter 6 presents results from a numerical modelling study. The 3D numerical modeling suggests that the structures perpendicular to the MTFC segments, as suggested by the strike of some fjords, were created by the linkage of the individual segments. This chapter is in preparation for publication, and presents my own work with support from Christophe Pascal.

A summary of the thesis with its main conclusions and recommendations for further studies is provided in **Chapter 7**.

In the **Appendices**, the various data sets acquired in the course of the project are presented. I was involved in the data acquisition for all of the individual data sets and processed most of them.

Refrences:

Doré, A.G., Lundin, E.R., Fichler, C. & Olesen, O. 1997. Patterns of basement structure and reactivation along the NE Atlantic margin. *Journal of the Geological Society, London, 154, 85–92.*

Gabrielsen, R.H. and Ramberg I.B., 1979. Fracture patterns in Norway from LANDSAT imagery: results and potential use. In: Proceedings of the Norwegian Sea Symposium, NSS/20, Tromsø. *Norwegian Petroleum Society (NPF)*, pp. 1-10.

Gabrielsen, R.H., Odinsen, T. and Grunnaleite, I., 1999. Structuring of the Northern Viking Graben and the Møre Basin; the influence of basement structural grain, and the particular role of the Møre-Trøndelag Fault Complex. *Mar. Petrol. Geol., 16: 443-465.*

Grønlie, A. and Roberts, D., 1989. Resurgent strike-slip duplex development along the Hitra-Snåsa and Verran Faults, More- Trøndelag Fault Zone, Central Norway. *J. Struct. Geol.,* 11 (3): 295-305

Lundberg, E., Juhlin, C., and Nasuti, A., 2012. High resolution reflection seismic profiling over the Tjellefonna fault in the Møre-Trøndelag Fault Complex, Norway, *Solid Earth*, 3, 175-188, doi:10.5194/se-3-175-2012.

Nasuti, A., Pascal, C., Ebbing, J. and Tønnesen, J. F., 2011. Geophysical characterisation of two segments of the Møre-Trøndelag Fault Complex, Mid Norway, *Solid Earth,* 2, 125–134.

Nasuti, A., Pascal, C., and Ebbing, J., 2012. Onshore-offshore potential field analysis of the Møre-Trøndelag Fault Complex and adjacent structures of Mid Norway, *Tectonophysics,* 518–521, 17–28.

Osmundsen, P.T., Eide, E., Haabesland, N.E, Roberts, D., Andersen, T.B., Kendrick, M., Bingen, B., Braathen, A., & Redfield, T.F. 2006: Exhumation of the Høybakken detachment zone and the Møre-Trøndelag Fault Complex central Norway. *Journal of the Geological Society London* 163, 303-318.

Redfield, T.F., Torsvik, T.H., Andriessen, P.A.M. & Gabrielsen, R.H. 2004. Mesozoic and Cenozoic tectonics of the Møre Trøndelag Fault Complex, central Norway: constraints from new apatite fission track data. *Physics and Chemistry of the Earth*, 10(29), 673–682.

Redfield, T.F. & Osmundsen, P.T. 2009. The Tjellefonna fault system of western Norway: linking late-Caledonian extension, post-Caledonian normal faulting and Tertiary rock-column uplift with the landslide-generated tsunami event of 1756. *Tectonophysics*, 474, 106–123

Watts, L. M. 2001. The Walls Boundary fault zone and the Møre Trøndelag Fault Complex: a case study of two reactivated fault zones. PhD thesis, University of Durham.

Chapter 2. Introduction to geophysical methods

2.1 Geophysical techniques for fault detection

Our ability to understand geologic structures to a large extent depends on how we perceive them. Few geologic structures have formed by simple processes. Different geophysical methods, each with its own advantages and disadvantages, can be used for fault detection.

Generally, we can classify geophysical surveys into *active* and *passive* surveys. This classification is based on the nature of the applied energy or fields. Geophysical measurements of Earth's natural fields are defined as passive, e.g. gravity and magnetic fields.

Active geophysical surveys require an artificial signal to be generated and injected into the Earth, to be able to measure how it responds to the source signal. Such signals can be ground displacement or variations in electrical currents. Induced polarization, electrical resistivity, and exploration seismics are typical examples of this class. In this thesis refraction and reflection seismics and 2D resistivity have been measured actively.

In the following sub-chapter a brief definition of fault zones and an overview of the applied geophysical methods are given. To enable the analysis in the later chapters, multiple geophysical data sets were acquired and partly processed by myself (gravity, magnetic, 2D resistivity). I will therefore focus on these methods.

2.2 Definition of fault zones

There are three ways by which rocks undergo large deformation (Suppe, 1985): (1) they flow, thereby experiencing a more or less distributed deformation; (2) they buckle or bend, deflecting the rock layers, which allows considerable overall shortening with only moderate internal deformation, or (3) they deform by slip of one body past another along discrete surfaces or zones, with little deformation away from the slip surfaces. These planes or zones of slip are called faults, which are the main focus of this thesis. Large faults within the Earth's crust are the result of differential or shear motion

and active fault zones are the causal locations of most earthquakes. Since faults do not usually consist of a single, clean fracture, the term fault zone is used when referring to the zone of complex deformation that is associated with the fault plane. The two sides of a non-vertical fault are called the hanging wall and footwall (Fig. 1). By definition, the hanging wall occurs above the fault and the footwall occurs below the fault. Faults can be categorized into three groups based on the sense of slip. A fault where the main sense of movement (or slip) on the fault plane is vertical is known as a dip-slip fault (Fig. 1). Where the main sense of slip is horizontal the fault is known as a strike-slip (i.e. lateral) fault. Oblique-slip faults have significant components of both strike and dip slip. For all naming distinctions, it is the orientation of the net dip and sense of slip of the fault which must be considered, not the present-day orientation, which may have been altered by local or regional folding or tilting.
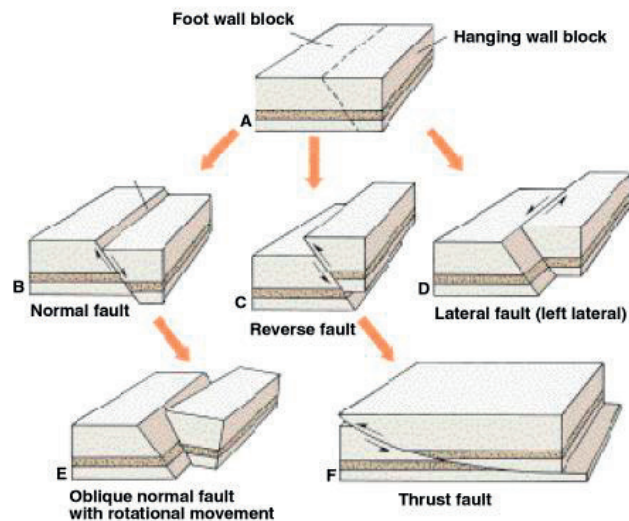
Fig 1. Overview of different fault types (from Levin 2006)

Where the fault type is unknown and cannot be simply characterized at the surface, a suite of different geophysical data sets should be integrated to decrease the inherent ambiguity in the geophysical interpretation. Some methods provide detailed information for shallow depths, e.g. the DC resistivity method, but do not allow tracing the faults farther down, where we have to rely on seismic reflection data.

Gravity and magnetic data in combination with active techniques help to study the dip of the faults. Very steep (near vertical) faults are difficult if not impossible to image with seismic experiments while gravity and magnetic data may show a signal related to a contact anomaly. In addition, regional gravity and magnetic anomaly maps provide a picture of the major geological structures and allow for estimating the thickness of the overburden. However, where basement rocks are relatively close to the surface, the anomalies can often not be correlated with bedrock relief as the effect is strongly influenced by lateral density and susceptibility variations within the bedrock itself (e.g. Overmeeren 1981). In this case only integrated application of several geophysical exploration methods can provide reliable results.

2.3 Gravity

The main purpose of gravity surveys in geophysical exploration is to investigate the gravity field caused by geological structures. The gravitational acceleration due to a subsurface mass (concentration or void) is measured together with the larger acceleration of gravity due to the total mass of the Earth. Therefore, two components of the gravity force are measured at the Earth's surface: first, a relatively uniform and large regional component due to the shape of the Earth and a second component of much smaller size which varies due to lateral, local density changes (the gravity anomaly).

2.3.1 Data acquisition

There are several ways to measure the gravity field of the Earth for example by timing the free fall of an object in a vacuum or measuring the period of a pendulum. However, today almost all gravity surveying is done with gravimeters. In general, there are two types of gravimeters: relative and absolute. Absolute gravimeters measure the actual gravity value for the measured point. The relative gravimeter is designed to measure differences in gravity accelerations rather than absolute magnitudes. This instrument basically consists of a weight on a spring that stretches or contracts corresponding to an increase or decrease in gravity. In each survey the nearest absolute gravity stations should be used to link the relative values to absolute ones. Nowadays, gravimeters used in geophysical surveys have an accuracy of about 0.01 mGal (1 mGal $= 10^{-5} \, m/s^2$) and are capable of detecting small differences in the Earth's gravitational

field which is in the order of 980,000 mGal. The Scintrex CG-3M and LaCoste & Romberg gravimeters that are widely used are shown in Fig.2.
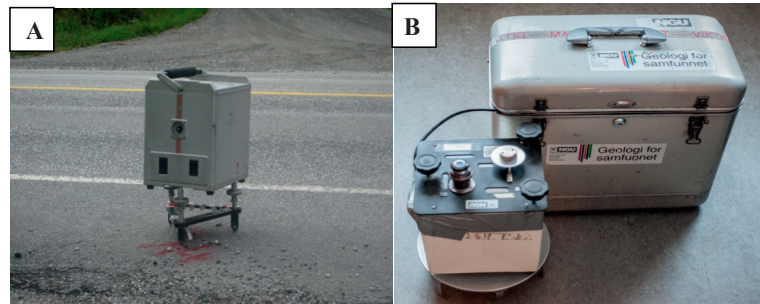
Fig. 2 Gravimeters (A) Scintrex CG-3M, (B) LaCoste & Romberg G.

2.3.2 **Gravity data processing**

In gravity surveying, the subsurface geology is studied by observing variations in the Earth's gravitational field caused by density changes between subsurface rocks. Hereby, it is necessary to correct the measured data for all variations which are not caused by the subsurface rocks, but are from known sources. This process is known as gravity correction or reduction (LaFehr 1991).

2.3.2.1 *Drift correction*

Together with the meter-reading from the gravimeters also the time, height and station location must be registered. Meter-readings are converted to observed gravity (*gobs*) by applying specific meter calibration constants. Afterwards the readings are corrected for tides and the instrument drift. The Earth tide corrections account for the gravitational pull of both the sun and moon and can be calculated for each point on the surface of the Earth (Longman, 1959) . Drift corrections remove the effects of instrument drift during the day (e.g. due to changes in air pressure or battery voltage and also influence of small shocks, and transportation to the sensor system).

The theoretical value of gravity accounts for gravity on the ellipsoid of a rotating Earth. The World Geodetic System 1984 (WGS84) (Blakely 1995) defines normal gravity as:

$$g_0 = 9.7803267714 \left(\frac{1 + 0.00193185138639\sin^2 \lambda}{\sqrt{1 - 0.00669437999013\sin^2 \lambda}} \right)$$

(2.1)

where λ is latitude of the gravity station. The observed gravity values are referenced to the 1971 International Gravity Standardization Net (IGSN71) (Morelli et al., 1974).

2.3.2.2 *Free air anomaly*

The free-air correction accounts for elevation of the station above the ellipsoid (the datum) and assumes no mass between the station and the ellipsoid. This correction is added to the observed gravity because the increased radial distance of the station from the center of the Earth results in a lower observed gravity value than if the station were at the local datum. The free-air correction is given by

$$g_{fa} = -\frac{2g}{r}h_s \qquad (2.2)$$

Where g_{fa} is free-air correction, g is absolute gravity on geoid, r is Earth's radius and h_s is the station elevation. The free-air gradient is not constant, but a mean value of 0.3086 mGalm^{-1} is often used. This must be added to the measured gravity if the gravity station is above the ellipsoid and subtracted if it is below. Application of free-air correction provides the free-air anomaly given by

$$\Delta g_{fa} = g_{obs} - g_{fa} - g_0 \qquad (2.3)$$

where Δg_{fa} is free-air anomaly, g_{obs} is observed gravity and g_0 is normal gravity.

2.3.2.3 *Bouguer anomaly*

The Bouguer correction accounts for the rock mass between the station, and the datum. The simple Bouguer correction approximates all mass above the reference level with a homogeneous, infinitely extended slab of thickness equal to the height of the observation point above the datum given by

$$g_{ba} = 2\pi\gamma\rho h_s \qquad (2.4)$$

where g_{ba} is Bouguer anomaly, γ is gravitational constant, ρ is density of the slab, and h_s is station elevation. By taking into account the simple Bouguer correction, the simple Bouguer anomaly is given by

$$\Delta g_{ba} = g_{obs} - g_{fa} - g_{ba} - g_0 \qquad (2.5)$$

where Δg_{ba} is simple Bouguer anomaly, g_{obs} is observed gravity, g_{fa} is free-air correction, g_{ba} is simple Bouguer correction, and g_0 is normal gravity.

In addition to these corrections, a curvature correction is often applied. The curvature correction corrects for the differences between a spherical and horizontal slab used in the simple Bouguer correction. The curvature correction is based on LaFehr's formula (LaFehr 1991). This correction converts the geometry for the correction from an infinite slab to a spherical cap with a radius of 166.7 km from the station. By taking into account the curvature correction, the Bouguer anomaly becomes:

$$\Delta g_b = \Delta g_{ba} + g_{curv} \qquad\qquad (2.6)$$

where Δg_b is Bouguer anomaly and g_{curv} the curvature correction.

A correct estimate of the Bouguer correction density is very important especially for local studies and in areas of undulating topography. Conventionally, a Bouguer density of 2670 kg/m^3 is used, but this must not be representative of the rock density associated with topographic features. Near-surface density maps for Fennoscandia show that the surface density for most areas is considerably higher (e.g. Korhonen et al. 2002; Ebbing et al. 2012).

Direct determination of density by surface profiling or measurement in boreholes is not feasible for most surveys. Therefore, one has to rely on indirect methods to estimate the most appropriate Bouguer density. In Chapter 4, I use the classical Nettleton method (Nettleton 1939). For a profile several Bouguer anomalies are calculated for different surface densities. The density which produces an anomaly which shows the weakest correlation with the topography is selected as representing the best approximation of the surface density for the study area.

2.3.2.4 *Complete Bouguer anomaly*

The simple Bouguer correction assumes a flat slab of rock between station and datum. If the actual topography surrounding the station is not flat, a terrain correction (TC) must be applied in addition. Topographic highs such as hills, which have mass located above the station, exert a component of acceleration on the station. This causes the value of observed gravity to be less than if the topography is flat, and a correction must be added to the observed gravity at the station. Topographic depressions such as valleys show a lack of rock mass at the station elevation, causing measured gravity to be less than if the area was flat. Therefore terrain corrections for depression features are also added to observed gravity.

Nowadays, the terrain correction is often calculated by the regional terrain correction from a coarse regional Digital Elevation Model (DEM) over a more finely sampled local DEM model that covers the survey area. This produces a regional correction grid that represents terrain correction beyond a local correction distance and this can be re-used to calculate detailed corrections at each observed gravity location. The application of all the preceding corrections results in the complete Bouguer gravity anomaly, as follows:

$$\Delta g_{cb} = \Delta g_b + g_{tc} \qquad\qquad (2.7)$$

where Δg_{cb} is complete Bouguer anomaly, Δg_b is Bouguer anomaly and g_{tc} is terrain correction.

For the thesis work, new gravity points have been measured over the proposed location of one of the segments of the MTFC (see appendix A) and these data are used in combination with magnetic data for geophysical and geological interpretation of the Tjellefonna fault (Chapter 3).

2.4 Magnetic field

There are many similarities between gravity and magnetic field methods. Both are passive geophysical methods and have similar physical and mathematical presentations. Furthermore, the acquisition, reduction and interpretation of gravity and magnetic observations are very similar. However, there are also several considerable differences between the methods. The physical parameter that controls variations in the gravity field is the density with typical values in the range from 1000 to 3000 kg/m^3 for crustal rocks. Magnetisation, as the parameter controlling magnetic field variations, can vary as much as three to four orders of magnitude. Unfortunately, this variation does not only exist between different rock types but there can be wide variation in magnetisation within a given rock type (e.g. Clark et al. 1992, Olesen et al. 1997). Another difference with gravity, which is always attractive, is that the magnetic force can be either attractive or repulsive and no single point sources (monopoles) exist. The magnetic field is best described as a dipole field.

The force F between two magnetic poles of strengths m1 and m2 separated by a distance r is given by equation (2.8) where μ_0 and μ_R are constants corresponding to the

magnetic permeability of vacuum and the relative magnetic permeability of the medium separating the poles. The force is attractive if the poles are of different sign and repulsive if they are of like sign.

$$F = \frac{\mu_0 \, m_1 m_2}{4\pi \mu_R r^2}$$ (2.8)

The magnetic field denoted by B due to a pole of strength m at a distance r from the pole is defined as the force exerted on a unit positive pole at that point.

$$B = \frac{\mu_0 \, m}{4\pi \mu_R r^2}$$ (2.9)

Furthermore, the magnetic field is highly time dependent. Hence, qualitatively and quantitatively data interpretation is more complex than for gravity.

2.4.1 **Earth's magnetic field**

At any point on the Earth's surface, the magnetic field, *F*, has specific strength and direction. The following terms are used to describe the direction of the magnetic field:

Declination - The angle between the geographic north and the horizontal projection of *F* (figure. 2.3). This value is measured positive clockwise and varies from 0 to 360 degrees.

Inclination - The angle between the surface of the Earth and *F* (Fig. 3). Positive inclinations indicate that *F* is pointing downwards; negative inclinations indicate *F* pointing upwards. Declination varies from -90 to 90 degrees.
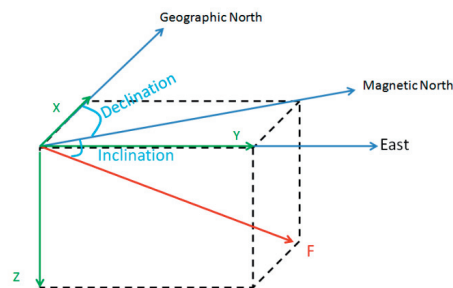
Fig. 3. The geomagnetic elements

Anomalies in the Earth's magnetic field are either caused by induced or remanent magnetism. Induced magnetic anomalies are caused by secondary magnetization induced in body with paramagnetic properties by the Earth's normal

magnetic field. The intensity of magnetization is proportional to the strength of the external magnetic field:

$$M_i = kH \tag{2.10}$$

where M_i is the induced magnetization, H is the external magnetic field and k the magnetic susceptibility. Magnetic susceptibility is the property of a material which determines how much magnetization will be present due to an external magnetic field. The magnetic field B and magnetization force H are related by

$$B = (1 + k)\mu_0 H \tag{2.11}$$

where μ_0 is a constant corresponding to the magnetic permeability of vacuum.

If the rock is placed in a field-free environment, the induced magnetization falls to zero. However, some materials for example ferromagnetic materials also have the ability to retain a magnetization even in the absence of external magnetic fields. This permanent magnetization is called *remanent magnetization (M_r)*. In crustal materials, remanent magnetization is a function not only of the atomic, crystallographic, and chemical make-up of the rocks, but also of their geologic, tectonic, and thermal history (Blakely 1995). The vector sum of induced and remanent magnetizations is called total magnetization

$$M = M_i + M_r \tag{2.12}$$

It is important to know the ratio of remanent to induced magnetization and the direction of remanent magnetization for correct interpretation of magnetic anomalies. This ratio is called *Koenigsberger ratio (Q)* and expressed as:

$$Q = |\frac{M_r}{M_i}| \tag{2.13}$$

2.4.2 Data acqusition

Magnetic surveys can be carried out on land, at sea, and in the air. Since the 1900s a variety of instruments have been designed to measure the geomagnetic field. These instruments are called magnetometers, and some magnetometers can measure the total magnetic field while others measure in addition its orientation and direction.

2.4.3 Magnetic data processing

The magnetic anomalies caused by the subsurface sources are superimposed on the geomagnetic field in the same way that gravity anomalies are superimposed on the

Earth's gravitational field. As discussed briefly, the magnetic case is more complex as the geomagnetic field varies not only in amplitude, but also in direction. Even during measurement time, the magnetic field is not constant, whereas the gravitational field is everywhere vertical and with almost very small changes in comparison with the main acceleration from the whole Earth body. Therefore, it is necessary to remove all magnetic variation from the observed data other than those arising from the magnetic effects of the subsurface.

2.4.4   Magnetic anomaly

Over the Earth's surface, the magnetic field varies markedly from the Equator to the Earth's magnetic poles, thus magnetic data must be corrected for longitude and latitude changes. This correction is done by subtracting the IGRF – International Geomagnetic Reference Field – from the diurnal-corrected data. IGRF is based on measurements around the Earth and revised every five years by taking into account the secular variation of the Earth's magnetic field. The IGRF-corrected data are called total field magnetic anomaly which can be presented either on individual magnetic profiles or gridded data and illustrated as a magnetic anomaly map. The changes in the geomagnetic field are unlikely to be entirely predictable and differences between the predictive IGRF and the true geomagnetic field grow over the course of each epoch. In the long term, the old IGRF models improve by incorporating measured data. Therefore, the geomagnetic field periodically adopts models for past epochs, called Definitive Geomagnetic Reference Field (DGRF) models. DGRF models are not available until data sets will be significantly improved. DGRF models, therefore, become the official record on how the geomagnetic field has evolved in past epochs (Blakely 1995).

2.4.5   Gravity and magnetic field signatures of faults

The shape of a gravity or magnetic anomaly over a fault is depending on its geometry, the density and magnetization contrast with the surrounding bedrock (Fig.1). A detailed discussion on gravity and magnetic anomalies over various fault structures can be found in Prieto (1996). Over a normal fault the typical observed signature is an anomaly with a steep gradient. In the case of the gravity field, the gradient steepens as a fault becomes shallower. The inflection point of the gradient coincides with the center of the fault in map view. In sedimentary regions a magnetic anomaly can be observed if

the basement or a magnetic layer is faulted as shown in Fig. 4. The amplitude of the anomaly depends on both the depth and magnetic susceptibility.
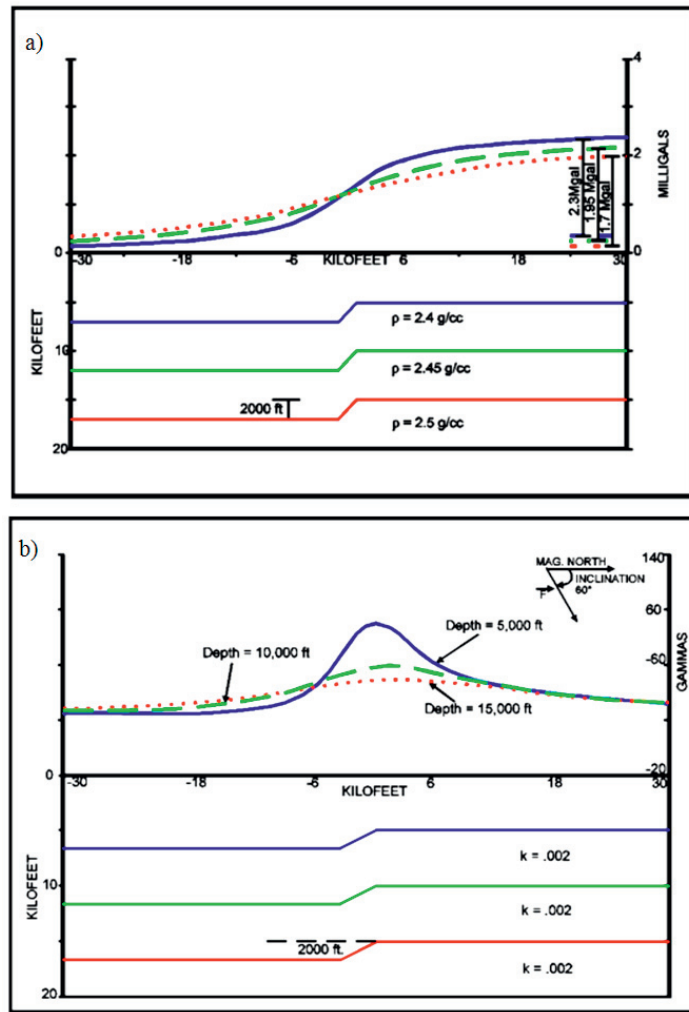
Fig.4 a) Gravity and b) magnetic anomalies with varying depth of a fault structure (after Prieto 1996)

In gravity and magnetic anomaly maps, faults can normally be identified as linear features. If faults offset two different types of rocks, abrupt changes in the magnetic or gravity field signatures may occur.

2.5 Resistivity imaging

2D resistivity imaging, a geoelectrical imaging technique, is a geophysical method often applied in an early stage of underground investigation (e.g. Dahlin et al., 1999; Rønning, 2003; Ganerød et al., 2006). The method has the advantage that measurements are relatively fast and cost-efficient compared to other profiling methods (e.g. refraction seismics). With geoelectrical imaging the spatial variation in subsurface resistivity is measured. The resistivity of geological materials differs greatly from about 10^{-6} Ωm in minerals such as graphite to more than 10^{12} Ωm for dry quartzitic rocks (Reynolds, 1997). Most rock-forming minerals are insulators and so the resistivity of crystalline rock depends largely on the amount and quality of water present and the degree of weathering of the rock. Therefore, rocks without water-bearing fractures or weathering have a high resistivity, whereas clay-weathered rocks or rocks with water-bearing fractures have a considerably lower resistivity (Parasnis 1997, Binley & Kemna, 2005).

The method involves transmission of electric current into the ground between electrodes C1 and C2 (Fig. 5) and measurement of the electrical potential with electrodes P1 and P2 to determine the electrical resistivity of the underground. The most common electrode arrays are Wenner, Schlumberger, pole-pole, pole-dipole, and dipole-dipole array. Recently, the gradient array has gained renewed interest, since it is well suited for multichannel systems. The ratio of voltage to current intensity is the resistance that, when multiplied by a factor taking into account electrode spacing, gives a parameter known as the apparent resistivity. When the measurement is made on a homogeneous medium, the apparent resistivity is equal to the true resistivity of the ground. However, when the measurement is made on a complex subsurface structure, the apparent resistivity is a weighted average of the resistivities of the rocks below the surface. Hence, the resulting apparent resistivity value depends on the structure of the subsurface. Resistivity distributions in the ground can be derived from the measured apparent resistivity values using inverse methods. The convention is to perform a large number of four electrode measurements along profiles or over areas to achieve resistivity models as 2D sections or as 3D volumes, respectively. This is normally done using multi-electrode systems.
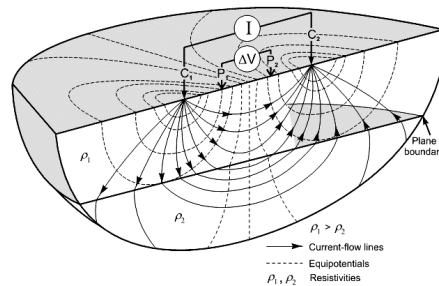
Fig.5 Principles of resistivity measurements (after Knödel et al., 2007)

In general, the imaging depth increases with increasing electrode distance. As a rule of thumb the penetration depth for a Schlumberger array is L/4 where L is the distance between two outermost active current electrodes. For a Wenner array the penetration depth is around L/6 (Loke 2004). However this is only the case if the sub-surface is homogeneous. The current follows the path of least resistance when travelling between the two electrodes. A very low resistive layer near the surface prevents the current from penetrating deeper into the ground. In this case, resolution at depth is limited. By contrast, a very high-resistive layer close to the surface would force the current down in the search of a less resistive layer. The depth of investigation therefore depends very much on the resistivity of the different layers as well as on electrode separation.

Usually resistivity data are measured along 2D profiles. Assuming 2D subsurface can lead to errors by 3D effects, in particular where geology is highly variable on a small scale. In order to obtain the most accurate 2D view, the profiles should be perpendicular to the geological structures.

2.5.1.1 *Processing of the 2D resistivity profiles*

After field surveying, resistance measurements are usually reduced to apparent resistivity values. We processed and inverted the data by using the RES2DINV (version 3.55) software (Loke 2004). Before carrying out the inversion of a data set, one first inspects visually the data in a pseudosection plot as well as on a profile plot. Data points with a high noise level show up as spots with unusually low or high values. In profile form, they stand out from the rest and can be easily removed manually.

2.5.2 **Application of resistivity imaging**

The resistivity method is applicable to various investigations such as groundwater detection, landslide characterization, construction of tunnels and dams, cavity detection, and delineation of subsurface geological structures. Furthermore, it can be used in various stages of an engineering project from reconnaissance through site investigation to maintenance (Reynolds, 1997).

For geological mapping, the method is used for delineation of fractured zones accompanied by faults, classification of weathering and alteration of rocks, and groundwater exploration. Fig. 6 shows a synthetic fault model. In the model the fault seprarates two areas with different resistivity properties. A comparision of different methods for maping faults and fracture zones in the shallow subsurface is discussed by Ganerød et al. (2006). The authors conclude that the resistivity method can give better results compared to other geophysical methods (e.g. VLF and refraction seismic) in terms of detailed mapping of structures in the subsurface. The 2D resistivity profiles were able to detect faults and fracture zones and indicate the respective depths and dip directions of the zones at a lower cost than traditional refraction seismic profiling. A variety of geological models were tested and the imaging possibilities and limitations of the four different arrays, Werner, dipole-dipole, pole-dipole, and Gradient were analysed by Reiser et al., 2009. Apart from imaging fracture zones with various depth, width, contrast and dip, some models for horizontal layers were also examined. Based on their studies the best results were achieved with Gradient and Dipole-dipole, especially for mapping fracture zones with various depth and width. The Gradient configuration gives the best response for mapping steeply dipping structures and different contrasts. In this study Gradient method was used for the 2D resistivity profiling (See appendix B of this thesis).

If the bedrock is fractured or faulted then the fracture zone has generally a lower resistivity value, either because the fracture zone is filled by water which has a dramatically lower resistivity value than fresh bedrock or because the fracture/fault zone is an accumulation space for mineral deposits. This property is useful to find fault locations.
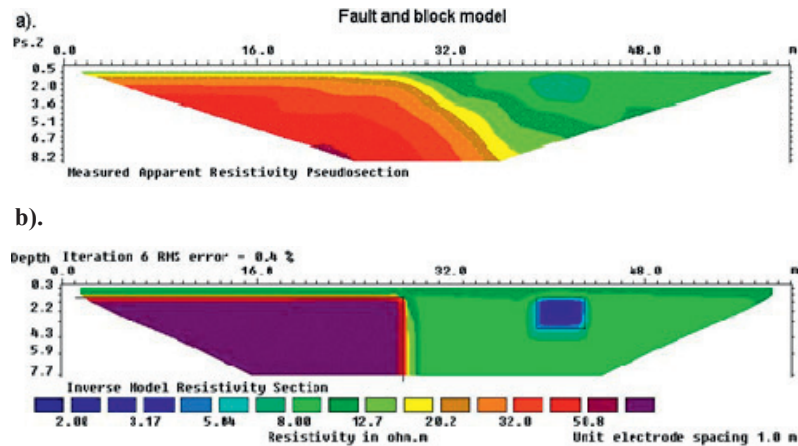
Fig. 6 (a) Apparent resistivity pseudosection (Wenner array) for a synthetic model with a faulted block (100 ohm.m) at the bottom left side and a small rectangular block (2 Ωm) in the right side surrounded by medium with a resistivity of 10 Ωm. (b) Inversion model produced by the Res2Dinv software (Loke, 2004).

2.6 Refraction seismic method

Like geoelectric measurements, seismic experiments are common in exploration geophysics. There are two types of seismic waves that can travel through the underground (i.e. body waves): P-waves (primary) and S-waves (secondary). P-waves are compression waves and travel at higher velocities than S-waves (shear waves). Noteworthy, S-waves are not able to pass through liquids because these materials do not possess shear strength. In addition to P- and S-waves there are two types of seismic waves that can travel along surfaces (i.e. surface waves): Rayleigh and Love waves. These surface waves can travel directly from the shot point to the geophone following the Earth's surface and, in this case, are called direct waves.

Refraction experiments are based on the analysis of arrival times recorded at different distances from the source (Fig. 7). The speed of the seismic waves is controlled by density of the rock and also a set of physical constants called elastic parameters that describe the material. Any change in rock or soil property will cause seismic wave speed to change (Redpath 1973). Usually only travel times of the first arrivals (P-waves) are recorded on each seismogram. When seismic velocity increases

downwards through an interface ($V_2 > V_1$) and the angle of incidence reaches the so-called critical angle, the transmitted P-wave travels along this interface refracting energy back into the upper medium. The interaction of this wave with the layer boundaries produces secondary sources that cause an upgoing wavefront, known as a head or refracted wave (Fig. 7a).

Seismic surveys aim to resolve the thickness and velocity of the rock layers and the depth of investigation depends on source-detector distance. In such surveys, several simplifications and assumptions are usually made: (1) each layer is homogeneous and isotropic (*i.e.,* has the uniform velocity in all directions), (2) the boundaries (interfaces) between layers are nearly planar and (3) each successive layer has higher velocity than the one above. Velocity values determined from time–distance plots depend also on the dip (slope) of the interfaces, apparent velocities increasing when the geophones are up dip from the source and decreasing when they are down dip (Fig. 7c). By measuring in both directions the dip and rock velocity can be determined. With a sufficient number of measurements, the relief on the interfaces separating the layers can also be resolved (Reynolds 1997).

2.6.1 Data acquisition

The purpose of seismic surveys is to record seismics wave (ground motion) caused by a determined source at a known location. The seismic wave may be generated by an explosion, a mechanical vibrator, a dropped weight, a bubble of high-pressure air injected into water, or other sources (Milson 2003). Geophones are used to record seismic waves. A line of geophones laid out for a refraction survey is known as a spread. Sufficient information on the direct wave and reasonable coverage of the refractor is obtained if the length of the spread is about three times the crossover distance.
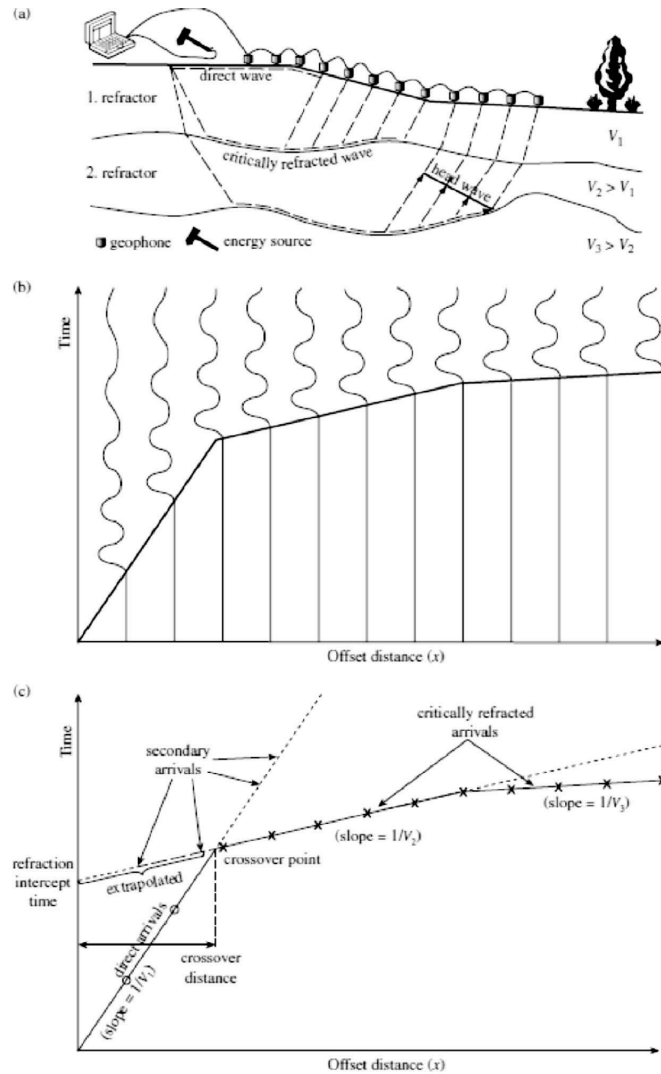
Fig.7 (a) Design of a refraction seismic survey and simplified ray path geometry in a layered subsurface with three layers. (b) Corresponding seismogram resulting from a forward shot close to the first geophone. (c) Time–distance plot of travel times of the first arrivals extracted from the seismogram above (from Hauk and Kneisel 2008).

A simple but often inaccurate rule of thumb states that the spread length should be eight times the expected refractor depth (Milsom 2003). For an efficient processing of seismic data, at least five shots are needed, two shots in the end of each spread, one shot in the center and two shots in the offsets (Fig. 8).
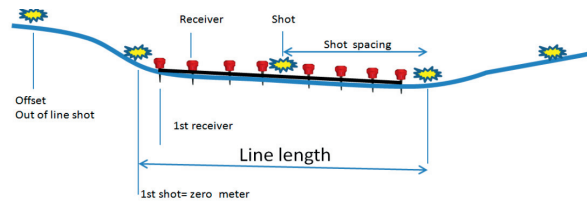
Fig. 8 A typical spread of refraction seismic survey. Five shots are needed at the minimum of a laid out (redrawn from http://www.wgeosoft.ch/Training/documentation.html).

2.6.2 Processing of refraction seismic data

The information used in refraction seismics is the first arrival time information of the P-waves. Picking these first arrivals on refraction records is done by estimation of first break positions. Sometimes it may be difficult to pick the first arrival at remote geophones where the signal-to-noise ratio is poor. However, the distance between the first break and any later peak gradually increases with increasing distance from the source. In some wave forms it is impossible to pick a first arrival and the trace will be neglected. After the first break is picked, the time will be plotted against the distances from the shot points. The gradient of any line which is fitted with plotting points is equal to the reciprocal of a velocity, i.e. steep slopes correspond to slow velocities (Fig. 7).

Refraction seismic can be used on small or large scales to detect fractured or faulted zones. In fractured/faulted zones velocities are lower than in normal bedrock. Fig. 9 shows an example of a small scale refraction seismic survey. The region of the fault zone is distinguishable by its low velocities. Also the top basement is well imaged by the velocity model.
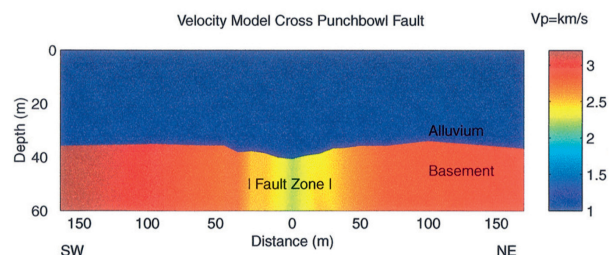
Fig. 9 The cross-fault Vp model for the Punchbowl fault zone. Model parameters were obtained from ray tracing with inverse to best fit observed travel times of P and S waves (from Li et al., 2001).

2.7 **Seismic reflection method**

Most of seismic experiments are seismic reflection studies. The sources and geophones are basically similar to those used for refraction studies. The concept of reflection seismic is very similar to echo sounding: seismic waves are reflected at interfaces where rock properties change and the round-trip travel time, together with velocity information, gives the distance to the interface (Fig. 10). Therefore, by mapping reflections from different locations in the underground, the relief on the interface can be resolved. Also for simple situations one is able to determine the velocity from the change in arrival time as source–geophone distance changes (Reynold 1997). In reality, the seismic reflection method is much more complicated. Reflections from most interfaces are very weak and cannot be easily distinguished from background noise; in addition, reflections from closely-spaced interfaces might be interfering with each other. Conversion of seismic waves, multiple reflections between two reflectors, and interfering of seismic waves from interfaces with different dips makes the reflection seismic method even more complicated (Sheriff 1977).
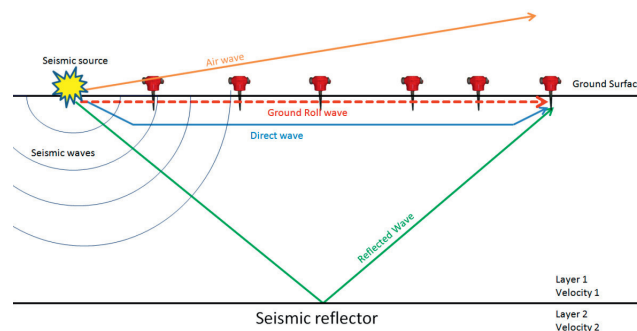
Fig. 10 Schematic diagram of the seismic reflection method (redrawn from http://www.rri-seismic.com)

2.7.1 **Fault determination by means of reflection seismics**

Seismic data can be used to map faults and associated changes in bedrock properties. Fig.11 shows an interpreted seismic profile, where synclinal and anticlinal structures as well as a fault are imaged. Faults are usually detected indirectly (fault planes are generally steep surfaces and so they do not reflect steep travelling seismic waves) by the offset of the reflections across them and/or by the recognition of different reflection patters in oposite blocks of the fault system.

Typically, one has to make a few assumptions to be able to map faults: (1) the data are of a reasonable quality and have been correctly processed, including migration of the data, (2) the two-way-time to depth conversion is known (i.e. a reliable velocity model has been established) and the lines have been interpreted correctly, with all faults tied at line intersections.
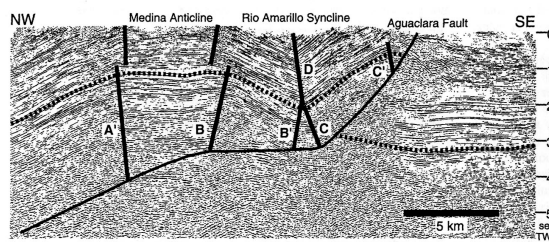
Fig. 11 Interpreted seismic profile for the Aguclara area, Colombia (Tearpock and Bischke 2002)

In areas with complex structures, this may not be possible (Tearpock and Bischke 2002). If these assumptions are met, seismic data can provide the following.

(1) The location of the fault surface. Unlike well data, data from seismic sections cover a series of points along the profile. This enables us to map fault surfaces over a greater area and in areas where no well control exists.

(2) Seismic data can provide a measurement of the throw of a fault.

(3) In many cases, seismic experiments can also provide valuable information about dips and depths of fault segments.

2.8 Comparison of geophysical methods

As previously discussed, different geophysical methods were used in this thesis. Even though the applicability of each method was tested separately in this study, in most cases an additional method is needed to unambiguously interpret the results. The aeromagnetic data are extensively used for fault detection at various scales, especially in the onshore areas. For offshore areas, gravity data appears to be better suited to image fault trends (see chapter 3). Nowadays, large areas are covered by aeromagnetic data and these data are used for preliminary structural interpretations and for planning more

detailed field experiments afterwards. 2D resistivity data can provide more detail in the shallow subsurface but the method cannot image deeper levels in the underground. Refraction seismic surveys generally employ fewer source and receiver locations and are thus relatively cheap. Less processing is needed for refraction seismics and the models and interpretations are not as difficult and complex as for reflection seismics. Furthermore, refraction seismic results are generally interpreted in terms of the dip and topography of the imaged layers. This method is useful if the velocity of the layers increase with depth. Over complex geologic structures reflection seismic has the potential for being more powerful in terms of its ability to provide interpretable observations. In general seismic surveys can detect both lateral and depth variations in physical properties, however data are expensive to acquire and data processing is more complicated than for other geophysical methods. As emphasized in this project the integration of methods is always preferred in order to provide reasonable models. For example, aeromagnetic data together with seismic reflection data can provide a comprehensive 3D view of the complex subsurface structure (Fig.12). The seismic data illustrate the structural complexities in cross section, whereas the aeromagnetic map shows the lateral extent and orientation of the strata that compose the larger structure.
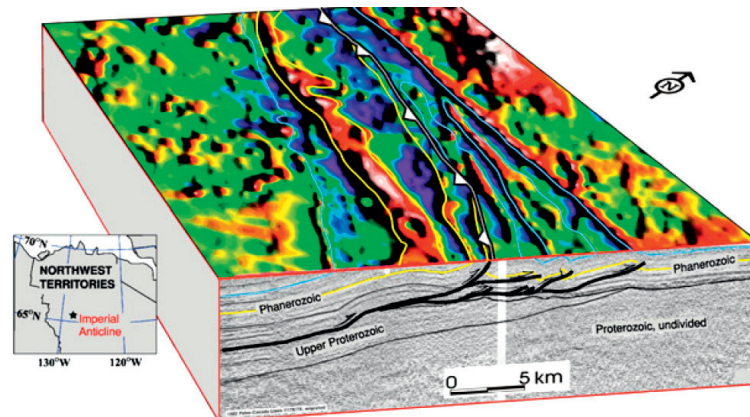
Fig. 12 Block diagram illustrating the relationship between thrust structures and residual magnetic anomalies over part of the Imperial Anticline, Northwestern Territories, Canada. The surface panel shows an image from aeromagnetic data collected by the Geological Survey of Canada (Geological Survey of Canada, 2005). Magnetic anomalies clearly correlate with steeply dipping stratigraphy in the hanging wall of the thrust fault, as identified by seismic-reflection data (MacLean and Cook, 2002), shown in the cross-sectional view. Example compiled by Jim Davies, Image Interpretation Technologies, Inc. (text and figure after Nabighian et al., 2005).

The main characteristics of the different methods discussed before are summarized in Table 1. In addition to the mentioned methods there are other geophysical methods which are used for mapping fault zones (MT and ground penetrating radar). However, these methods have not been applied in this thesis and are therefore not discussed here.

Table 1. Summary of the main characteristics of the geophysical methods discussed above when applied to fault imaging.

	Gravity	Magnetics	Refraction and reflection seismics	Electrical methods
Physical property	Density	Magnetic susceptibility and remanent magnetization	Velocity	Resistivity
Typical units	mGal	nT	m/s	Ohm m
Application	Dip and overburden thickness	Detection of the location of the fault and its dip	Depth of the fault and its dip at deep levels in the underground	Damage zones in the shallow subsurface (about 200 m) and possible dip detection
Measurement time	Short to moderate	Short	Moderate to long	Short to moderate
Cost	Moderate	Low	Moderate to high	Moderate

Refrences:

Binley, A. and Kemna, A., 2005: DC resistivity and induced polarization methods *in* Hydrogeophysics: Rubin, Y. and Hubbard, S., Eds., Springer.

Blakely, R.J. 1995: Potential theory in gravity and magnetic applications: *Cambridge University Press*, 441pp.

Clark, D.A., French, D.H., Lackie, M.A. & Schmidt, P.w., 1992. Magnetic petrology: application of integrated magnetic and petrological techniques to geological interpretation of magnetic surveys. *Exploration Geophysics*, 23, 65-68.

Dahlin, T., Bjelm, L., and Svensson, C., 1999: Use of electrical imaging in site investigations for a railway tunnel through the Hallandsås Horst, Sweden: *Quarterly Journal of Engineering Geology*, 32**,** 163-172.

Ebbing, J., England, R.W., Korja, T., Lauritsen, T., Olesen, O., Stratford, W., Weidle, C., 2012. Structure of the Scandes lithosphere from surface to depth. Tectonophysics, Volumes 536–537 , pp. 1–24.

Ganerød, G. V., Rønning, J.S., Dalsegg, E., Elvebakk, H., Holmøy, K., Nilsen, B. and Braathen, A. 2006: Comparison of geophysical methods for sub-surface mapping of faults and fracture zones in a section of the Viggja road tunnel, Norway. *Bull Eng Geol Env* 65: 231 – 243).

Hauck, C. and Kneisel, C. 2008: Applied geophysics in periglacial environments. Cambridge. *Cambridge University Press*. 240 pp.

Knödel, K., Lange, G., & Voigt, H.-J. (Eds.). (2007). Environmental Geology, Handbook of Field Methods and Case Studies, Springer, ISBN 978-3-540-74669-0, Berlin.

Korhonen, J.V., Aaro, S., All, T., Elo, S., Haller, L.Å., Kääriäinen, J., Kulinich, A., Skilbrei, J.R., Solheim, D., Säävuori, H., Vaher, R., Zhdanova, L., Koistinen, T., 2002. Bouguer anomaly map

of the Fennoscandian Shield 1: 2 000 000. Geological Surveys of Finland, Norway and Sweden and Ministry of Natural Resources of Russian Federation.

LaFehr, T.R 1991: An exact solution for the gravity curvature (Bullard B) correction. *Geophysics* 56, 1179-1184.

Levin, H., 2006. The Earth through Time, 8th edition. John Wiley & Sons, Inc., New York, N.Y.

Li, Y.-G., F. M. Chester, and J. E. Vidale, Shallow seismic profiling of the exhumed Punchbowl fault zone, southern California, *Bull. Seis. Soc. Am.*, 91, 1820-1830, 2001

Loke, M. H., 2004: Tutorial: 2-D *and 3-D electrical imagining surveys*. 136 pp.

Longman, I.M., 1959: Formulas for Computing the Tidal Accelerations Due to the Moon and the Sun. Journal of Geophysical Research, Volume 64, No. 12, 2351 - 2355.

MacLean, B. C., and D. G. Cook, 2002(updated), Subsurface and surface distribution of Proterozoic units, northwestern NWT: a Cambrian sub-crop map: Geological Survey of Canada, Open File 3502.

Milsom, J. 2003. *Field Geophysics,* 3rd Edition. John Wiley & Sons, Chichester, UK.

Morelli, C., ed., 1974, The International Gravity Standardization Net 1971: International Association of Geodesy, Special Publication 4. Moritz, H., 1980, Geodetic Reference System 1980: *Journal of Geodesy*, 54, 395–405.

Nabighian, M. N., V. J. S. Grauch, R. O. Hansen, T. R. LaFehr, Y. Li, J. W. Peirce, J. D. Phillips, and M. E. Ruder, 2005, The historical development of the magnetic method in exploration: *Geophysics*, 70, no. 6, 33ND–61ND.

Nettleton, L. L., 1939. Determination of density for reduction of gravimeter observations: *Geophysics*, 4, 176–183.

Olesen, O., Torsvik, T.H., Tveten, E., Zwaan, K.B., Løseth, H. and Henningsen, T., 1997, Basement structure of the continental margin in the Lofoten-Lopphavet area, northern Norway: constraints from potential field data, onland structural mapping and palaeomagnetic data, Norsk Geologisk *Tidsskrift* 77: 15-30

van Overmeeren, R. A., 1981, A combination of electrical resistivity seismic refraction and gravity measurements for groundwater exploration in Sudan: *Geophysics*, 46, no. 09, 1304-1315.

Parasnis, D. S., 1997: Principles of Applied Geophysics: Chapman and Hall.

Prieto, C. (1996) Gravity/magnetic signatures of various geologic models- An exercise in pattern recognition. *IGC footnote series*, Volume 4, Number 4.

Redpath, Bruce B., 1973: Seismics refraction exploration for engineering site investigations, U.S. Army Engineer Waterways Experiment Station Explosive Excavation Research Laboratory, Technical Report E-73-4, Livermore, California, 51 p.

Reiser, F., Dalsegg, E., Dahlin, T., Ganerød, G. V., and Rønning, J. S., 2009. Resistivity Modelling of Fracture Zones and Horizontal Layers in Bedrock. NGU Report 2009.079, 120 P. http://www.ngu.no/upload/Publikasjoner/Rapporter/2009/2009_070.pdf

Reynolds, J. M., 1997: An Introduction to Applied and Environmental Geophysics: John Wiley & Sons.

Rønning, J.S., Dalsegg, E., Elvebakk, H., & Storrø, G., 2003: Characterization of fracture zones in bedrock using 2D resistivity. 9th EEGS European Meeting, Prague, August 31 – September 4 2003.

Sheriff, R. E., 1977. Limitations on resolution of seismic reflections and geologic detail derivable from them. *In* Payton, C. E. (Ed.), *Seismic Stratigraphy—Applications to Hydrocarbon Exploration*. Am. Assoc. Pet. Geol. Mem., 26:3-14.

Suppe, J. 1985. Principles of Structural Geology. Prentice Hall, New Jersey. 537 pp.

Tearpock, D.J., and Bischke, R.E., 2002, Applied Subsurface Geological Mapping With Structural Methods, 2nd ed., Prentice Hall, NJ, 822pp.

Chapter 3. Paper I. Onshore–offshore potential field analysis of the Møre–Trøndelag Fault Complex and adjacent structures of Mid Norway

Aziz Nasuti [1, 2], Christophe Pascal [2, 3], Jörg Ebbing [1, 2]

[1] Department of Petroleum Engineering and Applied Geophysics, Norwegian University of Science and Technology, 7491 Trondheim, Norway.
[2] NGU, Geological Survey of Norway, 7491 Trondheim, Norway
[3] Institute of Geology, Mineralogy & Geophysics, Ruhr University, Bochum, Germany

ARTICLE INFO

ELSEVIER

TECTONOPHYSICS

ABSTRACT

The Møre–Trøndelag Fault Complex (MTFC) is one of the most prominent fault complexes of Scandinavia. It exerted a strong control on the development of offshore basins of Mid Norway and onshore topography. However, the relationships between the faults observed in the field onshore and those identified by means of seismic profiling offshore remain obscure. Regional gravity and aeromagnetic data are used to map regional-scale faults and, in particular, to delineate the main geophysical features related to the MTFC. The advantage of potential field data is to provide an almost continuous coverage and to tie bedrock mapping onshore to seismic interpretation offshore. In this paper, we apply potential field transformations to focus on the regional and deep-seated structures in order to extract new geological information. Also the tilt derivative technique (TDR) is applied to gravity and magnetic data with the aim of enhancing linear trends. The results indicate the possible onshore–offshore links of large scale structural elements like the MTFC and late-Caledonian detachments (e.g. Kollstraumen Detachment). The locations of different segments of the MTFC are detected and possible new faults/lineaments are depicted. Correlating petrophysical data with gravity and magnetic maps explains the influence of the MTFC on the deformation and mineralisation of bedrock along its strike. In addition, the structural pattern seen in the enhanced lineaments is diagnostic for the sinistral strike–slip movements that are known to have occurred in Devonian time along the MTFC. This confirms the important role of the MTFC in the tectonic setting and geological evolution of Mid Norway.

3.1 **Introduction**

Crustal faults are key elements in attempting to understand the structure and evolution of basins as well as the migration of the hydrocarbons which they may eventually host. Numerous studies have addressed the role of major faults in shaping the Norwegian continental shelf and influencing hydrocarbon systems (e.g. Bukovics and Ziegler, 1985; Caselli, 1987; Gabrielsen et al., 1984, 1999; Lundin and Doré, 1997; Pascal et al., 2002; Vågnes et al., 1998). It has been recognised that most faults of the Mid-Norway shelf and their counterparts onshore Norway have experienced multiple reactivations since at least Caledonian times (e.g. Brekke, 2000; Gabrielsen et al., 1999; Grønlie et al., 1994; Lundin and Doré, 1997). In particular, the continental shelf of Mid Norway (Fig. 1) is a structurally complex area, containing features of different ages, styles and trends. More than thirty years of dense seismic profiling offshore has provided a reliable mean of assessing the impact of the major fault zones on the development of the Mesozoic basins. The origin and pre-Mesozoic history of most of the offshore faults remains speculative because pre-Triassic rocks, including the basement, are in general located at great depths below the thick Mesozoic–Cenozoic cover and difficult to interpret (Brekke, 2000). Onshore mapping constrains to some extent the Palaeozoic evolution of the Mid-Norway shelf and has provided information on the origin and timing of some of the major fault zones (Grønlie et al., 1994; Kendrick et al., 2004; Osmundsen et al., 2002, 2006; Séranne, 1992). However, the relationships between the faults observed in the field onshore and those identifed by means of seismic profiling offshore remain obscure, largely because offshore exploration has been restricted to areas located relatively far away from the coastline. In addition, offshore faults are mainly imaged affecting the sedimentary cover and, as such, it is often difficult to demonstrate whether or not they root deep into the basement and if they are similar to the onshore faults.

The advantage of potential field data is that they provide an almost continuous coverage from the mainland to the offshore and allow us to tie bedrock mapping onshore to seismic interpretation offshore. Furthermore, detailed analysis allows for isolating signals and eventually imaging structures located well below the sediments. Our study focuses on Mid Norway and its adjacent continental shelf (Fig. 1). Previous

authors have used gravity and aeromagnetic data to trace basement structures from the mainland to offshore areas (e.g. Fichler et al., 1999; Olesen et al., 2002; Skilbrei and Olesen, 2005; Skilbrei et al., 2002). However, these previous studies focused mainly on identifying basement units on the Mid-Norway margin. The offshore extensions of the major faults and their mutual structural relationships remain open questions (e.g. Osmundsen and Ebbing, 2008). In this paper, we use tilt derivative techniques on gravity and magnetic field data with the aim of enhancing linear trends. We carefully examine the possible onshore–offshore links of large-scale structural elements such as the Møre–Trøndelag Fault Complex (MTFC), one of the major fault complexes of Mid Norway, and discuss their role in the overall tectonic evolution of the Mid-Norway Margin.
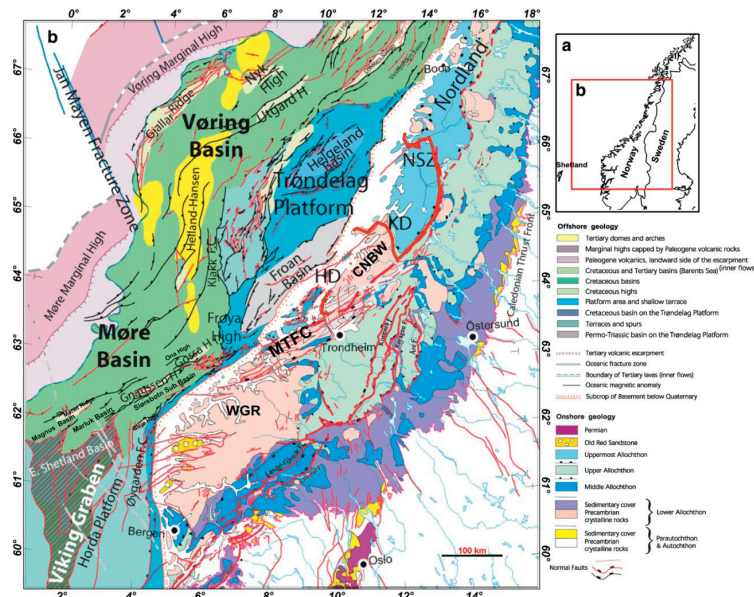
Fig. 1. (a) Location of study area. (b) Simplified geological map (modified from Mosar et al., 2002). HD=Høybakken Detachment, KD=Kollstraumen Detachment, NSZ =Nesna Shear Zone, CNBW =Central Norway Basement Window, WGR =Western Gneiss Region.

3.2 Geological setting

3.2.1 Regional tectonic evolution

Mainland Norway and its continental shelf have most probably experienced a similar geological history until Mesozoic times (e.g. Mosar et al., 2002). The geology

on land in Norway is dominated by Caledonian nappes which also involve allochthonous basement resting on the autochthonous Precambrian basement (Roberts and Gee, 1985), itself exposed in windows like the Western Gneiss Region (WGR, Fig. 1). Farther east, mainly in Sweden this crystalline Precambrian basement is autochthonous. The nappes are composed of a variety of metasedimentary and igneous rocks ranging in age from Palaeoproterozoic to Silurian and were emplaced during the final stages of the Caledonian Orogeny in Late Silurian time (i.e. the Scandian phase). The offshore domain involves several sedimentary basins reflecting different phases of extension (Brekke, 2000). The most important stretching phases occurred in the Devonian, Permo-Triassic and Late Jurassic–Early Cretaceous. The Devonian phase is mainly documented onshore. It corresponds to the collapse of the Caledonian mountain range (Hossack, 1984; Norton, 1986; Séranne and Séguret, 1985, 1987) and was probably followed by a phase of regional rifting (Fossen, 1992). Evidence for Permo-Carboniferous and Permo-Triassic rifting of the Mid-Norway margin is obscured by the thick Cretaceous successions but has been suggested from studies in Greenland, the North Sea, the Barents Sea and the Permian Oslo Graben (Brekke, 2000). The best documented rifting phase occurred in Late Jurassic–Early Cretaceous time and led to the formation of the deep Møre and Vøring basins. Continental breakup finally resumed in earliest Eocene time some 400 km northwest of the present-day coastline.

3.2.2 The Møre–Trøndelag Fault Complex

Remains of down-faulted sedimentary rocks of Devonian and Jurassic ages in coastal areas of Central and Western Norway indicate that some of the present-day onshore faults like the MTFC were reactivated during the different phases of stretching (Bøe, 1991; Bøe and Bjerkli, 1989). The MTFC appears to be one of the most important structures, both onshore and offshore Mid Norway (Bukovics et al., 1984; Gabrielsen and Ramberg, 1979; Oftedahl, 1975), and defines the coastline of Norway between 62° and 64° N. It extends offshore to define the southern margin of the Møre Basin and the northern margin of the Viking Graben (Fig. 1), suggesting that it played an important role in the architecture of these Mesozoic basins (e.g., Gabrielsen et al., 1999). The MTFC is represented offshore by NE–SW to ENE–WSW-trending basement highs and minor basins (Brekke, 2000) whereas ENE–WSW-trending topographic lineaments

outline the fault complex on the mainland. The links between the onshore and the offshore structures remain obscure. The ENE–WSW structural grain of Mid Norway appears to be a feature inherited from the Caledonian continent–continent collision phase (e.g. Hacker et al., 2010). Field evidence shows that this structural grain was subsequently exploited to accommodate ductile sinistral strike–slip in Devonian (Grønlie et al., 1991; Séranne, 1992; Watts, 2001) and normal dip–slip faulting in post-Middle Jurassic times (i.e. presumably Late Jurassic– Early Cretaceous, Bøe and Bjerkli, 1989; Bering, 1992; Grønlie et al., 1994). Reactivation of the MTFC in Permo-Triassic (Grønlie et al., 1994) and Cenozoic (Redfield et al., 2005) time has been proposed but conclusive pieces of evidence for such faulting events are still lacking. The MTFC is moderately active at the present-day and appears to divert contemporary the regional stress field (Pascal and Gabrielsen, 2001; Pascal et al., 2010; Roberts and Myrvang, 2004).

3.3 **Data and methods**

3.3.1 **Potential field data**

Early, large-scale, structural studies of the Norwegian Shelf were mostly based on potential field data (Grønlie and Ramberg, 1970; Talwani and Eldholm, 1972). Since these pioneering studies, the coverage with potential field data has dramatically improved both offshore and on mainland Norway (e.g. Olesen et al., 2010). The gravity data used in this study (Fig. 2a) are based on a compilation by Olesen et al. (2010) and involve a combination of free-air anomalies offshore with Bouguer anomalies onshore. The International Standardization Net 1971 and the Gravity Formula 1980 for normal gravity have been used, and Bouguer and terrain corrections were made using a reduction density of 2670 kg/m^3. The isostatic residual gravity anomaly (Fig. 2b) was calculated to remove the effects of isostatic roots supporting the topography. The isostatic residual gravity anomaly was achieved by subtracting the gravity response of the Airy-Heiskanen root (Heiskanen and Moritz, 1967) from the calculated Bouguer–free-air gravity data. The isostatic correction has been calculated applying the AIRYROOT algorithm (Simpson et al., 1983). The depth of compensation is 30 km with a density contrast of 330 km/m^3 at the Moho. Isostatic residual gravity anomalies

show variations in the gravity field caused by lateral variations in the density of the Earth's crust and upper mantle that reflect variation in composition and thickness (i.e. signals related to changes in the geological structure). Magnetic data (Fig. 2c) are also based on the compilation by Olesen et al. (2010). These data involve a series of surveys over mainland and offshore Norway. The international Geomagnetic Reference Field was calculated and subtracted from the levelled survey lines to produce the magnetic anomaly map.

3.3.2 **Petrophysical data**

The gravity and magnetic anomalies along the coastal zone show their continuation from onshore to offshore (Fig. 2); consequently, there are good reasons to assume that the basement rocks on the continental shelf are similar to those found on the islands and skerries. In this respect, petrophysical measurements on core samples, hand specimens and on in situ bedrock outcrops in the study area provide information about the sources of gravity and magnetic anomalies and facilitate the interpretation of geophysical maps. The Geological Survey of Norway has carried out a petrophysical sampling programme on hand specimens from the Norwegian mainland, as well as on offshore drillcores (e.g. Olesen et al., 2010). To demonstrate the relationship between geology and petrophysical parameters, the density and magnetic susceptibility have been averaged over all major geological units (Fig. 3a and b). Peculiar and non-representative samples (e.g. sulphide mineralisations, hydrothermal alterations, mylonites, dolerites and eclogites) were excluded from the dataset before map production (Olesen et al., 2010). In this study we used these maps to constrain the interpretation of the gravity and magnetic data and utilised them to distinguish between deep and shallow structures. In particular, these maps are conducive to finding sources of gravity and magnetic anomalies along the different segments of the MTFC.

Some care, however, has to be taken while interpreting potential fields together with petrophysical maps. According to these maps (Fig. 3) the WGR is characterised by an average density and magnetic susceptibility of 2700 kg/m^3 and 0.01 SI, respectively. However, gravity and magnetic anomalies are variable over the wide region of the WGR. Noteworthy, in this region the MTFC separates the observed high gravity and magnetic values in the northwest from the relatively low values in the southeast. The

Central Norway Basement Window (CNBW) has susceptibility values similar to those of the WGR but its density is slightly higher (2750 kg/m^3). This latter region, which is bounded by the MTFC to the southeast, has pronounced gravity and magnetic signals. Although there is a very good correlation between surface petrophysics and geophysical data in some regions, mismatches can be found. In southern Nordland (Fig. 2c), for example, a low magnetic anomaly is observed but no marked contrast is seen in the susceptibility map (Fig. 3b). Therefore, not all the anomalies can be explained by surface geology but merely reflect deeper structures. In particular, rocks in Nordland have similar densities than to those of the CNBW (Fig. 3a) but these two regions differ in the amplitude of their respective gravity signals (Fig. 2a).

3.3.3 Data enhancement and filtering

Data-enhancement techniques such as derivative-based filters and shaded-relief imaging have been applied for the analysis of the gravity and magnetic data. Upward continuation (to 1000 m) has been utilised for noise suppression of the aeromagnetic data, and the mainland aeromagnetic data show an error due to manually digitising grids from hand-drawn contours.

It is not a trivial matter to separate shallow sources from magnetic anomalies associated with deeper magnetic sources. To enhance the regional component in magnetic anomalies, we applied the pseudo-gravity transformation (Fig. 2d; Blakely, 1996). Using Poisson's formula, this technique transforms the magnetic field into an equivalent gravity field that would have been produced by a density distribution proportional to the magnetic source. Here, one must assume that (1) magnetisation and density are piecewise constant, and (2) magnetisation is induced and remanence is negligible (Blakely, 1996). It is noteworthy that the oceanic Norway Basin in the north westernmost part of the study area (see Fig. 2c and d) does not satisfy these conditions, but this particular area is not addressed in the present study.

By suppressing short- to medium-wavelength magnetic disturbances, the pseudogravity (PSG) map outlines the main magnetic domains within the study area (Fig. 2d). The PSG map helps to trace the crystalline basement from onshore to offshore and, by comparing with the gravity anomalies, it is possible to obtain further information about the type of basement involved.
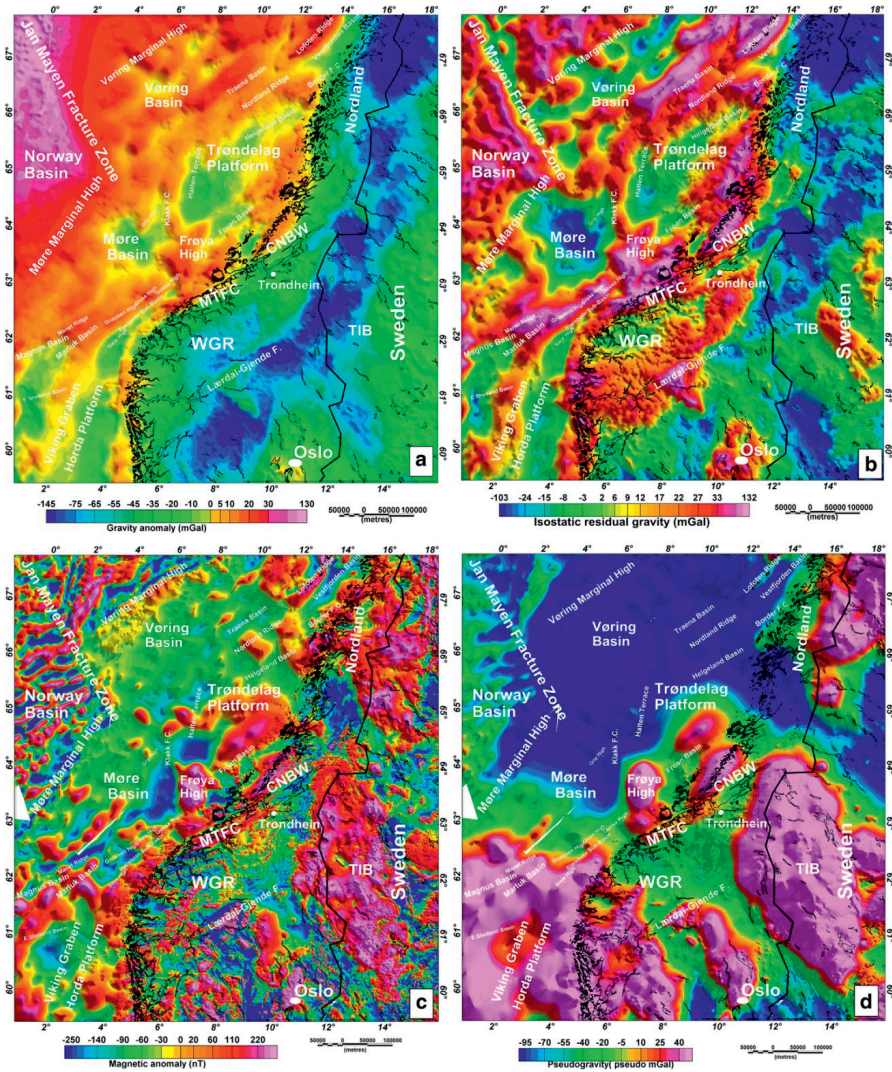
Fig. 2. (a) Bouguer (onshore) and free-air anomalies (offshore). The dataset has been interpolated to a square grid of 2×2 km using a minimum curvature algorithm. (b) Isostatic gravity residual. (c) Total magnetic anomaly after Olesen et al. (2010). (d) Pseudogravity calculated from the magnetic anomalies assuming an inclination of 74° and a declination of 0.2°. CNBW =Central Norway Basement Window, WGR =Western Gneiss Region, MTFC=Møre–Trøndelag Fault Complex, TIB=Transscandinavian Igneous Belt.
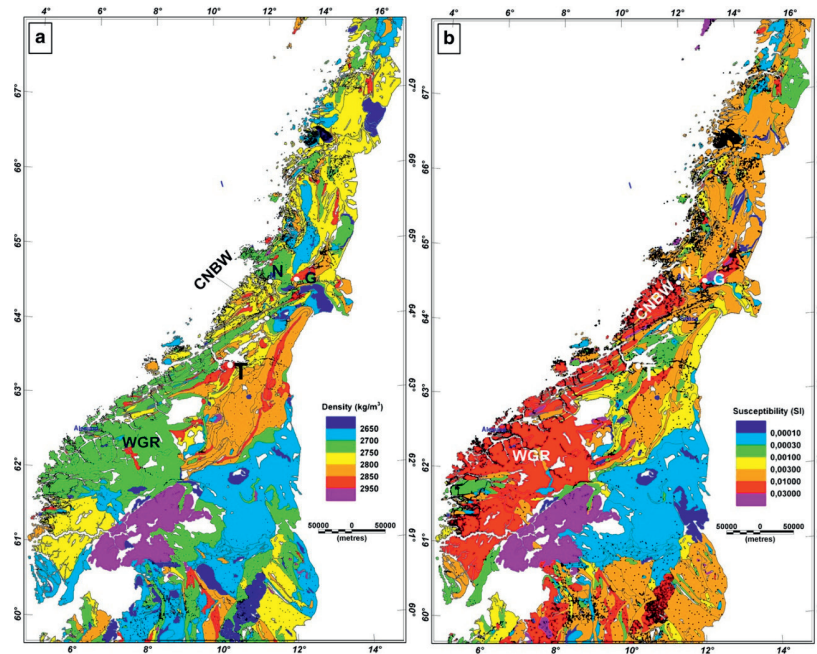
Fig. 3. Petrophysical maps (Olesen et al., 2010). (a) Average density and (b) average magnetic susceptibility of bedrock samples within each geological unit defined by Sigmond(2002).The black dots show sampling locations. CNBW=Central Norway Basement Window, G =Grong, N =Namsos, T=Trondheim, WGR =Western Gneiss.

3.3.4 **Boundary and edge detection**

Edge detection techniques are used routinely in the visual interpretation of both gravity and magnetic maps in order to detect the main geological structures and alignments (e.g. Blakely and Simpson, 1986). Alignment of geophysical anomalies provides information for structural analysis; however, it still remains to be determined whether the magnetic and gravity lineaments correspond to faults, folds or other structural patterns. To this end, we use the tilt derivative method (TDR) in order to enhance the edges of sources. The tilt derivative T is the angle between the total horizontal derivative (x and y directions) and the first vertical derivative and defined after Miller and Singh (1994) as

$$T = \tan^{-1}\left(\frac{\partial f/\partial z}{\sqrt{((\partial f/\partial x)^2 + (\partial f/\partial y)^2)}}\right)$$

where f is the potential field.

Tilt angle responses vary between positive values over the source, zero over or near the edge, and negative values outside the body (Cooper and Cowan, 2006). This sign variation is particularly useful when attempting to detect the relative contrast in magnetisation. The TDR method enhances near-surface features in gravity and magnetic fields. In order to detect deep magnetic sources the method was also applied in the pseudogravity map.

3.4 Results

There is, in general, a good agreement between the boundaries of geological units, showing density and/or susceptibility contrasts along them, and TDR lineaments (Fig. 8). At the edge of units with contrasting densities it is easy to identify TDR lineaments which run parallel to contact boundaries. Comparison of magnetic lineaments with the susceptibility map shows that many of the linear features are concentrated along the faults and fold structures. For example, north of Trondheimsfjorden, the Hitra–Snåsa Fault is located on the northern flank of a ductile antiform with susceptibilities of 0.03 SI, itself separated from rock units with susceptibilities of 0.003 SI and 0.01 SI. Also, rock deformation along the main faults of the MTFC caused changes in petrophysical properties and enhanced their geophysical expression (e.g. the Tjellefonna Fault, Nasuti et al., 2011).

3.4.1 The MTFC in its regional context

In the present section we focus on major regional structures that bound or are related to the MTFC. The reader will find detailed potential field studies on other aspects of the regional geology in e.g. Fichler et al. (1999), Olesen et al. (2002) Skilbrei (1988), and Skilbrei et al. (2002). As already pointed out by previous authors (e.g. Balling, 1980), the gravity anomaly map (Fig. 2a) shows a prominent Bouguer gravity low, aligned approximately along the axis of highest elevation of the Scandinavian (Scandes) mountains, which indicates isostatic compensation at depth. A sharp gravity gradient is observed along the coastline. Offshore, maxima in the gravity field delineate, in general, basement highs (e.g. Frøya High), whereas local minima are observed over very deep basins (e.g. Møre Basin, see also Skilbrei et al., 2002).

The Airy isostatic residual map (Fig. 2b) enhances crustal anomalies better than traditional free-air and Bouguer gravity maps. In this map, the Western Gneiss Region (WGR) and Central Norway Basement window (CNBW), as well as some of the Caledonian nappes are associated with gravity highs. For example, Caledonian nappes east of Trondheim correspond to areas with relatively high densities in the petrophysical data (i.e. in the range of 2750–2850 kg/m^3, compare Fig. 1 with Fig. 3a). The gravity highs offshore generally occur along major faults bounding basement highs. A first-order analysis allows us to distinguish two major structural trends: (1) a (E)NE–(W)SW trend, represented by e.g. the MTFC and the Lofoten and Nordland ridges and (2) a (N)NE–(S)SW trend, represented by, e.g. the Klakk Fault Complex and the Viking Graben. The (E)NE–(W)SW structural trend appears to be the most pronounced and is also distinguishable on the magnetic anomaly map (Fig. 2c) where, in contrast, the (N)NE–(S)SW trend looks more subdued. Onshore, this (E)NE–(W)SW structural trend follows the MTFC and is particularly well expressed in the residual gravity and magnetic maps. Note that the residual gravity highs south of the MTFC correlate with mafic rocks trapped within the different thrust-sheets of the Central Norwegian Caledonides (Skilbrei, 1988).

Two pronounced magnetic highs are discernible on the mainland (Fig. 2c). The first one is located east of Trondheim, mainly in Sweden, and the second one in Nordland. They correspond to the Late Palaeoproterozoic, Transscandinavian Igneous Belt (TIB) (Gaal and Gorbatschev, 1987). The two magnetic bodies have their negative counterparts in the isostatic anomaly map (Fig. 2b), typical for granitoids with low densities but high susceptibilities (e.g. Olesen et al., 2002; Skilbrei et al., 2002). It is noteworthy that a NW–SE trending magnetic low separates these two magnetic high units onshore. The two TIB igneous complexes and also the low-magnetic lineament separating them are particularly well imaged in the pseudogravity map (Fig. 2d). Furthermore, the NW–SE magnetic low apparently continues offshore until the Nordland Ridge. Interestingly enough, the ENE–WSW MTFC appears to reach its easternmost limit near this pronounced NW–SE magnetic low, confirming the geological and structural interpretation (Roberts, 1998) that the fault complex dies out in the horsetail splay across the Grong-Olden Culmination. It is tempting to interpret this NW–SE magnetic low as a Precambrian megashear following the interpretation of

Strömberg (1976) but, alternatively, it could reflect a passive divide between the two regions characterised by the TIB magmatism.

Fig. 4 shows the tilt derivative (TDR) of the gravity anomaly superimposed on the TDR of the pseudogravity map (PSG). Where anomalies coincide, the sources of gravity and magnetic anomalies are most likely related to the same geological object. We superimposed the main structural elements based on seismic interpretation offshore (Blystad et al., 1995) on our combined TDR results. Onshore, colocated anomalies occur mainly just northwest the MTFC (e.g. Central Norway Basement Window, Fig. 4) and represent late Caledonian extensional metamorphic domes (Braathen et al., 2000; Osmundsen et al., 2003) involving high density and high susceptibility rocks (Skilbrei, 1988). We see that co-located anomalies, offshore, coincide with the Frøya High, the structures separating the Froan Basin from the Trøndelag Platform (i.e. Vinleia Fault Complex) and the basement highs trapped within the MTFC (e.g. Ona and Gossa highs; see Fig. 1). We follow previous authors (Ebbing et al., 2009; Skilbrei et al., 2002) and interpret these co-located anomalies as representing basement highs involving high-susceptibility crystalline rocks. Skilbrei et al. (2002) assumed that the anomalies are produced by middle to lower Precambrian crust involved in metamorphic domes that were exhumed during the collapse of the Caledonian mountains (Braathen et al., 2000). However, the basement rocks penetrated by an exploration drillhole on the Frøya High (i.e. well 6407/10-3, Slagstad et al., 2008) were found to be Caledonian granites with no obvious metamorphic foliation. Petrophysical measurements of the core samples resulted in magnetic susceptibility and remanence of 0.01 SI and 0.1 Am^{-1}, respectively (Slagstad et al., 2008). This potentially explains the high-magnetic anomaly over the Frøya high, assuming a direction of remanent magnetisation close to today's induced magnetisation, as has been proposed from a petrophysical analysis of samples of the MTFC onshore (Biedermann, 2010). It is possible that the Frøya High and probably some of the other basement highs offshore are not metamorphic domes similar to the ones observed onshore but rather classical examples of uplifted footwalls of normal faults.

3.4.2   Imaging the Møre–Trøndelag Fault Complex

There is, in general, a good spatial correlation between the TDR of gravity and the major offshore structures (Fig. 5). The TDR map is showing fewer but more linear features in the offshore compared to the onshore part. This is because of the attenuation effect of the sediments covering the basement structures in the offshore domain. A series of anomalies can be followed from onshore to offshore, indicating that the respective sources are located within the crystalline basement. Basement anomalies are seen at the Frøya, Gossa, Selje and Gnausen highs, the Manet Ridge, within the Trøndelag Platform and along the coastline of mainland Norway (Figs. 4 and 5). Some of the anomalies link up with the MTFC on land and with the structural highs over the continental shelf.

In the area of the MTFC, deeply buried Mesozoic rift structures consisting of a series of structural highs and lows (Brekke, 2000) are enhanced by the TDR (Fig. 5). The strike of the lineaments emphasises the MTFC as a key element in the structuring of Mid Norway. South of the MTFC, offshore, the lineaments strike N–S whereas in the northern part up to the Møre Marginal High the lineaments run parallel to the MTFC (Fig. 4). The junction between the MTFC and the Klakk Fault Complex south of the Frøya High appears to be structurally complex and difficult to interpret based on the data on hand.

Onshore-offshore seismic studies of the MTFC are crucially lacking because of the gap in the near-shore coastal areas. An exception is the study of Breivik et al. (2011) but the set up of their seismic experiment was aimed at imaging the structure of the whole crust, and eventual signals related to the MTFC were not recorded. Our analysis shows a curvilinear anomaly southeast of the Frøya High which could represent the offshore prolongation of one of the faults of the MTFC (Fig. 5). This gravity lineament begins in the Grong area, strikes parallel to the Hitra–Snåsa Fault and takes on a curvilinear form close to the island of Hitra. The TDR of pseudogravity (PSG) has been applied in order to image structural boundaries at depth; for example, near the coast, the prolongation of individual structures or domes such as the Central Norwegian Basement Window (CNBW) is well expressed (Fig. 6). Offshore, the TDR of the PSG outlines mainly the crystalline basement.

A good correlation between the results obtained by means of tilt derivative analyses and the geomorphological expression of the fault segments of the MTFC is seen in Figs. 6 and 7. Even second-order structures are imaged in the TDR maps. In detail, the Hitra–Snåsa Fault (HSF, Grønlie and Roberts, 1989) is well imaged on land and its continuation offshore is highlighted by an alignment of high tilt derivative values. The prolongation of the HSF has been imaged by a seismic line just west of Hitra Island, where it also forms a bathymetric step (Osmundsen and Ebbing, 2008) and our interpretation finds firm support in this latter observation. In addition, our analyses suggest that an arm of the HSF exists north of the Slørebotn Sub Basin (Figs. 6 and 7). North of the HSF, another ENE–WSW TDR lineament is imaged. It begins at the northwestern flank of the CNBW and extends offshore between the islands of Frøya and Hitra, where it appears to correspond to the Tarva Fault (Bøe, 1991). This lineament apparently continues westwards through the southern flank of the Frøya High to apparently connect with the southernmost boundary fault of the Møre Basin.

The Verran Fault (Grønlie and Roberts, 1989) is associated with a strong TDR signal (Fig. 5). This is true in particular for its easternmost part where supracrustal units of the Caledonian nappes (i.e. mainly metasedimentary and metavolcanic rocks) are separated from the inferred Precambrian basement by the Verran Fault (Wolff, 1976). No clear offshore prolongation of the Verran Fault can be seen and the fault appears to merge into the Hitra–Snåsa Fault. The Bæverdalen Fault (Nasuti et al., 2011; Redfield et al., 2004) has a strong gravity and magnetic signal and is visible on the TDR map as a prominent lineament extending from Trondheimsfjorden to just southeast of the Slørebotn Sub Basin offshore close to Ålesund. The proposed location of the Bæverdalen Fault (e.g. Blystad et al., 1995; Mosar, 2000) is not completely coinciding with the TDR lineament where it curves more to the north, following the boundary between Caledonian nappes and Proterozoic gneisses. In more detail, east of Tingvoll the lineament is divided into two parts: one part parallel to Fannefjorden and the other one located between the Caledonian nappes and the WGR. TDR analyses of both pseudogravity and magnetic anomalies (Fig. 6a and b) enhance the lineament. South of the Bæverdalen Fault, the Tjellefonna Fault (Nasuti et al., 2011; Redfield and Osmundsen, 2009), which follows a topographic lineament, is also detectable and appears to be located along Langfjorden. From the TDR it can be traced to the offshore

and connects with the end of Bæverdalen Fault east of Ålesund (Fig. 7). The Tjellefonna Fault does not appear to be a continuous lineament in the TDR maps but some discontinuous anomalies are seen in the prolongation of the fault (Fig. 7). These anomalies might be explained by rock deformation related to fault reactivation (Nasuti et al., 2011).
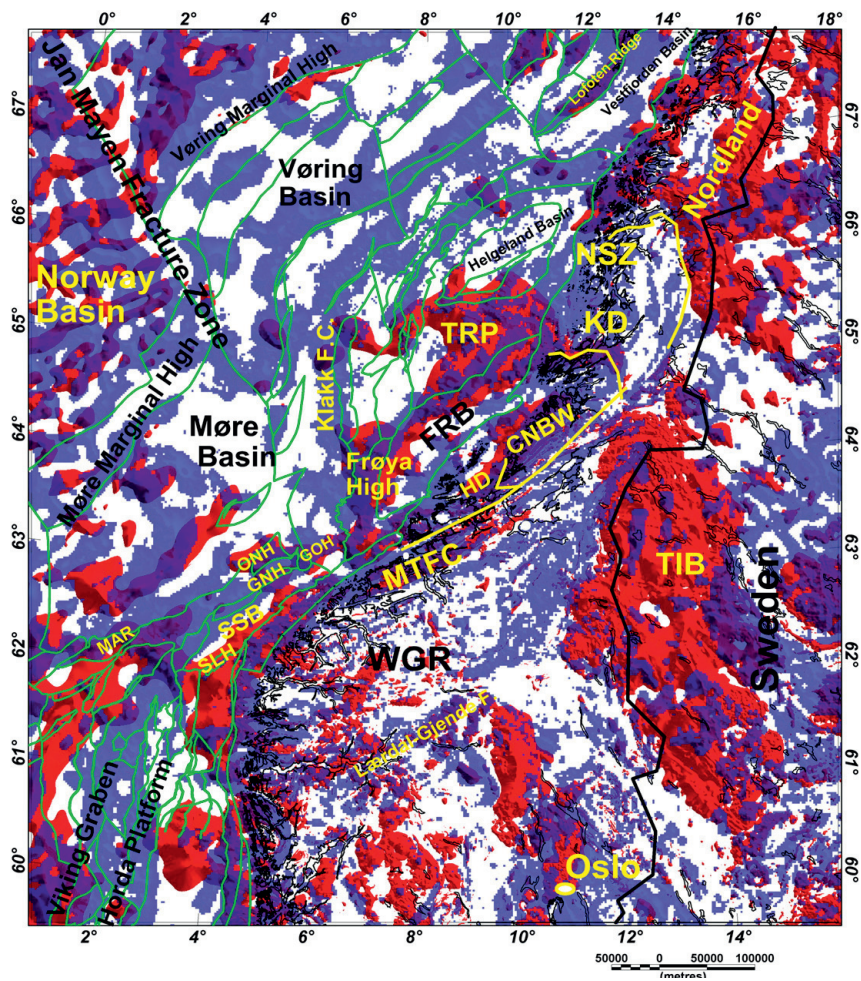
Fig. 4. Tilt derivative (TDR) maps of gravity (blue) and pseudogravity (red). Green lines indicate the main structural elements offshore Norway after NPD. CNBW= Central Norway Basement Window, FRB=Froan Basin, GNH=Gnaussen High, GOH =Gossa High, HD=Høybakken Detachment, KD=Kollstraumen Detachment, MAR=Manet Ridge, MTFC=Møre–Trøndelag Fault Complex, ONH =Ona High, NSZ=Nesna Shear Zone, SLH =Sleje High, SSB =Slørebotn Sub Basin, TIB=Transscandinavian Igneous Belt.

3.4.3   **Discussion**

Important detachments and steep faults affected both the present-day onshore section and the concealed offshore parts of the Caledonides (Braathen et al., 2000; Mosar, 2000; Séranne, 1992). Northeast of the MTFC and north of Grong, the Devonian Nesna Shear Zone (NSZ) and the Kollstraumen Detachment (KD) are mapped on land (e.g., Braathen et al., 2000; Eide et al., 2002; Nordgulen et al., 2002; Osmundsen et al., 2003). In our investigation based on TDR maps (Figs. 6–8), the Nesna Shear Zone is bounded to the north by a pronounced PSG anomaly associated with the TIB, and the Kollstraumen Detachment coincides with the edge of a magnetic anomaly. This anomaly can be traced from the mainland to the western side of the Halten Terrace (Fig. 6a). This is in agreement with previous interpretations based on potential field data suggesting the trace of the offshore prolongation of the KD (e.g. Olesen et al., 2002). However, as pointed out by Breivik et al. (2011), the exact traces of the onshore detachments are extremely difficult to map from potential field data alone and even difficult to image using other kinds of present-day geophysical methods. The TDR of magnetic anomalies depicts lines of local anomalies that connect the MTFC to the NSZ and also prolongs the magnetic high of the TIB to the offshore domain (Fig. 6b). The signals are most probably related to pegmatite and doleritic dykes intruding the northeastern part of the MTFC (Braathen et al., 2000; Watts, 2001).

The structural linkage between the strike–slip MTFC and the extensional NSZ is well imaged in the TDR of the gravity anomalies (Fig. 5). A curvilinear lineament starts from the northeastern part of the MTFC striking N–S and then gradually turns to a NW–SE trend where it extends offshore. This feature can also be observed in the topography.

Comparison of the petrophysical information with the TDR maps shows that lineaments are correlated with the boundaries of different geological units with density and susceptibility contrasts. For example the magnetic lineaments along the Hitra–Snåsa and Verran faults follow geological unit boundaries (Fig. 8). Furthermore, the system of post-Caledonian strike–slip faults proposed by Titus et al. (2002) on Leka Island is consistent with our gravity and magnetic lineaments. In this interpretation; in particular, the horsetail structure imaged at the south of Leka a set of subparallel NE–SW-oriented lineaments can be recognised. These have been suggested to be conjugate faults to the sinistral strike–slip MTFC in Devonian times (Olsen et al., 2007). The geophysical

pattern based on our TDR maps is consistent with this interpretation; in particular, the horsetail structure imaged at the northeastern end of the Hitra–Snåsa Fault is also diagnostic for be recognised. These have been suggested to be conjugate faults to sinistral strike–slip along the MTFC (Fig. 6 and Roberts, 1998).
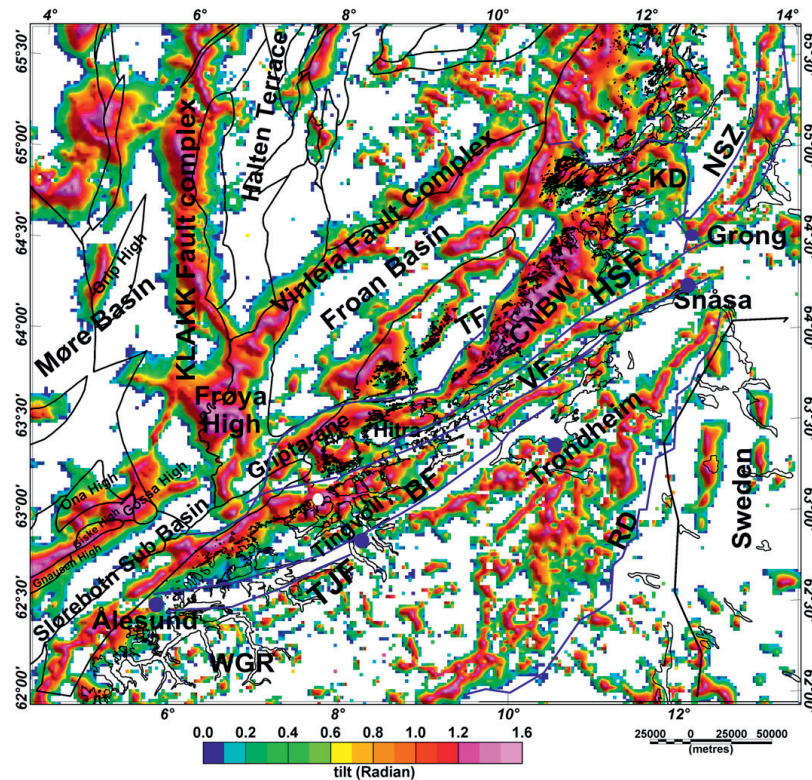
Fig. 5. Tilt derivative (TDR) of gravity anomalies. Only the positive values of TDR are shown (see text for details). Blue lines show the main interpreted faults or detachments as deduced from TDR analysis, black lines are structural elements based on seismic surveys offshore (NPD). BF =Bæverdalen Fault, BB =Beitstadfjorden Basin, CNBW=Central Norway Basement Window, FB =Frohavet Basin, HG=Half Graben, HSF=Hitra–Snåsa Fault, KD=Kollstraumen Detachment, NSZ =Nesna Shear Zone, RD =Røragen Detachment, TF=Tarva Fault, TJF =Tjellefonna Fault, VF=Verran Fault, WGR =Western Gneiss Region.

The southern ends of both the Nesna Shear Zone and the Kollstraumen Detachment form a triple point with the MTFC (Fig. 6b). This triple point is coinciding with the northern tip of the TIB where the Grong–Olden Culmination is located. South of this point and in prolongation of the Verran Fault, some linear features are observed which can be brittle faults. From the TDR lineaments (Fig. 6b) it would appear that the

northeastern tip of the MTFC, the Kopperå Fault (KF) and the Røragen Detachment (RD) system (Andersen, 1998; Mosar, 2000; Norton, 1986), are possibly linked. This would help to explain the curvature of the geological structures in that region. The Hitra–Snåsa Fault bounds the Central Norway Basement Window (CNBW) in which the CNBW is recognised by its high gravity and magnetic values but also by marked lineaments in the TDR (e.g. Fig. 6). A high susceptibility value (0.01 SI) explains the high magnetic signal in this region, and this susceptibility value is in clear contrast to those of the adjacent rocks (i.e. 0.003 SI) (Figs. 6b and 8). The TDR of the gravity (Fig. 5) and magnetic (Fig. 6b) anomalies show the possible continuation of the CNBW to the eastern side of the Frohavet Basin offshore (Bøe, 1991; Sommaruga and Bøe, 2002). The TDR analysis shows that the eastern boundary of the Frohavet Basin coincides with the continuation of the Tarva Fault which limits the Mesozoic half graben present off the coast of Trøndelag (Thorsnes, 1995). This is analogous to the Beitstadfjorden Basin (Bøe and Bjerkli, 1989) which, in turn, is controlled by the Verran Fault. Fig. 7 shows that these basins are bounded by lineaments on the TDR maps that coincide with segments of the MTFC.

The strike of the magnetic lineaments in the CNBW area (Fig. 6) changes from south to north: at the southwestern end, lineaments strike NE–SW, in particular in their offshore prolongation, whereas on the mainland they strike ENE–WSW and north of Namsos they swing toa NW–SE trend. These changes are reflected in the strike of the MTFC segments (e.g. Verran and Hitra–Snåsa faults). A sinistral displacement along the master faults of the MTFC in a pull-apart system explains convincingly the observed lineament pattern as proposed by previous authors based on geological mapping and structural interpretation (e.g., Olsen et al., 2007; Titus et al., 2002).

The TDR of the gravity anomalies (Fig. 5) highlights the possible onshore–offshore links of the MTFC and also suggests that the Klakk Fault Complex (KFC) may crosscut the MTFC. The TDR of the magnetic anomalies (Fig. 6b) enhances prominent high-magnetic anomalies on Griptarane, depicting a sharp boundary in the south parallel to the MTFC and a western edge parallel to the KFC. This anomaly is linked with the Gossa High west of the KFC and the Frøya High, where we propose that the MTFC finds its prolongation to the more distal areas offshore. From this area to the southwestern tip of the CNBW, the lineaments (possible minor faults) that strike ENE–

WSW to E–W are bounded by major faults of the MTFC and are suggestive of a strike–slip system.
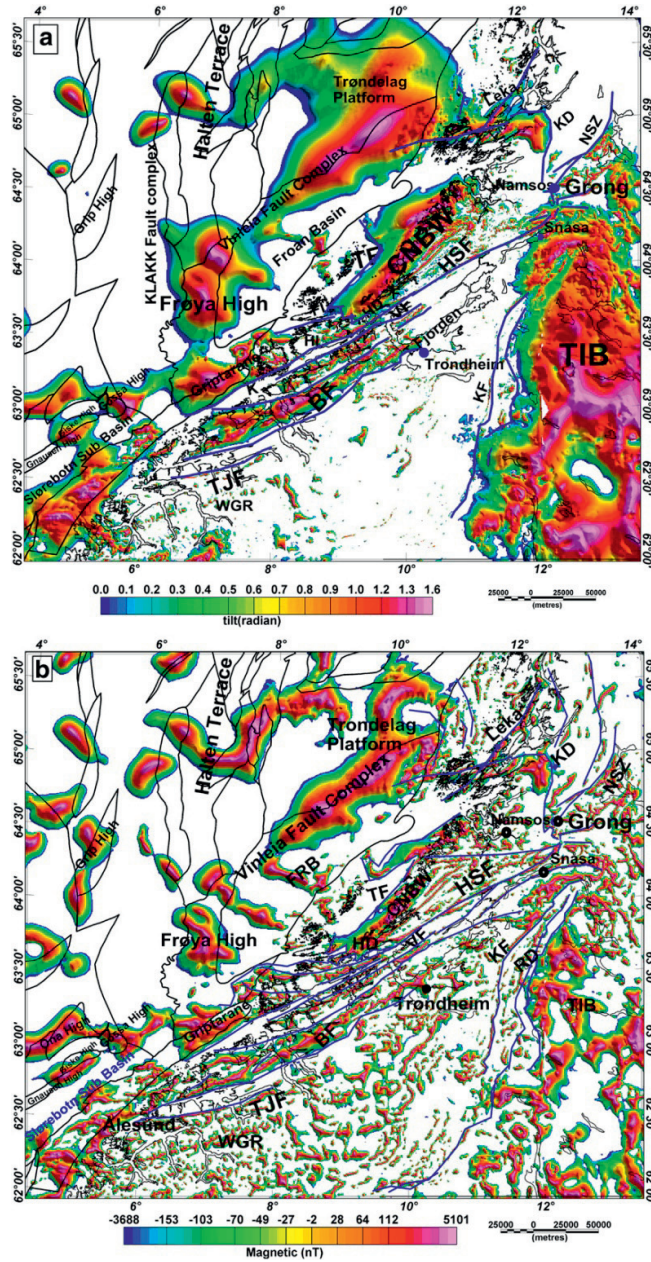
Fig. 6. Tilt derivative of a) pseudogravity and b) magnetic anomalies. See Fig. 5 for details.
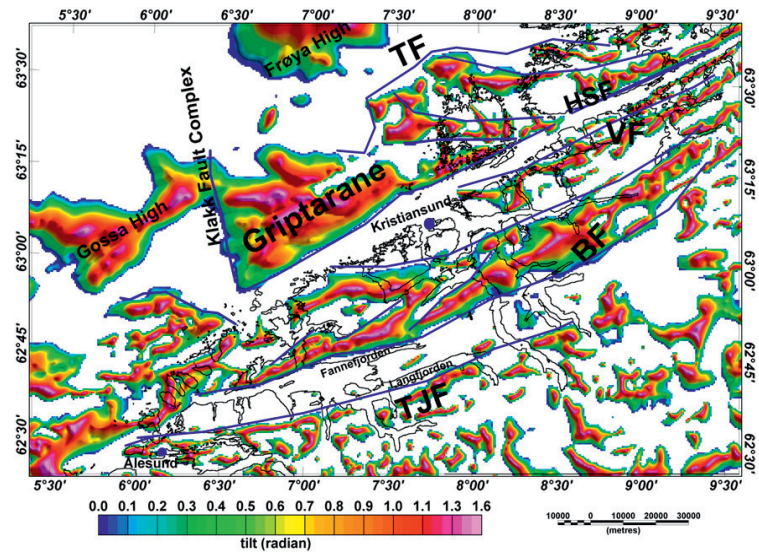
Fig. 7. Tilt derivative of magnetic anomalies over the Møre–Trøndelag Fault Complex. Blue lines show the interpreted faults based on TDR results. BF=Bøverdalen Fault, BB=Beitstadfjorden Basin, HSF =Hitra–Snåsa Fault, HI=Hitra Island, TF=Tarva Fault, TJF =Tjellefonna Fault, VF =Verran Fault.
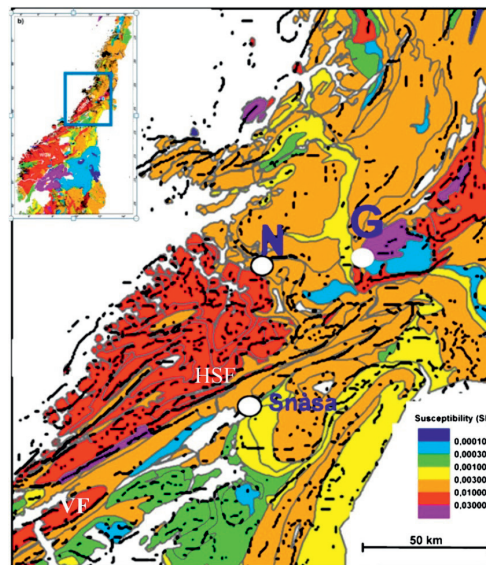
Fig. 8. Magnetic susceptibility map (Olesen et al., 2010) and TDR results. The results of boundary detection by using the TDR of magnetic anomalies are superimposed on the figure (the black dots). These boundaries (edges) of geophysical anomalies are coinciding with the zero value of the TDR of magnetic grids. G=Grong, HSF=Hitra–Snåsa Fault, N=Namsos, VF=Verran Fault.

3.5 Conclusions

The gravity and magnetic maps have been processed and analysed in order to identify the large to medium-scale tectonic structures of Mid Norway, with particular emphasis on the Møre–Trøndelag Fault Complex and the connection between the onshore and offshore domains. The main findings of the study are:

(1) Tilt derivatives of the gravity and magnetic data enabled us to trace the segments of the MTFC from land to the offshore, where these faults have controlled the shape of basins like the Frohavet Basin.

(2) The offshore–onshore link of the MTFC is obscured by the signals of adjacent structures, in particular the Frøya High, in the gravity and magnetic anomalies.

(3) The links between the MTFC and major late-Caledonian extensional structures on the mainland (e.g. Nesna Shear Zone and Kollstraumen Detachment) are well expressed on the TDR maps.

(4) It has been shown that lineament patterns discerned on the gravity and magnetic data can help in the kinematic interpretation of the MTFC (e.g. sinistral strike–slip evidenced by horsetail).

(5) The boundaries of deep-seated structures and geological complexes on the mainland (e.g. TIB) and also in the offshore (e.g. Frøya High) are very well defined by using the TDR of pseudogravity.

(6). Comparison of the tilt derivative (TDR) results with petrophysical data explains the source of the potential field anomalies and assists in our understanding of the spatial relationships between mineralised zones concentrations and geological structures.

References

Andersen, T.B., 1998. Extensional tectonics in the Caledonides of SW Norway: an overview. *Tectonophysics* 285, 333–351.

Balling, N., 1980. The land uplift in Fennoscandia, gravity field anomalies and isostasy. In: Mörner, N.-A. (Ed.), Earth Rheology, Isostasy and Eustasy. Jon Wiley & Sons, New York, pp. 297–321.

Bering, D., 1992. The orientation of minor fault plane striae and the associated deviatoric stress tensor as a key to the fault geometry in part of the Møre–Trøndelag Fault Zone, on-shore central Norway. In: Larsen, R.M., Brekke, H., Larsen, B.T., Talleraas, E. (Eds.), Structural and Tectonic Modelling and its Application to Petroleum Geology: *Norwegian Petroleum Society (NPF)*, Special Publications, 1, pp. 83–90.

Biedermann, A.R., 2010. Magnetic Properties of the Møre–Trøndelag Fault Complex. MSc Thesis, ETH Zürich. http://e-collection.library.ethz.ch/view/eth:1986.

Blakely, R.J., 1996. Potential Theory in Gravity and Magnetic Applications. Cambridge Univ. Press, New York. 441 pp.

Blakely, R.J., Simpson, R.W., 1986. Approximating edges of source bodies from magnetic or gravity anomalies. *Geophysics* 51 (7), 1494–1498.

Blystad, P., Brekke, H., Faerseth, R.B., Larsen, R.B., Skogseid, J., Torudbakken, B., 1995. Structural Elements of the Norwegian Continental Shelf. Part 2: The Norwegian Sea Region. *Norwegian Petroleum Directorate Bulletin* 8.

Bøe, R., 1991. Structure and seismic stratigraphy of the innermost mid-Norwegian continental shelf: an example from the Frohavet area. *Marine and Petroleum Geology* 8, 140–151.

Bøe, R., Bjerkli, K., 1989. Mesozoic sedimentary rocks in Edøyfjorden and Beitstadfjorden, Central Norway: implications for the structural history of the Møre–Trøndelag Fault Zone. *Marine Geology* 87, 287–299.

Braathen, A., Nordgulen, Ø., Osmundsen, P.T., Andersen, T.B., Solli, A., Roberts, D., 2000. Devonian, orogen-parallel, opposed extension in the Central Norwegian Caledonides. *Geology* 28, 615–618.

Breivik, A.J., Mjelde, R., Raum, T., Faleide, J.I., Murai, Y., Flueh, E.R., 2011. Crustal structure beneath the Trøndelag Platform and adjacent areas of the Mid-Norwegian margin, as derived from wide-angle seismic and potential field data. Norwegian Journal of *Geology* 90, 141–161.

Brekke, H., 2000. The tectonic evolution of the Norwegian Sea Continental Margin with emphasis on the Vøring and Møre Basins. In: Nøttvedt, A., et al. (Ed.), Dynamics of the Norwegian Margin: *Geological Society, London*, Special Publications, 167, pp. 327–378.

Bukovics, C., Ziegler, P.A., 1985. Tectonic development of the Mid-Norway continental margin. *Marine and Petroleum Geology* 2, 2–22.

Bukovics, C., Cartier, E.G., Shaw, P.A., Ziegler, P.A., 1984. Structure and development of the Mid-Norway continental margin. In: Society, N.P. (Ed.), Petroleum Geology of the North European Margin. Graham & Trotman, London, pp. 407–423.

Caselli, F., 1987. Oblique-slip tectonics mid-Norwegian shelf. Petroleum Geology of North-west Europe. Graham & Trotman, London, pp. 1049–1063.

Cooper, G.R.J., Cowan, D.R., 2006. Enhancing potential field data using filters based on the local phase. *Computers & Geosciences* 32 (10), 1585–1591.

Ebbing, J., Gernigon, L., Pascal, C., Olesen, O., Osmundsen, P.T., 2009. A discussion of structural and thermal control of magnetic anomalies on the mid-Norwegian margin. *Geophysical Prospecting* 57, 665–681.

Eide, E.A., Osmundsen, P.T., Meyer, G.B., Kendrick, M.A., 2002. The Nesna Shear Zone, North-Central Norway: an 40 Ar/39 Ar record of Early Devonian–Early Carboniferous ductile extension and unroofing. *Norwegian Journal of Geology* 82, 317–339.

Fichler, C., Rundhove, E., Olesen, O., Saether, B.M., Rueslatten, H., Lundin, E., Dore', A.G., 1999. Regional tectonic interpretation of image enhanced gravity and magnetic data covering the Mid-Norwegian shelf and adjacent mainland. *Tectonophysics* 306, 183–197.

Fossen, H., 1992. The role of extensional tectonics in the Caledonides of South Norway. *Journal of Structural Geology* 14, 1033–1046.

Gaal, G., Gorbatschev, R., 1987. An outline of the Precambrian evolution of the Baltic Shield. *Precambrian Research* 35, 15–52.

Gabrielsen, R.H., Ramberg, I.B., 1979. Fracture patterns in Norway from LANDSAT imagery: results and potential use. Proceedings of the Norwegian Sea Symposium, NSS/20, Tromsø. *Norwegian Petroleum Society* (NPF), pp. 1–10.

Gabrielsen, R.H., Færseth, R.B., Hamar, G., Ronnevik, H.C., 1984. Nomenclature of the main structural features on the Norwegian Continental Shelf north of the 62nd parallel. In: Spencer, A.M., et al. (Ed.), Petroleum Geology of the North European Margin. Proceedings of the North European Margin Symposium, Norwegian Petroleum Society, Trondheim, Graham and Trotman, London, pp. 41–60.

Gabrielsen, R.H., Odinsen, T., Grunnaleite, I., 1999. Structuring of the Northern Viking Graben and the Møre Basin; the influence of basement structural grain, and the particular role of the Møre–Trøndelag Fault Complex. *Marine and Petroleum Geology* 16, 443–465.

Grønlie, G., Ramberg, I.B., 1970. Gravity indications of deep sedimentary basins below the Norwegian continental shelf and the Vøring plateau. *Norsk Geologisk Tidsskrift* 50, 374–391.

Grønlie, A., Roberts, D., 1989. Resurgent strike–slip duplex development along the Hitra–Snåsa and Verran Faults, More–Trøndelag Fault Zone, Central Norway. *Journal of Structural Geology* 11 (3), 295–305.

Grønlie, A., Nilsen, B., Roberts, D., 1991. Brittle deformation history of fault rocks on the Fosen Peninsula, Trøndelag, Central Norway. Norges *geologiske undersøkelse Bulletin* 421, 39–57.

Grønlie, A., Naeser, C.W., Naeser, N.D., Mitchell, J.G., Sturt, B.A., Ineson, P., 1994. Fission track and K/Ar dating of tectonic activity in a transect across the Møre–Trøndelag Fault Zone, Central Norway. Norwegian Journal of Geology 74, 24–34.

Hacker, B.R., Andersen, T.B., Johnston, S., Kylander-Clark, A.R.C., Peterman, E.M., Walsh, E.O., Young, D., 2010. High-temperature deformation during continental-margin subduction and exhumation: the ultrahigh-pressure Western Gneiss Region of Norway. *Tectonophysics* 480 (1–4), 149.

Heiskanen, W.A., Moritz, 1967. Physical Geodesy. W.H. Freeman and Co, San Francisco, 181pp.

Hossack, J.R., 1984. The geometry of listric growth faults in the Devonian basins of Sunnfjord, west Norway. Journal of the Geological Society of London 135, 705–711.

Kendrick, M.A., Eide, E.A., Roberts, D., Osmundsen, P.T., 2004. The Mid-Late Devonian Høybakken Detachment, Central Norway: 40Ar/39Ar evidence for prolonged late/ post Scandian extension and uplift. *Geological Magazine* 141, 329–344.

Lundin, E.R., Doré, A.G., 1997. A tectonic model for the Norwegian passive margin with implications for the NE Atlantic: Early Cretaceous to break-up. *Journal of the Geological Society of London* 154 (3), 545–550.

Miller, H.G., Singh, V., 1994. Potential field tilt—a new concept for location of potential field sources. *Journal of Applied Geophysics* 32, 213–217.

Mosar, J., 2000. Depth of extensional faulting on the Mid-Norway Atlantic passive margin. *Norges geologiske undersøkelse Bulletin* 437, 33–41.

Mosar, J., Osmundsen, P.T., Sommaruga, A., Torsvik, T.H., Eide, E.A., 2002. Greenland– Norway separation: a geodynamic model for the North Atlantic. *Norwegian Journal of Geology* 82, 281–298.

Nasuti, A., Pascal, C., Ebbing, J., Tønnesen, J.F., 2011. Geophysical characterisation of two segments of the Møre–Trøndelag Fault Complex, Mid Norway. *Solid Earth* 2, 125–134.

Nordgulen, Ø., Braathen, A., Corfu, F., Osmundsen, P.T., Husmo, T., 2002. Polyphase kinematics and geochronology of the late-Caledonian Kollstraumen detachment, north-central Norway. *Norwegian Journal of Geology* 82, 299–316.

Norton, M.G., 1986. Late Caledonian extension in western Norway: a response to extreme crustal thickening. *Tectonics* 5, 192–204.

Oftedahl, C., 1975. Middle Jurassic graben tectonics in Mid Norway. *Proc. Jurassic Northern North Sea Symposium*, 21, pp. 1–13.

Olesen, O., Lundin, E., Nordgulen, Ø., Osmundsen, P.T., Skilbrei, J.R., Smethurst, M.A., Solli, A., Bugge, T., Fichler, C., 2002. Bridging the gap between the onshore and offshore geology in Nordland, northern Norway. *Norsk Geologisk Tidsskrift* 82, 243–262.

Olesen, O., Brönner, M., Ebbing, J., Gellein, J., Gernigon, L., Koziel, J., Lauritsen, T., Myklebust, R., Sand, M., Solheim, D., Usov, S., 2010. New aeromagnetic and gravity compilations from Norway and adjacent areas — methods and applications. *Petroleum Geology Conference Series* 7, 559–586.

Olsen, E., Olsen, E., Gabrielsen, R.H., Braathen, A., Redfield, T.F., 2007. Fault systems marginal to the Møre Trøndelag Fault Complex, Osen–Vikna area, Central Norway. *Norwegian Journal of Geology* 87, 59–73.

Osmundsen, P.T., Ebbing, J., 2008. Styles of extension offshore Mid Norway and implications for mechanisms of crustal thinning at passive margins. Tectonics 27 (TC6016).

Osmundsen, P.T., Sommaruga, A., Skilbrei, J.R., Olesen, O., 2002. Deep structure of the Mid-Norway Rifted Margin. *Norwegian Journal of Geology* 82, 205–224.

Osmundsen, P.T., Braathen, A., Nordgulen, Ø., Roberts, D., Meyer, G.B., Eide, E., 2003. The Devonian Nesna shear zone and adjacent gneiss-cored culminations, North-Central Norwegian Caledonides. *Journal of the Geological Society of London* 160, 137–150.

Osmundsen, P.T., Eide, E., Haabesland, N.E., Roberts, D., Andersen, T.B., Kendrick, M., Bingen, B., Braathen, A., Redfield, T.F., 2006. Kinematics of the Høybakken detachment zone and the Møre–Trøndelag Fault Complex, central Norway. *Journal of the Geological Society* 163, 303–318. doi:10.1144/0016-764904-129.

Pascal, C., Gabrielsen, R.H., 2001. Numerical modelling of Cenozoic stress patterns in the Mid Norwegian Margin and the northern North Sea. *Tectonics* 20, 585–599.

Pascal, C., Angelier, J., Seland, R., Lepvrier, C., 2002. A simplified model of stress–slip relationships: application to the Frøy Field, northern North Sea. *Tectonophysics* 357, 103–118.

Pascal, C., Roberts, D., Gabrielsen, R.H., 2010. Tectonic significance of present-day stress relief phenomena in formerly glaciated regions. *Journal of the Geological Society of London* 167, 363–371.

Redfield, T.F., Osmundsen, P.T., 2009. The Tjellefonna Fault system of western Norway: linking late-Caledonian extension, post-Caledonian normal faulting and Tertiary rock-column uplift with the landslide-generated tsunami event of 1756. *Tectonophysics* 474, 106–123.

Redfield, T.F., Torsvik, T.H., Andriessen, P.A.M., Gabrielsen, R.H., 2004. Mesozoic and Cenozoic tectonics of the Møre Trøndelag Fault Complex, central Norway: constraints from new apatite fission track data. *Physics and Chemistry of the Earth* 10 (29), 673–682.

Redfield, T.F., Osmundsen, P.T., Hendriks, B.W.H., 2005. The role of fault reactivation and growth in the uplift of western Fennoscandia. *Journal of the Geological Society of London* 162, 1013–1030.

Roberts, D., 1998. High-strain zones from meso-to macro-scale at different structural levels, Central Norwegian Caledonides. *Journal of Structural Geology* 20, 111–119.

Roberts, D., Gee, D.G., 1985. An introduction to the structure of the Scandinavian Caledonides. In: Gee, D.G., Sturt, B.A. (Eds.), The Caledonide Orogen — Scandinavia and Related Areas. John Wiley & Sons Ltd, Chichester, pp. 55–68.

Roberts, D., Myrvang, A., 2004. Contemporary stress orientation features in bedrocks, Trøndelag, central Norway, and some regional implications. *Norges geologiske undersøkelse Bulletin* 442, 53–63.

Séranne, M., 1992. Late Paleozoic kinematics of the Møre–Trøndelag Fault Zone and adjacent areas, central Norway. *Norsk Geologisk Tidsskrift* 72, 141–158.

Séranne, M., Séguret, M., 1985. Etirement ductile et cisaillement basal dans les bassins dévoniens de l'Ouest Norvège. Comptes Rendus de l' Academie des Sciences, Paris 300 (II), 373–378.

Séranne, M., Séguret, M., 1987. The Devonian basins of western Norway: tectonics and kinematics of an extending crust. 111. In: Coward, M.P., Dewey, J.F., Hancock, P.L. (Eds.), Continental Extensional Tectonic: Geological Society, London, Special Publications, 28, pp. 537–548.

Sigmond, E. M. O. 2002. Geological map, land and sea areas of northern Europe. Scale 1: 4 million. Geological Survey of Norway, Trondheim.

Simpson, R.W., Jachens, R.C., Blakely, R.J., 1983. AIRYROOT: a Fortran program for calculating the gravitational attraction of an Airy isostatic root out to 166.7 km. United States Department of the Interior, Geological Survey, Open-File Report 83–883. 24 pp.

Skilbrei, J.R., 1988. Geophysical Interpretation of the Fosen–Namsos Western Gneiss Region and Northern Part of the Trondheim Region Caledonides, Central Norway. Geological Survey of Norway, Trondheim, Special Publications, 3, pp. 59–69.

Skilbrei, J.R., Olesen, O., 2005. Deep structure of the Mid-Norwegian shelf and onshore– offshore correlations: insight from potential field data. In: Wand°, B.T.G., Eide, E.A., Gradstein, F., Nystuen, J.P. (Eds.), Onshore–Offshore Relationships on the North Atlantic Margin. *Norwegian Petroleum Society (NPF),* pp. 43–68.

Skilbrei, J.R., Olesen, O., Osmundsen, P.T., Kihle, O., Aaro, S., Fjellanger, E., 2002. A study of basement structures and some onshore–offshore correlations in Central Norway. *Norwegian Journal of Geology* 82, 263–279.

Slagstad, T., Barrère, C., Davidsen, B., Ramstad, R.K., 2008. Petrophysical and thermal properties of pre-Devonian basement rocks on the Norwegian continental margin. *Geological Survey of Norway Bulletin* 448, 1–6.

Sommaruga, A., Bøe, R., 2002. Geometry and subcrop maps of shallow Jurassic basins along the Mid-Norway coast. *Marine and Petroleum Geology* 19, 1029–1042.

Strömberg, A.B.G., 1976. A pattern of tectonic zones in the western part of the East European Platform. Geologiske Föreningens i Stockholm Förhandlinger 98, 227–243.

Talwani, M., Eldholm, O., 1972. The continental margin off Norway: a geophysical study. *Geological Society of America Bulletin* 83, 3375–3608.

Thorsnes, T., 1995. Structural setting of two Mesozoic half-grabens of the coast of Trøndelag, Mid-Norwegian shelf. *Norges Geologiske Undersøkelse Bulletin* 427, 68–71.

Titus, S.J., Fossen, H., Pedersen, R.B., Vigneresse, J.L., Tikoff, B., 2002. Pull-apart formation and strike–slip partitioning in an obliquely divergent setting, Leka Ophiolite, Norway. *Tectonophysics* 354, 101–1019.

Vågnes, E., Gabrielsen, R.H., Haremo, P., 1998. Late Cretaceous–Cenozoic intraplate contractional deformation at the Norwegian continental shelf: timing, magnitude and regional implications. *Tectonophysics* 300, 29–46.

Watts, L.M., 2001. The Walls Boundary Fault Zone and the Møre–Trøndelag Fault Complex: a case study of two reactivated fault zones. Unpublished PhD thesis, Department of Geological Sciences, University of Durham.

Wolff, F.C. 1976. Trondheim. Geological map of Norway, Bedrock map, 1:250 000 series. Geological Survey of Norway, Trondheim.

Chapter 4. Paper II. Geophysical characterisation of two segments of the Møre-Trøndelag Fault Complex, Mid Norway

A. Nasuti[1,2], C. Pascal[2,3], J. Ebbing[1,2], and J. F. Tønnesen[2]

[1] Department of Petroleum Engineering and Applied Geophysics, Norwegian University of Science and Technology, 7491 Trondheim, Norway.
[2]NGU, Geological Survey of Norway, 7491 Trondheim, Norway
[3]Institute of Geology, Mineralogy & Geophysics, Ruhr University, Bochum, Germany

ARTICLE INFO

Solid Earth

ABSTRACT

The Møre-Trøndelag Fault Complex (MTFC) has controlled the tectonic evolution of Mid Norway and its shelf for the past 400 Myr through repeated reactivations during Palaeozoic, Mesozoic and perhaps Cenozoic times, the very last phase of reactivation involving normal to oblique-slip faulting. Despite its pronounced signature in the landscape, its deep structure has largely remained unresolved until now. We focused on two specific segments of the MTFC (i.e. the Tjellefonna and Bæverdalen faults) and acquired multiple geophysical datasets (i.e. gravity, magnetic, resistivity and shallow refraction profiles).

A 100–200 m-wide zone of gouge and/or brecciated bedrock steeply dipping to the south is interpreted as being the Tjellefonna fault sensu stricto. The fault appears to be flanked by two additional but minor damage zones. A secondary normal fault also steeply dipping to the south but involving indurated breccias was detected ~1 km farther north. The Bæverdalen fault, ~12 km farther north, is interpreted as a ~700 m-wide and highly deformed zone involving fault gouge, breccias and lenses of intact bedrock. As such, it is probably the most important fault segment in the studied area and accommodated most of the strain during presumably Late Jurassic normal faulting. Our geophysical data are indicative of a Bæverdalen fault dipping steeply towards the south, in agreement with the average orientation of the local tectonic grain. Our findings suggest that the influence of Mesozoic normal faulting along the MTFC on landscape development is more complex than previously thought.

4.1 **Introduction**

The Møre-Trøndelag Fault Complex (MTFC, Fig. 1), Mid Norway, is a long-lived structural zone whose tectonic history has involved repeated reactivation since Caledonian times (e.g. Grønlie et al., 1994, Watts, 2001). The MTFC appears to have controlled the evolution of both the oil-rich basins offshore (Brekke 2000) and the rugged landscape onshore (Redfield et al., 2005). It strikes ENE-WSW, paralleling the coastline of Mid Norway southwest of Trondheimsfjord, and separates the northern North Sea basin system from the deep Mesozoic Møre Basin (Brekke, 2000). Despite its pronounced signature in the landscape, its deep structure has largely remained unresolved until now, the only exception being the interpretation of a seismic reflection profile on Fosen Peninsula (Hurich & Roberts, 1997). The fault cores themselves are, in general, not exposed and their respective traces can only be seen as topographic lineaments (Fig. 1). Furthermore, their exact locations, extents, widths and dips remain, with the exception of the Hitra-Snåsa and Verran faults on Fosen Peninsula (e.g. Grønlie & Roberts, 1989), in most cases speculative, and have not been studied systematically by means of geophysical methods.

A common assumption behind most geological models proposed to describe the regional tectonic evolution is that the ENE-WSW faults of the MTFC dip, in general, steeply towards the north-northwest and, therefore, represent the inland boundaries of the offshore basins (e.g. Gabrielsen et al., 1999). Redfield et al. (2005) proposed, in particular, that the abrupt change in elevation seen just southeast of the MTFC, with higher topography in the south, reflects Mesozoic normal faulting to the north-northwest along the major segments of the fault complex. Furthermore, according to this latter model, the present-day topography of southern Norway (i.e. the Southern Scandes) would have been the result of this last phase of reactivation of the MTFC.

A consensus on the origin of the enigmatic topography of Norway is, however, still pending (e.g. Nielsen et al., 2009, Gabrielsen et al., 2010). With the present study, we aim to shed new light on the deep structure of the MTFC and introduce new observations and data to the ongoing debate. We present the results of the acquisition of several geophysical datasets across two of the major segments of the MTFC, the so-

called Tjellefonna and Bæverdalen faults (Fig. 1), and discuss their significance in terms of the geological evolution of the area.
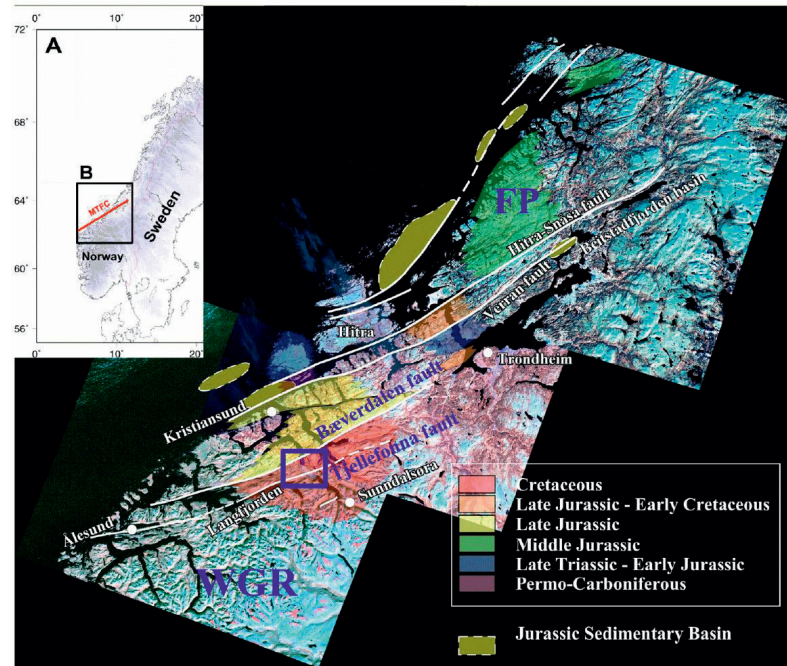
Fig. 1. Principal structural features of the Møre-Trøndelag FaultComplex (MTFC) and surrounding regions. (A) Location of the Møre-Trøndelag Fault Complex (MTFC) onshore Norway. (B) Composition of three LandSat scenes showing the major lineaments of the MTFC (after Redfield et al., 2005). The blue frame depicts the study area. FP- Fosen Peninsula, WGR- Western Gneiss Region.

4.2 **Geology and tectonic setting of the study area**

The study area is located in the Western Gneiss Region (WGR) of Mid Norway (Fig. 1). Regional-scale interpretations (Gabrielsen & Ramberg, 1979; Nasuti et al., 2010b) indicate that two segments of the MTFC (i.e. the Bæverdalen and Tjellefonna faults, informally named by Redfield et al. 2004 and Redfield & Osmundsen 2009, respectively) cross the study area. The WGR is a basement window exhumed in Devonian to Early Carboniferous times as part of a megascale, late- to post-Caledonian extensional or transtensional system (e.g. Andersen and Jamtveit, 1990; Krabbendam and Dewey, 1999, Braathen et al., 2000). The bedrock of the area is dominated by Late Palaeoproterozoic gneisses strongly reworked during the Caledonian Orogeny (Tveten

et al., 1998). The gneisses have a magmatic origin and are locally migmatitic, varying from quartz-dioritic to granitic compositions (Fig. 2).
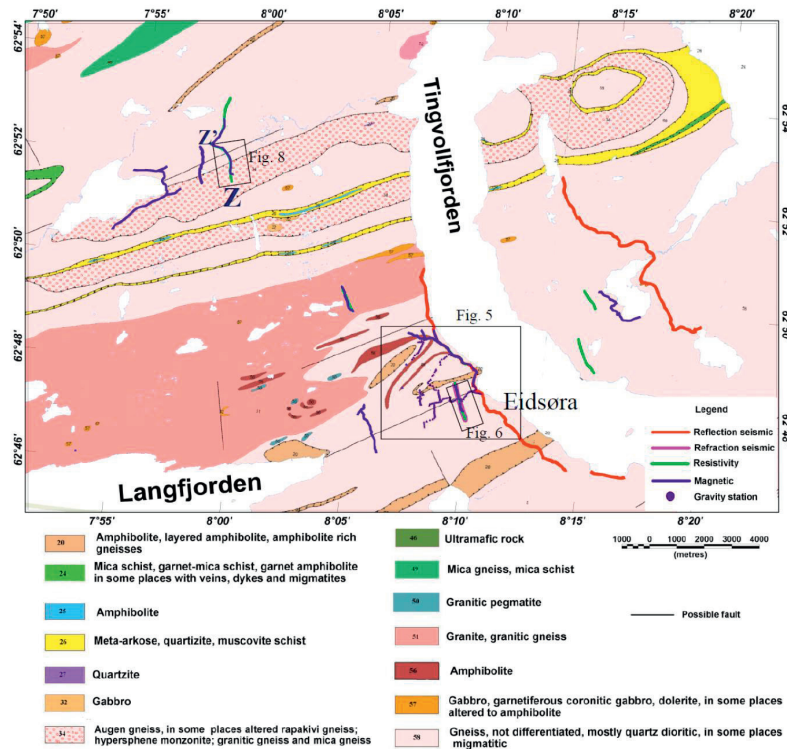
Fig. 2. Simplified bedrock map of the study area (after Tveten et al., 1998). The respective locations of the different geophysical profiles are shown. The black boxes outline some of the geophysical profiles shown in Figs. 5, 6, and, 8.

The structural grain inherited from the Caledonian event consists of polyphase tight to open folds with axes trending ENE-WSW (e.g. Tucker et al., 1990, Robinson 1995, Hacker et al., 2010). Field evidence shows that the steep flanks of the folds were subsequently exploited to accommodate sinistral strike-slip in Devonian (Grønlie et al. 1991, Séranne, 1992, Watts, 2001) and normal dip-slip faulting in post-Mid Jurassic times (i.e. presumably Late Jurassic-Early Cretaceous, Bøe and Bjerkli, 1989, Bering 1992, Grønlie et al., 1994). Reactivations of the MTFC in Permo-Triassic (Grønlie et al. 1994) and Cenozoic time (Grønlie et al., 1990, Redfield et al., 2005) have been proposed but firm evidence to support these latter faulting events is still lacking. The

MTFC is moderately active at the present-day and appears to divert the regional stress field (Pascal and Gabrielsen, 2001, Roberts & Myrvang, 2004, Pascal et al., 2010).

Interestingly, Redfield et al. (2004, 2005) and Redfield and Osmundsen (2009) report significant apatite fission track (AFT) age jumps across the major ENE-WSW segments of the MTFC (Fig. 1), most apparent ages ranging from Triassic to Early Cretaceous. This group of authors explain the general trend of a southward decrease in AFT ages with a model involving gradual erosion of the uplifted successive footwalls, faulting and erosion progressing away from the rifted margin from north to south (i.e. the 'scarp retreat' model). Accordingly, the abrupt relief south of the Tjellefonna fault (Fig.1) and, in general, the topography of southern Norway would be relics of this process. An implication of the 'scarp retreat' model is that faults of the MTFC should dip towards the north.

4.3 Data acquisition

In order to detect the fault zones and their structural attributes, a series of gravity, magnetic, 2D-resistivity, shallow-refraction and reflection-seismic profiles were measured across two presumed segments (Figs. 2 and 3) as part of the MTFC Integrated Project (Nasuti et al., 2009, 2010a). Note that a detailed description and interpretation of the reflection seismic profiles will be presented in a forthcoming publication, so far reported only in an abstract (Lundberg et al., 2009).

Gravity and magnetic data help to determine the thickness of the overburden and eventually the location of the fault cores. In addition, rock sampling and petrophysical measurements on densities and magnetic susceptibilities in the study area constrain the geophysical models. 2D-resistivity and shallow-refraction seismic data are commonly used to map fractures and faults. Resistivity studies image shallow/near-surface structures with higher resolution than seismic surveys. Along one of the 2D resistivity profiles, shallow-refraction seismic data were also acquired. Refraction seismics is generally very effective at determining heavily fractured bedrock and wide zones of fault gouge.
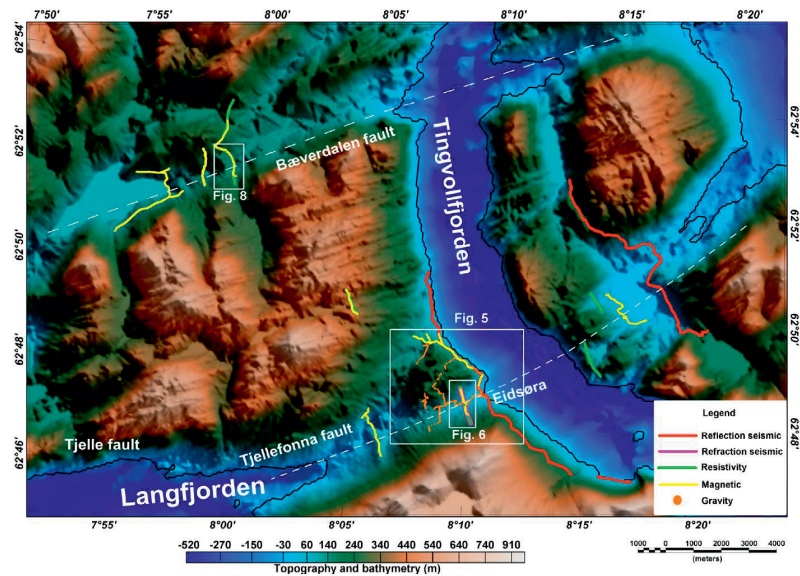
Fig. 3. Several geophysical datasets have been acquired in the study area (blue box in Fig. (1). The background map depicts topography and bathymetry. The white boxes outline geophysical profiles whose corresponding results are shown in Figs. 5, 6 and 8. Dashed white lines show the proposed Tjellefonna and Bverdalen faults.

4.3.1 **Gravity data**

In total, 265 gravity stations were established in a 4 x 4 km area close to Eidsøra (Fig. 3). The gravity survey was planned to study the thickness of the overburden and to detect eventual gravity signals related to the faults. The distance between gravity stations varied from 15 to 80 metres. More densely spaced gravity data were acquired in the vicinity of the Tjellefonna fault, in particular along profiles perpendicular to the strike of the inferred fault. Away from it, station spacing was increased. For all stations the elevation was determined by levelling. In order to increase the accuracy of our survey, measurements were carried out at least twice at each gravity station. For positioning we used a total station survey camera with a precision of 1 mm. Measuring accuracy was in the order of 10 to 20 μ Gal. A combined bathymetry-topography compilation (Olesen et al., 2010) with a resolution of (250 x 250 m) was used for the regional terrain correction, and a high-resolution grid 25 x 25 m created by the Norwegian Mapping Authority, based on triangulation of 20 m contour maps and road

and river data, was used over the study area. Further details about data acquisition can be found in Nasuti et al. (2010a).

4.3.2 Magnetic data

The magnetic profiles were set up in order to cross the two chosen segments of the MTFC. Fifteen magnetic profiles with variable lengths from 1000 to 2500 m were measured (Fig. 3). Measurements were made using a GSM-19 magnetometer with two sensors separated vertically by 56 cm in order to measure vertical gradients and the total magnetic field simultaneously.

A significant number of noise sources (e.g. power lines, electric fences) exist in the survey area and, consequently, high noise levels were recorded along some of the profiles (Nasuti et al. 2010a). Such high-amplitude noise overprints the anomalies related to geological structures and had to be removed before processing. A 50 Hz low-pass filter was used to remove noise and very high frequencies. Measured vertical gradients are in most cases affected by high noise levels; therefore, we focus only on total magnetic field anomalies. The magnetic data were further corrected for diurnal variations using base station readings and the International Geomagnetic Reference Field 2005 was subtracted.

4.3.3 Petrophysical data and Bouguer corrections

Magnetic and gravity properties were derived from petrophysical measurements made on rock samples collected, in the framework of the project, in secondary fault zones and their host rocks (Biedermann 2010). The samples consist mainly of gneisses and amphibolites typical of the area (Fig. 2). Samples A to L were collected along a profile following the southwestern shore of Tingvollfjorden (Fig. 5). Samples F, G and H originate from locations just north and south of the surface expression of a minor but visible fault. Analysis of the samples showed that the bulk magnetic susceptibility of the gneisses varies from ~10-4 to ~10-2 SI (Table 1). The variation in bulk susceptibility over two orders of magnitude can be explained by changes in mineralogy, different concentrations of ferromagnetic minerals and varying grain sizes (see details in Biedermann 2010).

Rock densities can be determined by measuring samples collected in the field. However, densities usually vary over a wide range even within the same rock unit, so that a large number of samples are required to determine a reliable average value. In addition, it is often difficult to obtain representative samples from well below the weathered surface. We applied the classical Nettleton method (Nettleton 1939) to estimate the bulk density of the rocks in the gravity survey area and to compute Bouguer corrections.

The optimum density is estimated by calculating a series of Bouguer anomalies as a function of rock density and comparing with topography (Fig. 4). For the optimum density (i.e. the actual bulk density), the computed gravity anomaly profile should show minimal correlation with topography. It is essential that the topographic feature selected for the gravity profile displays at least one reversal (Fig. 4b, Nettleton 1939). The optimum density was found to be 2790 kg/m^3 along the traverse N-N'. When compared to the measured densities (Table 1), this value falls between the typical values obtained for gneisses and amphibolites, suggesting that the rocks below the gravity profile are a mixture of both rock types.

Fig. 5 shows Bouguer anomalies computed according to the optimum density value. Bouguer anomalies are quite modest (Fig. 5). A Bouguer low is, nevertheless, observed along the valley floor where the Tjellefonna fault is suspected to occur. However, this may reflect at the first order the low-density Quaternary overburden, which varies in thickness from a few metres to several tens of metres. We will address this issue further below.
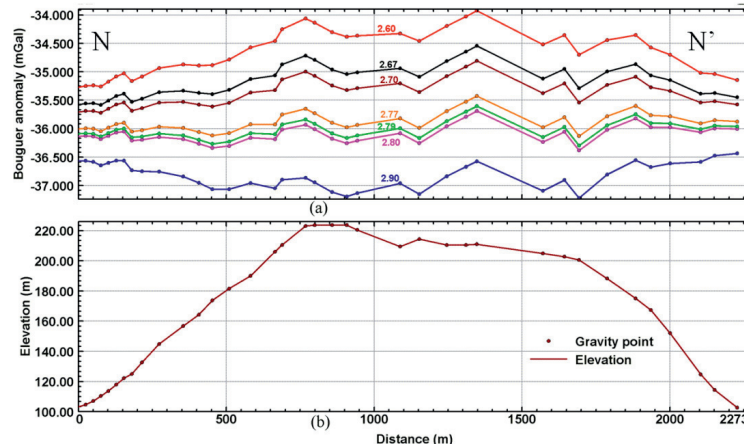
Fig. 4. Determination of the bulk density of the studied domain using the Nettleton Method. (a) Computed Bouguer anomalies along NN using different densities. The location of this profile is shown in Fig. 5. (b) Topography of the profile with location of the gravity points.

Table 1. Summary of the physical properties of the rock samples. Details of the petrophysical analysis and sample information are given in Biedermann (2010).

Lithology	Density range (kg/m^3)	Susceptibility range (SI)	Number of samples
Gneisses	2643–2745 Median: 2680	$9.92 \times 10^{-5} - 1.21 \times 10^{-2}$ Median: 2.23×10^{-3}	10
Amphibolites	2938–3066 Mean: 3002	$7.46 \times 10^{-4} - 1.28 \times 10^{-3}$ Mean: 1.02×10^{-3}	2
Fault rocks	2504–2642 Median: 2623	$1.13 \times 10^{-3} - 1.19 \times 10^{-2}$ Median: 4×10^{-3}	4

4.3.4 **Resistivity**

The 2D-resistivity survey consists of seven profiles, mostly oriented NW-SE in order to cross the fault structures perpendicularly (Figs. 2 and 3). The resistivity method measures apparent resistivity in the subsurface, which is a weighted average of all resistivity values within the measured volume (Dahlin 1996, Reynolds 1997). The 2D-resistivity profiles were acquired according to the Lund system (Dahlin 1996). Data were collected with a gradient array configuration with electrode spacing of 10 and 20 metres to map the shallow and deeper parts of the profiles respectively. The depth penetration is approximately 130 metres, with a reliable data coverage to approximately 70 metres depth.
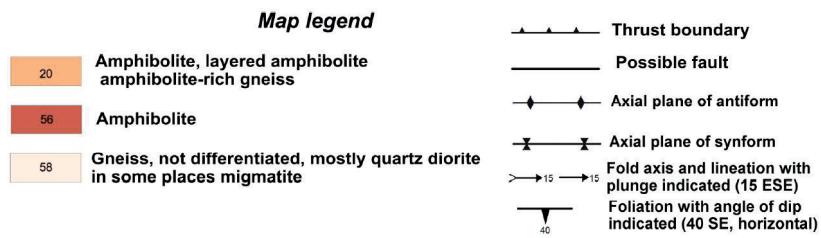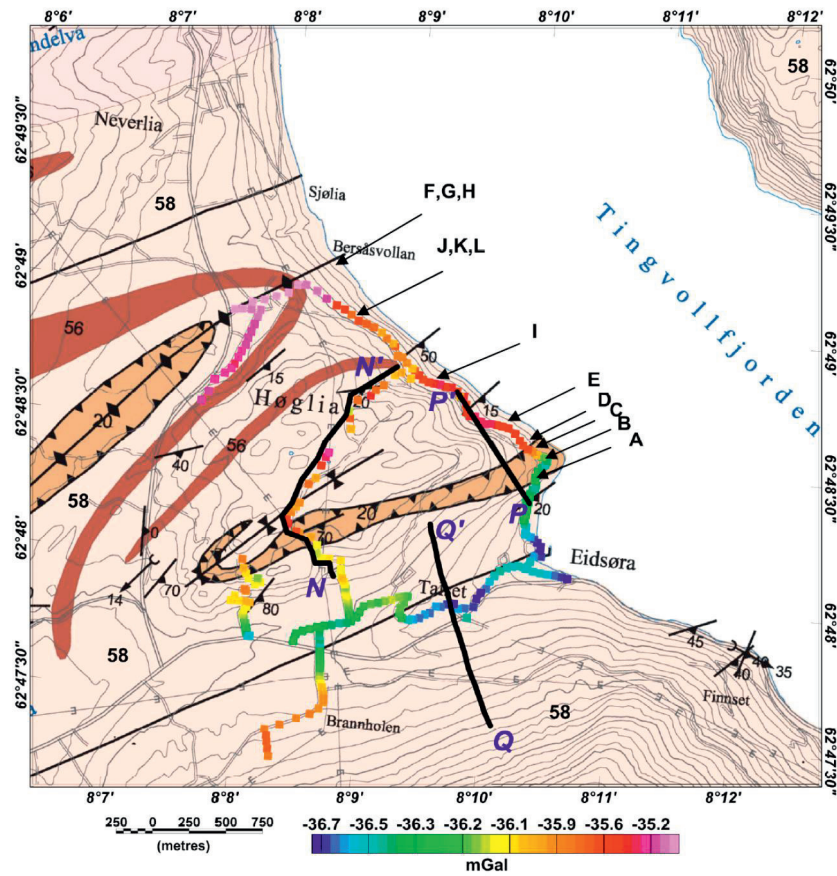
Fig. 5. Bouguer anomalies calculated using a reduction density of 2790 kg m^{-3} and superposed on the geological map (Tveten et al., 1998). NN is the traverse used to determine the reduction density (Fig. 4). QQ and PP' are profiles shown in Figs. 6 and 7 respectively. Letters in black represent petrophysical sampling sites (Biedermann, 2010).

Measured apparent resistivities with different electrode configurations were converted into 2D true resistivity profiles using the Res2Dinv software (Loke 2004). In the inverted profiles, relatively low-resistive zones may indicate fractured and/or water saturated bedrock, while more resistive ones are diagnostic for fresh bedrock. Particularly low resistivity (i.e. lower than 1000 Ωm) characterises clay-filled fractures and, consequently, also fault gouge (e.g. Ganerød et al. 2008). Further details can be found in Nasuti et al. (2009).

4.3.5 Seismic profiling

Two reflection and one shallow-refraction seismic profiles were acquired perpendicular to the Tjellefonna fault (Fig. 3). The reflection-seismic profiles were shot on both sides of Tingvollfjorden with the aim of imaging the upper 4 km of the crust. Details on this particular study will soon be published by Lundberg & Juhlin (in prep.). The refraction profile was 1320 m long (Fig. 3). The profile was measured with two seismic cables, each involving 12 geophone connections. Geophone spacing along the cables was 10 m, except at the end of the cables where the spacing was reduced to 5 m. Along each cable, five shots were arranged with 110 m shot spacing in each layout. For short distances 100 grams of dynamite were used, while up to 200 grams were used for greater distances from the geophones. The classical plus-minus method (Hagedoorn 1959) was used for estimating seismic velocities and layer thickness in combination with estimating layering and thickness from intercept times and crossover distances. The interpretation is shown in Fig. 6a. More details can be found in Nasuti et al. (2009).

4.4 Integration and interpretation of the geophysical data

4.4.1 Tjellefonna fault

Fig. 6 shows the results from three independent datasets acquired across the Tjellefonna fault along profile QQ' (Fig. 5). At the top, a thin layer of soil with very low seismic P-wave velocities (400-600 m/s) is imaged. Just below this layer, P-wave velocities increase to 1400-2300 m/s in what is interpreted to be the Quaternary overburden. The underlying bedrock has, in general, velocities of 4500-5100 m/s, but clearly shows three distinctive, vertical, low-velocity zones (Fig. 6a). Low P-wave

velocity values (i.e. less than 4000 m/s) suggest the presence of densely fractured and/or fault gouge. We note that S2 appears to be wider than S1 and S3. Furthermore, S2 is associated with a lower velocity (i.e. 2500 m/s) with respect to the two other velocity anomalies (i.e. 3500 and 3700 m/s for S1 and S3, respectively). These observations are suggestive of highly strained rock material and, presumably, the presence of significant volumes of densely fractured and/or unconsolidated fault gouge at the location of S2.

We imaged a low-resistive top layer (Fig. 6b) corresponding to the low-velocity layer (Fig. 6a) and representing, without doubt, the unconsolidated Quaternary sediments. Low-resistive anomalies are also imaged in the bedrock (i.e. R1, R2 and R3, Fig. 6b). The length of the resistivity profile, acquired following the refraction seismic line, is 1400 m. A remarkably good spatial correlation is found between seismic anomaly S2 and R2 and between S3 and R3, adding support to the interpretation that these co-located anomalies represent fault zones. In particular, the respective widths of S2 and R2 are very similar. The southern edge of R2 looks vertical but we note that the apparent geometry of its northern edge strongly suggests a structure dipping towards the south. No visible counterpart is found for seismic anomaly S1. This latter seismic anomaly may potentially be a blind zone created by shallow cavities (Westerdahl 2003) and, therefore, may not represent any actual fault zone. In turn, R1 might represent a relatively minor deformation zone.

In order to refine our interpretation, we compare the previous results with our magnetic data. Because of the presence of a high-voltage power line, the magnetic profile contains a small gap of ~100 m. Nevertheless, three magnetic anomalies depicted as central lows between high-amplitude and mainly short-wavelength peaks can be distiguished (i.e. M1, M2 and M3, Fig. 6c). M2 is the most pronounced magnetic anomaly and correlates very well with seismic anomaly S2 and resistivity anomaly R2. Contacts between rocks with contrasting magnetic properties are commonly associated with positive and negative magnetic anomalies with steep gradients. The M2 anomaly appears to reflect the existence of two rock contacts in the subsurface correlating with the edges of R2 and that we interpret as the two outer boundaries of the fault zone (Fig. 6c). In brief, the analysis of the three geophysical datasets points unambiguously to the presence of a 100-200 m-wide fault zone at the centre of profile QQ', that we interpret as the Tjellefonna fault *sensu stricto*. Magnetic anomaly M3 appears to be less

pronounced but it may be related to both seismic anomaly S3 and resistivity anomaly R3. Our interpretation is that a secondary and narrower fault produces these signals, including perhaps M3. Finally, some correlation appears between magnetic anomaly M1 and seismic anomaly S1, and both geophysical anomalies are tentatively attributed to another minor fault zone; however, as discussed previously, this latter interpretation remains uncertain. A forward model was run to further evaluate the magnetic anomalies (Fig. 6d). The model involves three zones with higher susceptibilities which could reflect fault zones enriched in magnetic minerals. M2 was reasonably well simulated by a southward-dipping zone, which we propose corresponds to the major fault zone of the area. The overburden thickness was calibrated according to the seismic and resitivity data.

4.4.2   A subordinate fault to the Tjellefonna fault

We now focus on profile PP' that we anticipated to cross a secondary structure adjacent to the Tjellefonna fault (Fig. 5). The Bouguer anomaly displays a steep gradient (Figs. 5 and 7). This gradient is expressed by a step-like anomaly with an amplitude of 0.8 mGal that coincides with a pronounced positive anomaly in the magnetic data (Fig. 7a). We used the GMSYS-2D modelling package (Popowski et al., 2009) in order to model the sources of the observed Bouguer and magnetic anomalies along profile PP'.

The physical parameters (i.e. density and magnetic susceptibility) used to model the host rocks are based on laboratory measurements of samples collected along profile PP' (Biedermann 2010) and summarised in Table 1. Biedermann's study indicates that the magnetic anomalies are dominated by induced magnetisation. Therefore the effect of remanent magnetisation can be neglected in the modelling. The measured density values for each type of rock show a relatively wide scatter and we used these ranges of values to constrain the most likely densities in the model. We rely on the density determined by means of the Nettleton method (i.e. 2790 kg/m^3, Fig. 4) for the central part of the PP' profile, that involves a mixture of amphibolites and gneisses. Note that the bedrock map (Fig. 5) indicates a narrower strip of amphibolites as compared to our 2D model (Fig. 7). However, we observed and sampled amphibolites outside the area where they have

been reported (i.e. samples F and J, Fig. 5 and Biedermann 2010), supporting the suggestion that the central part of our profile involves a mixture of both rock types.
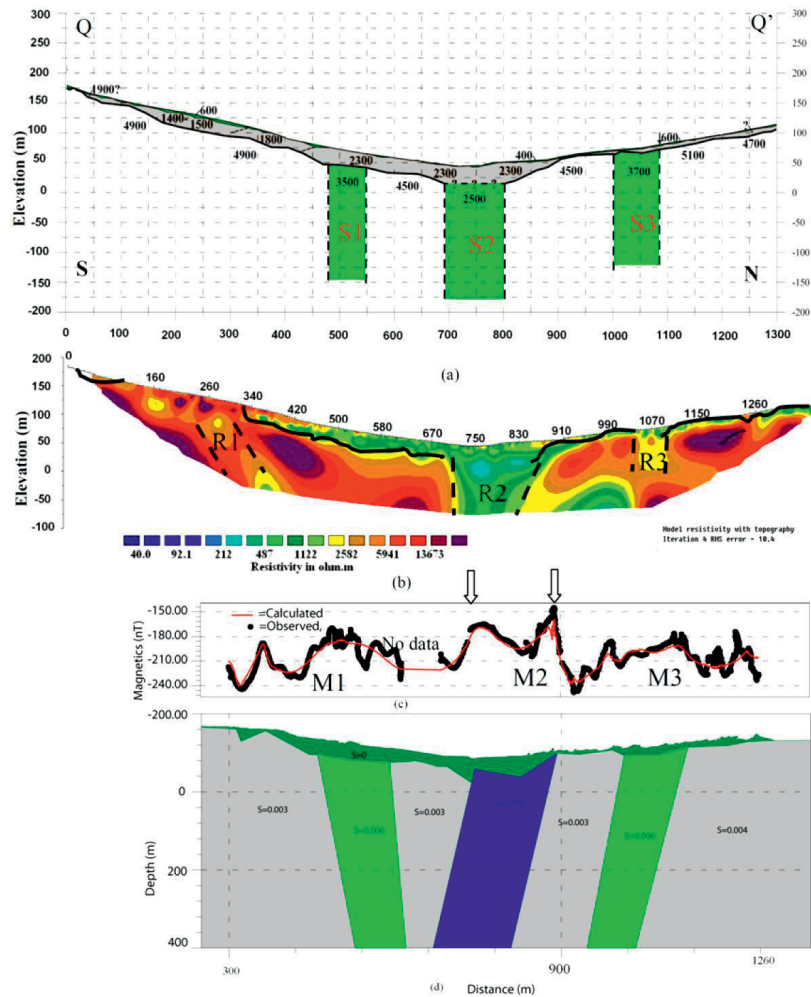
Fig. 6. Geophysical profiling across the Tjellefonna Fault. (a) The refractionseismic profile shows three low-velocity zones (S1, S2 and S3); velocities in m s $^{-1}$. (b) Depth-inverted 2-D-resistivity profile showing three low-resistivity zones (R1, R2 and R3). Continuous and dashed lines represent the interpreted top bedrock and the edges of the interpreted main fault zone, respectively. (c) Magnetic profile. The arrows on top of the magnetic anomaly show the edges of the interpreted main fault zone. Profile locations are shown in Figs. 3 and 5. (d) A model is proposed for magnetic anomalies.
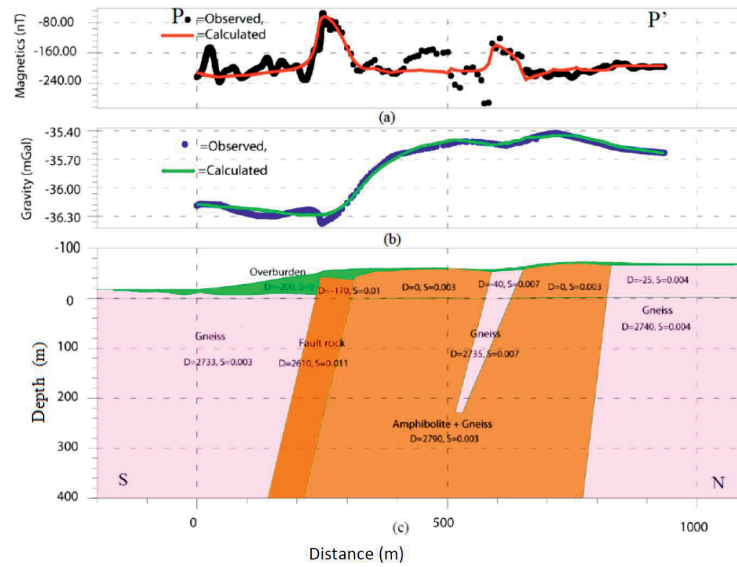
Fig. 7. 2-D model along profile PP'. Density (D) and susceptibility (S) of the blocks are in SI units. See text for modelling details. Note that for modelling Bouguer gravity anomalies, density contrasts with respect to the reduction density are used above the reduction level (i.e. sea-level).

A southward-dipping block with a density of 2610 kg/m^3 and a magnetic susceptibility of 0.011 (SI units) is added to the model to simulate fault rocks. The chosen values for the modelling were calibrated according to the results of the petrophysical measurements carried out on five fault rock samples (Biedermann 2010, Table 1). These samples consist of indurated breccias and were collected a few kilometres east and west of Eidsøra but along the same topographic lineament as the one crossing the study area (see precise locations in Biedermann 2010). Note that our choice of a fault dipping to the south in the model is supported by (1) the average dip of the local structural grain as measured in the field (i.e. foliation, Fig. 5) and (2) reflection-seismic experiments showing a reflector presumably related to the fault dipping 60-70^0 to the south (Lundberg et al. 2009). After testing various modelling scenarios, we concluded that one realistic solution to explain the observed gravity and magnetic fields is that a ~50 m-wide and south-dipping fault zone composed of indurated breccias, like the ones cropping out near Tjelle (Redfield and Osmundsen 2009, Bauck 2010), separates mostly dioritic gneisses from a mixture of amphibolites and gneisses.

4.4.3 **Bæverdalen fault**

Fig.8 shows 2D-resistivity and magnetic profiles measured perpendicular to the Bæverdalen fault. The inverted resistivity data show three low-resistive anomalies and a shallow layer with very low resistivity at the top of the section, corresponding to water-saturated sediments. The low-resistivity anomalies (A1, A2 and A3) along the profile may relate to highly strained zones of the MTFC and are interpreted to represent water-saturated, fractured and/or extensive fault gouge. There is a good spatial correlation between resistivity anomaly A1 and magnetic anomaly U (Fig.8 b). Anomaly U has an amplitude of 200 nT and mimics the expected shape for a magnetic anomaly arising from a contact between two blocks with contrasting magnetic properties. However, the correlation between rock contacts imaged in the resistivity profile and that inferred from the magnetic one is not straightforward in the present case. Nevertheless, the structure of the subsurface below the location of magnetic anomaly U appears to be complex, and the shape of anomaly A1 is suggestive of either a southward shallow-dipping fault zone or (our preferred interpretation) a steep and wide crushed zone involving lenses of intact bedrock.
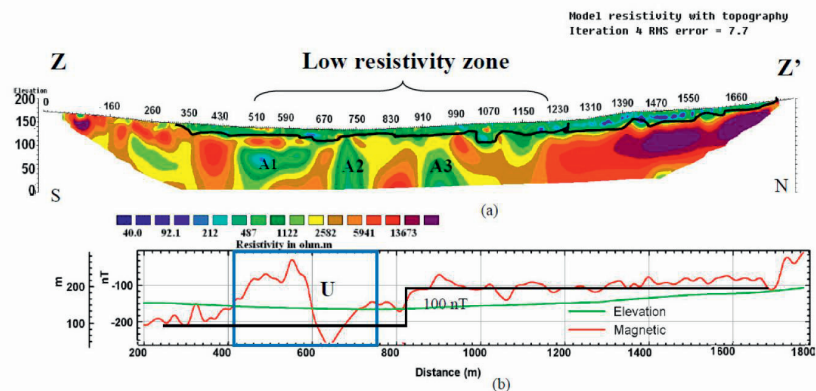
Fig. 8. Results from resistivity and magnetic profiling over the Bverdalen fault. (a) Results from inversion of the 2-D-resistivity data. (b) Magnetic profile (see Fig. 2 for location).

A high-resistivity anomaly is detected at the northern end of the profile, which points to intact bedrock and could eventually represent the moderately deformed footwall of the Bæverdalen fault. The shape of the anomaly suggests a steep rock contact, presumably the northern boundary of the damage zone. In general, resistivity is

low to very low over a ~700 m-wide zone (Fig. 8a), suggesting a large faulted corridor. Furthermore, the magnetic trend along the profile shows a marked jump from -200 nT in the south to -100 nT in the north while crossing the low-resistive zone, suggesting different rocks or, at least, variations in petrophysical properties within the same rock unit, separated by the inferred faulted corridor.

4.5 **Discussion**

The locations of the previously proposed Bæverdalen and Tjellefonna faults (e.g. Gabrielsen and Ramberg 1979, Bryhni et al. 1990, Redfield et al. 2004, Redfield and Osmundsen 2009) are confirmed by our integrated geophysical study (Fig. 6 and 7). The Tjellefonna fault system comprises a master fault (i.e. the Tjellefonna fault *sensu stricto* depicted by anomalies S2, R2 and M2 in Fig. 6), surrounded by two (?) damage zones in the centre of the valley of Eidsøra (Fig. 7) and a secondary fault less than 1 km farther north (Fig. 8). Our dataset suggests that the core of the master fault is ~100-200 m wide and filled with water and/or clay minerals, hence presumably highly fractured and fault gouge rocks. As such, the structure of the core of the Tjellefonna fault appears to be similar to that of the Mulvik fault which is exposed ~10 km northeast of Eidsøra (Bauck 2010). From a quick glance at the topographic map, it can be seen that the two faults are not aligned and that the latter fault is probably a secondary structure of the former. Our geophysical measurements suggest a different nature for the secondary fault found farther north (Fig. 7). We interpret the observed high-magnetic signal and the gravity low to be associated with a fault core bearing similar petrophysical properties (i.e. high-magnetic susceptibility and low density, Table 1) to the indurated fault rocks from Tjelle and Mulvik (Biedermann 2010). If our interpretation is correct, a field analogue for this fault could be the Tjelle fault (Redfield and Osmundsen 2009). The Tjelle fault exposes mainly consolidated zeolite-rich breccias where the gneissic protolith is still evident and is interpreted to be a secondary structure of the Tjellefonna fault (Redfield and Osmundsen 2009). The width of our modelled fault zone (i.e. ~30 m) appears to exceed by one order of magnitude the width of individual fault zones mapped at the outcrop scale near Tjelle (Redfield and Osmundsen 2009, Bauck 2010).

In detail, the fault zone that we modelled most probably involves alternating 1 to 10 m-wide fault zones and intact rock as observed in the field by Bauck (2010).

Our 2D model (Fig. 7) suggests that the secondary fault dips steeply towards the south. Admittedly, we can only indicate the dip in the uppermost few hundred metres. However, our observations are in good agreement with both field observations on the Tjelle fault (Redfield and Osmundsen 2009) and seismic-reflection data (Lundberg et al. 2009), which increases confidence in our findings. An obvious difference between the Tjelle fault and our secondary fault is that the former reactivated foliation planes flanking an antiform (Fig. 5 in Redfield and Osmundsen 2009), whilst the latter apparently reactivated foliation flanking a synform (Fig. 5). The dip of the main fault of the Tjellefonna fault system can only be inferred from our resistivity data (Fig. 6b). Inversion of the data suggests that the northern edge of the fault core (i.e. R2 in Fig, 6b) is dipping steeply towards the south while the southern edge is subvertical. We carried out sensitivity tests by means of forward modelling and changing the dip directions of both edges. The geometry shown in Figure 6b is the most elegant one in terms of reproducing the results of our resistivity inversion. Considering that the metamorphic foliation, both at the regional and local scales, dips in general towards the south (Bryhni et al. 1990, Fig. 5) and that, without any exception, the faults of the MTFC whose internal architecture is exposed have been shown to reactivate the pre-existing structural grain (Grønlie et al. 1991, Séranne 1992, Watts 2001, Redfield and Osmundsen 2009, Bauck 2010), we feel that our interpretation of a south-dipping Tjellefonna fault is geologically sound.

The geophysical experiments suggest that the Bæverdalen fault is characterised by a wide corridor of deformation (i.e. ~700 m, Fig. 8) containing alternating ~50-100 m-wide zones of fault gouge, highly fractured (i.e. permeable) rock and relatively intact bedrock. This relatively wide deformation corridor points to significant displacements along the Bæverdalen fault (e.g. Scholtz 2002). The Bæverdalen fault is also associated with (1) a pronounced jump in apatite fission track ages (Redfield et al. 2004) and (2) marked gravity and magnetic gradients (Skilbrei et al. 2002, Nasuti et al. 2010b), adding support to the idea that it is one of the master faults of the MTFC. Note that when crossing the Bæverdalen fault, the regional magnetic gradient is visible in our ground data as a step of ~100 nT (Fig. 8b). The deformation corridor related to the Bæverdalen

fault reaches its northernmost extension at horizontal coordinate 1200 on profile ZZ' (Fig. 8), where highly resistive bedrock is encountered. An additional resistivity profile, acquired ~200 m farther north, confirms that the bedrock remains highly resistive, hence presumably intact, for at least a distance of 2 km from this specific location. In general and because they are prone to severe rotations, the hanging-walls of normal faults tend to be much more fractured than their footwalls (e.g. Fossen and Gabrielsen 1996, Berg and Skar 2005). Consequently, we interpret the highly resistive bedrock observed north of the Bæverdalen fault as being its footwall. A corollary of our interpretation is that the Bæverdalen fault dips to the south, in agreement with the local tectonic grain (Bryhni et al. 1990). Admittedly, this latter conclusion remains more uncertain than in the case of the Tjellefonna fault.

Our findings have implications for the ongoing debate on the origin of the Scandinavian Mountains, also termed the Scandes (e.g. Nielsen et al. 2009, Pascal and Olesen 2009, Gabrielsen et al. 2010). It has been proposed that the relief of Mid Norway reflects normal faulting along the major segments of the MTFC that occurred in the geological past (Redfield and Osmundsen 2009 and references therein). The high-topography beginning south of Langfjorden (Fig. 3) is interpreted by these authors to be the uplifted footwall of the Tjellefonna fault. This hypothesis requires a northward-dipping Tjellefonna fault, which is in obvious contradiction to our findings. The 'scarp retreat' model proposed by Redfied et al. (2005) relies on the interpretation of apatite fission track ages and, in particular, the abrupt age changes recorded when crossing the major lineaments of the MTFC. The recent publication by Redfield and Osmundsen (2009) of additional AFT ages shows a much more complex pattern, where significant age variations also occur parallel to the MTFC over relatively short distances (i.e. ~50 km). Although the 'scarp retreat' model is still appealing, the new AFT data and our own observations call for further refinements to this model.

4.6 Conclusions

Several geophysical datasets (i.e. refraction seismic, resistivity, magnetics and gravimetrics) have been acquired in order to image the respective depth structures of two major segments of the MTFC, the Tjellefonna and Bæverdalen faults. The

Tjellefonna fault *sensu stricto* is interpreted as a 100-200 m-wide zone of gouge and/or water-saturated, fractured bedrock dipping steeply to the south. This fault zone appears to be flanked by two additional but minor damage zones but only one of them can be determined with sufficient confidence. A secondary normal fault also dipping steeply to the south but involving indurated breccias has been detected ~1 km farther north. The Bæverdalen fault is interpreted as a ~700 m-wide and highly deformed zone involving fault gouge, densely fractured rocks and intact bedrock, embedded within the fault rock products, and as such it is probably the most important fault segment in the studied area and accommodated most of the strain during inferred Late Jurassic normal faulting. Our geophysical data suggest that the Bæverdalen fault dips steeply towards the south, in agreement with the average orientation of the local tectonic grain. In summary, our geophysical observations suggest, in turn, that the influence of Mesozoic normal faulting along the MTFC on landscape development is more complex than previously thought.

Reference:

Andersen, T.B., and Jamtveit, B., 1990. Uplift of deep crust during orogenic extensional collapse: a model based on field studies in the Sogn–Sunnfjord region, W. Norway. *Tectonics*, 9, 1097–1111.

Bauck, M. S., 2010. *Fault rock assemblages and fault architecture in the Møre-Trøndelag Fault Complex*. Unpublished MSc Thesis, NTNU Trondheim.

Berg, S.S., and Skar, T., 2005. Controls on damage zone asymmetry of a normal fault zone: outcrop analyses of a segment of the Moab fault, SE Utah. *Journal of Structural Geology*, 27, 1803-1822.

Bering, D., 1992. The orientation of minor fault plane striae and the associated deviatoric stress tensor as a key to the fault geometry in part of the Møre– Trøndelag fault zone, on-shore central Norway. In: Larsen, R.M., Brekke, H., Larsen, B.T. & Talleraas, E. (eds) *Structural and Tectonic Modelling and its Application to Petroleum Geology*. Norwegian Petroleum Society (NPF), Special Publications, 1, 83–90.

Biedermann, A.R., 2010. *Magnetic Properties of the Møre-Trøndelag Fault Complex*. MSc Thesis, ETH Zürich. http://e-collection.library.ethz.ch/view/eth:1986

Bøe, R., and Bjerkli, K., 1989. Mesozoic sedimentary rocks in Edøyfjorden and Beitstadfjorden, Central Norway: Implications for the structural history of the Møre–Trøndelag fault zone. *Marine Geology*, 87, 287–299.

Braathen, A., Nordgulen, Ø., Osmundsen, P.T., Andersen, T.B., Solli, A. & Roberts, D. 2000. Devonian, orogen-parallel, opposed extension in the Central Norwegian Caledonides. *Geology*, 28, 615–618.

Brekke, H., 2000. The tectonic evolution of the Norwegian Sea continental margin, with emphasis on the Vøring and Møre Basins. In: NØTTVEDT, A. (Ed.), Dynamics of the Norwegian Margin. Special Publication, vol. 167. *Geological Society of London*, pp. 327–378.

Bryhni, I., Austrheim, H., Bjørnstad, Kullerud, L., and Reksten, K., 1990. Bergrunnskart Tingvoll. 1320 1 1:50000. Foreløpig utgave. Geological Survey of Norway, Trondheim.

Dahlin, T., 1996. 2D resistivity surveying for environmental and engineering applications. *First Break*, 14, 275-284.

Fossen, H., and Gabrielsen, R. H., 1996. Experimental modelling of extensional fault systems by use of plaster. *Journal of Structural Geology*, 18, 673-687.

Gabrielsen, R.H. and Ramberg I.B., 1979. Fracture patterns in Norway from LANDSAT imagery: results and potential use. In: Proceedings of the Norwegian Sea Symposium, NSS/20, Tromsø. *Norwegian Petroleum Society (NPF)*, pp. 1-10.

Gabrielsen, R.H., Odinsen, T. and Grunnaleite, I., 1999. Structuring of the Northern Viking Graben and the Møre Basin; the influence of basement structural grain, and the particular role of the Møre-Trøndelag Fault Complex. *Marine and Petroleum Geology*, 16: 443-465.

Gabrielsen, R.H., Faleide, J.I., Pascal, C., Braathen, A., Nystuen, J.-P., Etzelmuller, B., and O'Donnell, S., 2010. Latest Caledonian to Present tectonomorphological development of southern Norway, *Marine and Petroleum Geology*, 27, 709-723.

Ganerød, G. V., G. Grøneng, J. S. Rønning, E. Dalsegg, H. Elvebakk, J. F. Tønnesen, V. Kveldsvik, T. Eiken, L. H. Blikra, and A., Braathen, 2008. Geological model of the Åknes rockslide, western Norway, *Engeering Geology,* 102(1-2), 1-18.

Grønlie, A., and Roberts, D., 1989. Resurgent strike–slip duplex development along the Hitra–Snåsa and Verran faults, Møre–Trøndelag Fault Zone, Central Norway. *Journal of Structural Geology*, 11, 295–305.

Grønlie, A., Harder, V. & Roberts, D. 1990. Preliminary fission-track ages of fluorite mineralisation along fracture zones, inner Trondheimsfjord, Central Norway. *Norwegian Journal of Geology*, 70, 173–178.

Grønlie, A., Nilsen, B., and Roberts, D., 1991. Brittle deformation history of fault rocks on the Fosen Peninsula, Trondelag, central Norway. *Norges Geologiske Undersøkelse Bulletin*, 421, 39–57.

Grønlie, A., Naeser, C.W., Naeser, N.D., Mitchell, J.G., Sturt, B.A., and Ineson, P., 1994. Fission track and K/Ar dating of tectonic activity in a transect across the Møre–Trøndelag Fault Zone, Central Norway. *Norwegian Journal of Geology*, 74, 24–34.

Hacker, B. R., T. B. Andersen, S. Johnston, A. R. C. Kylander-Clark, E. M. Peterman, E. O. Walsh, and Young, D., 2010. High-temperature deformation during continental-margin subduction & exhumation: The ultrahigh-pressure Western Gneiss Region of Norway, *Tectonophysics*, *480*(1-4), 149.

Hagedoorn J.G. 1959: The plus-minus method of interpreting seismics refraction sections. *Geophysical Prospecting* 7, 158-182.

Hurich, C. A. & Roberts, D. 1997: A seismic reflection profile from Stjørdalen to Outer Fosen, Central Norway: a note on the principal results. *Norges geologiske undersøkelse Bulletin* 433, 18-19.

Krabbendam, M., and Dewey, J.F., 1999. Exhumation of UHP rocks by transtension in the Western Gneiss region, Scandinavian Caledonides. In: Holdsworth, R.E., Strachan, R.A. & Dewey, J.F. (eds) Continental Transpressional and Transtensional Tectonics. *Geological Society, London, Special Publications*, 135, 159–181.

Loke, M. H., 2004. Tutorial: 2-D and 3-D electrical imagining surveys. 136p.

Lundberg, E., Nasuti, A. and Juhlin C., 2009. High resolution reflection seismic Profiling over the Møre-Trøndelag Fault Complex, Norway. Abstract, EGU Conference . Vienna, Austria.

Nasuti, A., Chawshin, K., Dalsegg, E., Tønnesen, J.F., Ebbing, J. and Gellein, J., 2009. Electrical resistivity and refraction seismics over a segment of the Møre-Trøndelag Fault Complex. *Norges geologiske undersøkelse* report 2009.037, 37p.
http://www.ngu.no/upload/Publikasjoner/Rapporter/2009/2009_037.pdf

Nasuti, A., Beiki, M., and Ebbing, J., 2010a. Gravity and magnetic data acquisition over a segment of the Møre-Trøndelag Fault Complex. *Norges geologiske undersøkelse* report 2010.049, 42p.
http://www.ngu.no/upload/Publikasjoner/Rapporter/2010/2010_049.pdf

Nasuti, A., Ebbing, J., Pascal, C., Tønnesen, J.F. and Dalsegg, E., 2010b. Using geophysical methods to characterize a fault zone: a case study from the Møre-Trøndelag Fault Complex, Mid-Norway. Extended abstract, EAGE conference, Barcelona.

Nettleton, L. L., 1939. Determination of density for reduction of gravimeter observations: *Geophysics*, **4**, 176–183.

Nielsen, S.B., Gallagher, K., Leighton, C., Balling, N., Svenningsen, L., Jacobsen, B.H., Thomsen, E., Nielsen, O.B., Heilmann-Clausen, C., Egholm, D.L., Summerfield, M.A., Clausen, O.R., Piotrowski, J.A., Thorsen, M.R., Huuse, M., Abrahamsen, N., King, C., Lykke-Andersen, H., 2009. The evolution of western Scandinavian topography: A review of Neogene uplift versus the ICE (isostasy-climate-erosion) hypothesis, *Journal of Geodynamics* 47, 72–95.

Olesen, O., Brönner, M., Ebbing, J., Gellein, J., Gernigon, L., Koziel, J., Lauritsen, T., Myklebust, R., Pascal, C., Sand, M., Solheim, D. and Usov, S., 2010. New aeromagnetic and gravity compilations from Norway and adjacent areas – methods and applications. *In Vining, B.A. & Pickering, S. C. (eds) Petroleum Geology: From mature basins to new frontiers. Proceedings of the 7th Petroleum Geology Conference. Geological Society of London, 559-586.*

Pascal, C., and Gabrielsen, R.H., 2001. Numerical modelling of Cenozoic stress patterns in the Mid Norwegian Margin and the northern North Sea, *Tectonics*, 20/4, 585-599.

Pascal, C., and Olesen, O., 2009. Are the Norwegian mountains compensated by a mantle thermal anomaly at depth? *Tectonophysics*, 475, 160-168.

Pascal, C., Roberts, D., and Gabrielsen, R.H., 2010. Tectonic significance of present-day stress relief phenomena in formerly glaciated regions, *Journal of the Geological Society of London*, 167, 363-371.

Popowski, T., Connard, G., and French, R., 2009: GM-SYS profile modeling, Gravity and Magnetic Modeling software for OasisMontaj—User Guide v 4.1.

Redfield, T.F., and Osmundsen, P.T., 2009. The Tjellefonna Fault system of Western Norway: Linking late-Caledonian extension, post-Caledonian normal faulting, and Tertiary rock column uplift with the landslide-generated tsunami event of 1756, *Tectonophysics*, 474, 106–123.

Redfield, T.F., Torsvik, T.H., Andriessen, P.A.M. and Gabrielsen, R.H., 2004. Mesozoic and Cenozoic tectonics of the Møre Trøndelag Fault Complex, central Norway: constraints from new apatite fission track data. *Physics and Chemistry of the Earth*, 10(29), 673–682.

Redfield, T.F., Osmundsen, P.T. and Hendriks, B.W.H., 2005. The role of fault reactivation and growth in the uplift of western Fennoscandia. *Journal of the Geological Society, London*, 162, 1013–1030.

Reynolds, J.M., 1997. *An Introduction to Applied and Environmental Geophysics*. John Wiley & Sons, New York, p. 796.

Roberts, D. & Myrvang, A. 2004. Contemporary stress orientation features in bedrocks, Trøndelag, central Norway, and some regional implications. *Norges geologiske undersøkelse Bulletin*, 442, 53–63.

Robinson, P., 1995. Extension of Trollheimen tectono-stratigraphic sequence in deep synclines near Molde and Brattvåg, Western Gneiss Region, southern Norway. *Norsk Geologisk Tidsskrift* 75, 181–198.

Scholz, 2002. *The Mechanics of Earthquakes and Faulting, Cambridge*, 471 p.

Séranne, M., 1992. Late Paleozoic kinematics of the Møre-Trøndelag Fault Zone and adjacent areas, central Norway. *Norsk Geologisk Tidsskrift 72*, 141-158.

Skilbrei, J. R., Olesen, O., Osmundsen, P. T., Kihle, O., Aaro, S., and Fjellanger, E., 2002. A study of basement structures and some onshore-offshore correlations in Central Norway. *Norwegian Journal of Geology,* 82, 263-279.

Tucker, R.D., Krogh, T.E., Råheim, A., 1990. Proterozoic evolution and age-province boundaries in the central part of the Western Gneiss region, Norway: results of U–Pb dating of accessoryminerals fromTrondheimsfjord to Geiranger. In: Gower, C.F., River, T., Ryan, B. (Eds.), Mid-Proterozoic Laurentia-Baltica. GAC special paper. *Geological Association of Canada, St. John's* Newfoundland, pp. 149–173.

Tveten, E., Lutro, O., and Thorsnes, T., 1998. Berggrunnskart Ålesund. 1:250000, (Ålesund, western Norway), Geological Survey of Norway, Trondheim (bedrock map).

Watts, L.M., 2001. *The Walls Boundary fault zone and the Møre-Trøndelag Fault Complex: a case study of two reactivated fault zones*. Unpublished PhD thesis, Department of Geological Sciences, University of Durham.

Westerdahl, H., 2003. Modellering av seismiske data over løsmassefylte depresjoner, svakhetssoner og ved kabelheng. *Norges Geotekniske Institutt . Intern rapport*, nr.2338

Chapter 5.   Paper III. High resolution reflection seismic profiling over the Tjellefonna fault in the Møre-Trøndelag Fault Complex, Norway

E. Lundberg[1], C. Juhlin[1], and A. Nasuti[2,3]

[1]Department of Earth Sciences, Uppsala University, Villav¨agen 16, 75236 Uppsala, Sweden
[2]Department of Petroleum Engineering and Applied Geophysics, Norwegian University of Science and Technology, 7491 Trondheim, Norway
[3]NGU, Geological Survey of Norway, 7491 Trondheim, Norway

ABSTRACT

The Møre-Trøndelag Fault Complex (MTFC) is one of the most prominent fault zones of Norway, both onshore and offshore. In spite of its importance, very little is known of the deeper structure of the individual fault segments comprising the fault complex. Most seismic lines have been recorded offshore or focused on deeper structures. This paper presents results from two reflection seismic profiles, located on each side of the Tingvollfjord, acquired over the Tjellefonna fault in the southeastern part of the MTFC. Possible kilometer scale vertical offsets, reflecting large scale northwest-dipping normal faulting, separating the high topography to the southeast from lower topography to the northwest have been proposed for the Tjellefonna fault or the Baeverdalen lineament. In this study, however, the Tjellefonna fault is interpreted to dip approximately 50–60° towards the southeast to depths of at least 1.3 km. Travel-time modeling of reflections associated with the fault was used to establish the geometry of the fault structure at depth, while detailed analysis of first P-wave arrivals in shot gathers, together with resistivity profiles, were used to define the near surface geometry of the fault zone. A continuation of the structure on the northeastern side of the Tingvollfjord is suggested by correlation of an in strike direction P-S converted reflection (generated by a fracture zone) seen on the reflection data from that side of the Tingvollfjord. The reflection seismic data correlate well with resistivity profiles and recently published near surface geophysical data. A highly reflective package forming a gentle antiform structure was also identified on both seismic profiles. This structure could be related to the folded amphibolite lenses seen on the surface or possibly by an important boundary within the gneissic basement rocks of the Western Gneiss Region. The fold hinge line of the structure is parallel with the Tjellefonna fault trace suggesting that the folding and faulting may have been related.

5.1 **Introduction**

The Møre-Trøndelag Fault Complex (MTFC), striking ENE–WSW, separates the northern North Sea basin system from the Møre and Vøring Basins (Brekke, 2000), and can be traced from the Møre County along the northern margin of the Western Gneiss Region (WGR) towards the Børgefjell Basement Window, where it dies out in a horsetail splay (Roberts, 1998). It consists of several marked major fault segments, e.g. the Hitra-Snåsa Fault (HSF) and the Verran Fault (VF) (Fig. 1). As one of the most prominent fault zones of Norway, both onshore and offshore, the MTFC has been studied frequently. Seismic lines have been recorded mainly offshore, e.g. Sommaruga and Bøe (2002) interpreted several seismic profiles from four inshore/nearshore areas, investigating the geometry and stratigraphy of mainly Jurassic sediments. Seismic profiles on land have focused on the deep crustal structure, e.g. Mykkeltveit (1980) and Hurich (1996). The MTFC has been important in controlling the landscape development both onshore and offshore as established by many authors, e.g. Grunnaleite and Gabrielsen (1995) and Osmundsen et al. (2006), and may still be seismically active today (Olesen et al., 2004), influencing the regional stress pattern of Norway (Pascal and Gabrielsen, 2001). Connecting the deeper structure of MTFC segments with geological observations on the surface is therefore important for understanding seismicity and landslides, as well as the geological/tectonic history of the region.

Although of major significance, the MTFC had not been investigated by geophysical methods on land until recently, aside from an onshore reflection seismic profile acquired on the Fosen Peninsula (Fig. 1) in the northeast (Hurich and Roberts, 1997). In 2008, an effort was initiated to better understand the nature of one of the onshore segments of the MTFC, the Tjellefonna fault (Fig. 1). The regional scale of the MTFC and its impact on the tectonic setting of middle Norway was studied using potential field data (Nasuti et al., 2012) along with a more detailed study (Nasuti et al., 2011), including DC resistivity soundings, refraction seismic, gravity and magnetic profiles and two reflection seismic profiles with focus on geophysical modeling of the Tjellefona fault and the Baeverdalen fault (Fig. 1). This paper goes into significantly more detail concerning the two reflection seismic profiles crossing the Tjellefonna fault.
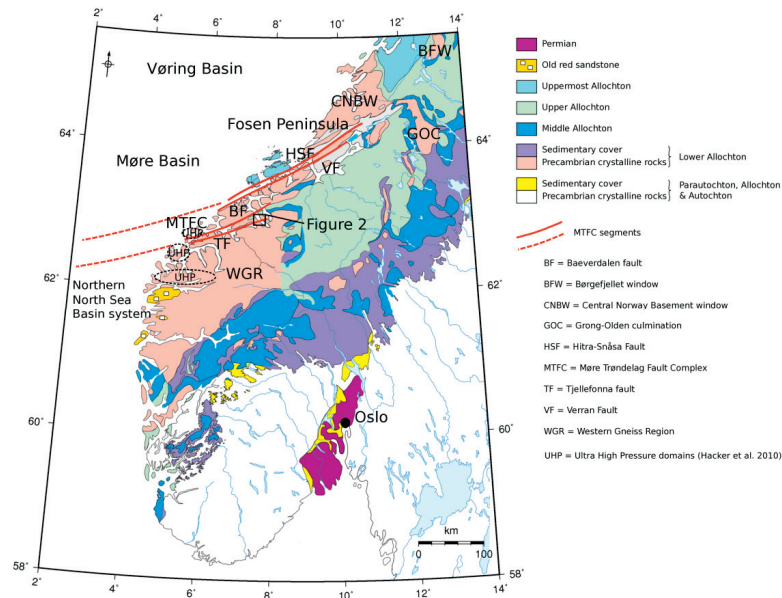
Fig. 1. Tectonostratigraphic map of southern Norway (modified after Mosar et al., 2002) showing the location of the study area in relation to the Western Gneiss Region and the important segments of the Møre-Trøndelag Fault Complex.

    The Tjellefonna fault follows a pronounced topographic lineament that runs along Langfjorden and continues past Eidsøra across the Tingvollfjord until Mulvik, and possibly farther northeast. Several fault localities have been mapped along this lineament and together these faults form a coherent fault system (marked in Figs. 1, 2 and 14 by a gray dashed line) paralleling Langfjorden (Redfield and Osmundsen, 2009). Based on apatite fission track data, Redfield et al. (2005a) indicated possible kilometer scale vertical offsets across the Baeverdalen lineament (here Baeverdalen fault, BF, in Fig. 1) and/or the Tjellefonna fault TF. These vertical offset were assumed to be reflecting northwest dipping normal faulting in the last 100 Ma just southeast of the MTFC, separating the high topography to the southeast from lower topography to northwest. The geometry of the Tjellefonna fault at depth was, however, not previously known. In order to better understand the development of the MTFC, it is important to know the geometry of the individual fault segments. In this paper seismic data and resistivity profiles are used to delineate the Tjellefonna fault at depth. The fault appears

to separate reflective bedrock to the northwest from less reflective bedrock to the southeast. The strike of the fault appears to be subparallel to the Fold Hinge line of an antiform defined by a reflective package seen on both seismic profiles (S.P. 1 and S.P. 2) at 0.5 km and 1 km depth, respectively.
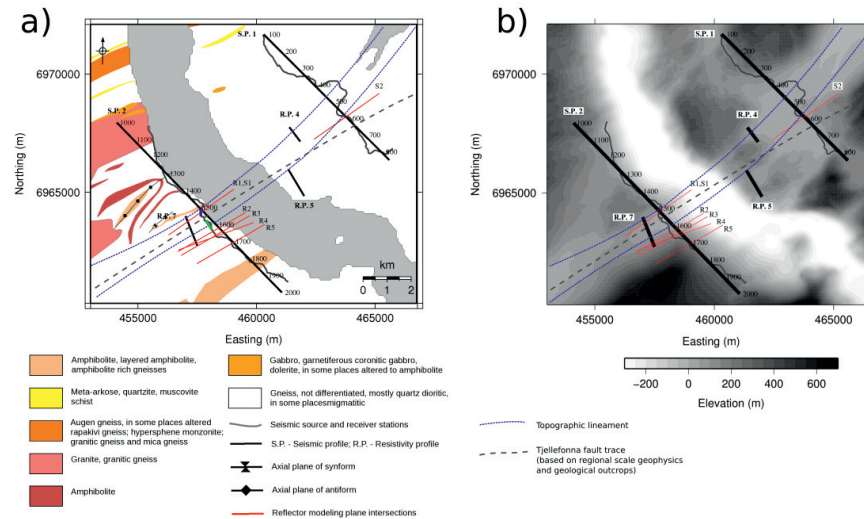
Fig. 2. (a) Simplified geological map after Tveten et al. (1998). S.P – Seismic Profile; R.P – Resistivity Profile; Green zone – LVA; Blue zone – LVB see text for explanation. (b) Topography of the study area. The topographic low is seen between the blue dashed lines on both figures. The thicker gray dashed line indicates the Tjellefonna fault trace based on geological outcrops and regional scale geophysics (Nasuti et al., 2012).

5.2 **Geological setting**

Our study area is located within the Western Gneiss Region (WGR) of Norway. The WGR is the lowest tectonic unit in the Scandinavian Caledonides (Andersen and Jamtveit, 1990) and is generally a topographic high in Norway displaying pronounced ENE–WSW topographic lineaments (many interpreted as fault zones), following the main Caledonian fabric. The WGR is composed of Fennoscandian gneisses, mainly 1650–950 Ma orthogneisses (Austrheim et al., 2003; Skår and Pedersen, 2003) that were reworked and exhumed in the final stage of the Caledonian Orogeny (i.e. Scandian Phase). The WGR gneisses are structurally overlain by continental and oceanic allochthons. These rocks were down-folded into the basement gneisses and can now be observed as long lobes and tongues extending E–W to ENE–WSW (Braathen et al.,

2000; Terry and Robinson, 2003; Hacker et al., 2010). In our study area both gneissic foliation and lobes of Caledonian allochthons, as well as topographic lineaments, extend in the ENE–WSW direction. The exposed rocks are sometimes folded with fold hinge lines directed ENE–WSW with steeply southeast dipping structures showing the same strike direction (Fig. 2). The folded rocks occur on the northwestern side of the Tjellefonna fault trace, while the rocks on the southeastern side show steeper dips.

The WGR experienced high pressure metamorphism in the Silurian-Devonian continent–continent collision and several ultra high pressure (UHP) terranes, surrounded by high-pressure rocks, have been identified within the WGR (e.g. Wain, 1997; Hacker et al., 2010). Peak metamorphic temperature and Scandian deformation intensity are both increasing towards the northwest (Hacker et al., 2010). In western Norway, detachment zones separating the lower crust from the middle and upper crust can be observed and these comprise 2 to 3 km thick mylonites with a complex geometry consisting of anastomosing high strain zones (Andersen and Jamtveit, 1990).

The MTFC probably formed during the Scandian Phase (Grønlie and Roberts, 1989). Main phases of activity include early Devonian sinistral strike-slip, early Permian sinistral transtension, late Jurassic normal to dextral strike-slip faulting (Grønlie and Roberts, 1989; Séranne, 1992; Sherlock et al., 2004) and, presumably, Cenozoic normal dip-slip (Redfield et al., 2005b). These phases reflect the collapse of the Caledonian mountain chain, widespread Permian rifting, late Jurassic rifting of the northern North Sea and the mid Norway margin (Gabrielsen et al., 1999) and Cenozoic uplift of the Norwegian mountains while offshore basins were subsiding (Faleide et al., 2002; Redfield et al., 2005b).

5.3 **Data acquisition**

The reflection seismic profiles (S.P.) were acquired in June 2008. The seismic profiles extend approximately 7.3 km (S.P. 1) and 8.9 km (S.P. 2), respectively, on each side of the Tingvollfjord (Fig. 2). A VIBSIST mechanical source system was used to generate the seismic waves (see e.g. Cosma and Enescu, 2001 for further details). This system has proven to be useful for imaging fault zones, deformation zones and the upper crust in crystalline environments (e.g. Dehghannejad et al., 2010; Juhlin et al.,

2010; Juhlin and Lund, 2011; Lundberg and Juhlin, 2011). The system consists of a hydraulic breaking hammer mounted on a tractor or excavator. Although relatively mobile, profiles are generally required to follow roads or trails, normally resulting in crooked recording geometries. This was especially true for S.P. 1 north of the Tingvollfjord and which resulted in a severely crooked profile in the central parts (Fig. 2). Soft ground conditions sometimes reduced the quality of recorded seismograms due to bad coupling between the source and the ground. Some source points also had to be skipped due to wet and soft ground conditions. These included the last 1200 m of S.P. 1, to the northwest, and also approximately 900 m in the central parts of S.P. 2. Another reason for skipping source points in some areas was the proximity to buildings and farms housing animals. Gaps in the recording geometry mostly affect the quality of the refraction statics corrections, but they also lower the fold and, thereby, reduce the signal to noise ratio in the final stacked sections. An uneven offset distribution may also effect the processing. In spite of this, the recorded seismic data were of sufficient enough quality to produce interpretable stacks on both sides of the Tingvollfjord. Acquisition parameters are listed in Table 1.

The 2-D-resistivity profiles (R.P. in Fig. 2) were acquired according to the Lund system (Dahlin, 1996). Data were collected with a gradient array configuration with electrode spacing of 10 and 20 m to map the shallow and deeper parts of the profiles, respectively. The depth penetration is approximately 130 m, with reliable data coverage to approximately 70 m depth.

Table 1. Acquisition parameters.

Parameter	Value
Source	VIBSIST 1000 mechanical source system
Source interval	20 m
Geophones	28 Hz single
Receiver spacing	20 m
Instrument	SERCEL 408 UL
Active channels	300
Sample rate	1 ms

5.4 Processing

Careful processing was required due to the seismic lines following crooked profiles and rugged terrain. Especially the northeastern part of S.P. 1 had a large spread in the midpoints in the central part of the profile due to its crookedness (Fig. 2). This large midpoint spread has a significant influence on the possibility to stack reflections coherently. Two sections on S.P. 1 (between CMP 400–450 and 520–550), where the recording line is approximately perpendicular to the stacking line (and hence parallel to structural trends), have clear reduced coherency in the reflections (Fig. 3). To properly image both steeply dipping reflections as expected from the fault zone itself, as well as sub-horizontal reflections from flat lying structures, a dip moveout correction (DMO) is usually required. DMO could, however, not be applied successfully, most likely due to large fold variations along the profiles and the large spread of midpoints for each CMP bin. If DMO is not applied, steeper reflections will stack with a higher normal moveout velocity. In S.P. 2, steep reflections in the southeastern part of the stack were visible when a high normal moveout velocity was applied (Fig. 4b). Since the strongest sub-horizontal reflectivity is observed in the northwestern part of the stack (Fig. 4a), and DMO processing was unsuccessful, we produced two separate stacks of S.P. 2 that were merged before interpretation. The seismic data were stacked first with lower normal moveout velocities, in the range of true bedrock velocities, in order to enhance sub-horizontal reflections. For the second stack, higher normal moveout velocities were used in order to enhance the steeply dipping reflections.

Refraction static corrections are usually one of the most important steps of reflection seismic processing in environments where low velocity loose sediments are present on top of high velocity bedrock (e.g. Juhlin, 1995), as is common in the crystalline environments in Scandinavia. However, the skipping of several source points in the central parts of the profiles, causing large gaps in the source records, reduced the accuracy of the refraction statics calculation for these parts. Such gaps occur between source points 198 and 245, corresponding to CMP:s 1550 to 1635 in S.P. 2 and also in several sections of S.P. 1. These gaps, together with the large spread of midpoints, most likely causes the lower signal to noise ratio on S.P. 1 (Fig. 3). Figures 5 and 6 show examples of shot-gathers and how the pre-stack processing enhanced the signal quality.

Reflections are clearer in the processed shot-gathers compared to the raw gathers. All processing steps are outlined in Table 2.
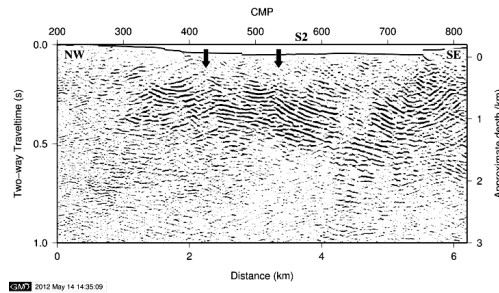
Fig. 3. Final migrated stack of S.P. 1 with marked position of reflection S2 (see also Fig. 8a). Arrows mark sections affected by sharp bends in the recording line (compare with Fig. 2). Elevation marked on top. Length to depth ratio approximately 1:1.

Table 2. Processing steps.

Step	Parameters
1	Decoding raw shot-gathers using shift and stack procedure
2	Geometry check/correction
3	Trace edit
4	Pick first break
5	Refraction statics: floating datum 200 m replacement velocity $5100 \, \mathrm{m\,s^{-1}}$
6	Remove 50 Hz noise
7	Spectral equalization: 15 25 140 180
8	AGC 100 ms window
9	Deconvolution
10	Band-pass filter 15 25 140 180
11	Remove first arrival energy
12	AGC 100 ms window
13	Residual statics
14	Normal Move Out correction 50 % stretch mute
15	Stack
16	Floating datum statics
17	Band-pass filter 25 35 95 120
18	FX-decon
19	Band-pass filter 25 35 95 120
20	FD-migration: constant velocity $5500 \, \mathrm{m\,s^{-1}}$
21	Band-pass filter 25 35 95 120

One of the benefits of crooked lines with a midpoint spread around the stacking line is that further possibilities for interpretation are available, since the traces map a 3-

D volume rather than just a 2-D slice. Therefore, we tested both an azimuthal binning procedure and a cross-dip analysis method, as described in e.g. Lundberg and Juhlin (2011). These tests were designed to improve the coherency of reflections that originate from out-of-the-plane of the profile. The tests, however, did not show any improved image compared with the standard stacking procedure, indicating that the imaged structures in Figs. 3 and 4 strike nearly perpendicular to the stacking line.

Crooked line recording geometries often result in that reflections in shot-gathers may be difficult to follow since the receiver offsets are often irregular. Reflection travel-time modeling was, therefore, performed to better understand the geometries of reflectors and link the reflections visible in source gathers with reflections in stacked sections and to the near surface. Travel-times were calculated (using a constant velocity ray tracing code, see Ayarza et al., 2000, for details) for different reflector geometries and the resulting travel-times were visually compared with reflections seen in source gathers and stacked sections. The calculated travel-times with the best-fit to real data provide an approximate geometry and position of the structure causing each modeled reflection.
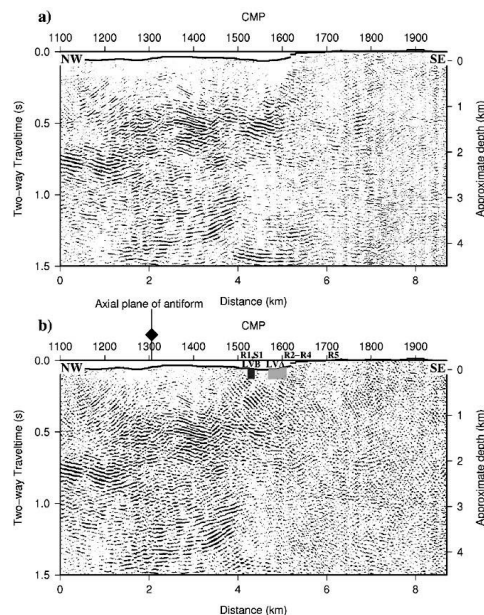
Fig. 4. (a) Final migrated stack of S.P. 2. (b) Final migrated stack of S.P. 2 merged with migrated stack using high stacking velocities. Green zone – LVA; Blue zone – LVB see text for explanation. Reflections S1 and R1–R5 marked. Location of axial plane of antiform from geology map (Fig. 2) also marked. Elevation on top. Length to depth ratio approximately 1:1.

The modeling assumes a planar reflecting surface and a constant bedrock velocity. Neither of these assumptions is expected in the real case, but by changing the dip or the strike of the modeled reflector planes in small increments and comparing the travel-times with the recorded data, a reasonable fit of travel-times could still be achieved, giving us approximate reflector geometries. Since the stacked sections are in 2-D and the modeling uses the 3-D configuration of sources and receivers, there is some room for error in fitting the travel-times with the stacked data. However, since the data are also compared with shot-gathers, the fitting of modeled travel-times will be more sensitive. The travel-time modeling is generally more sensitive to the dip of the modeled reflector plane as compared to the strike. The chosen strike directions can be shifted at least $5°$ with results still in a reasonable fit to the recorded data. Using appropriate strikes and dips, the corresponding modeled planar surfaces for each reflection (R1–R5) can be projected onto the geological map (Fig. 2). A constant bedrock velocity of 5200 m s^{-1} was used for all modeling. The reflection modeling employed also allows for calculating reflection coefficients and reflection depth points. These calculations have been used for interpreting the origin of the reflections and the depth extent of the reflectors.
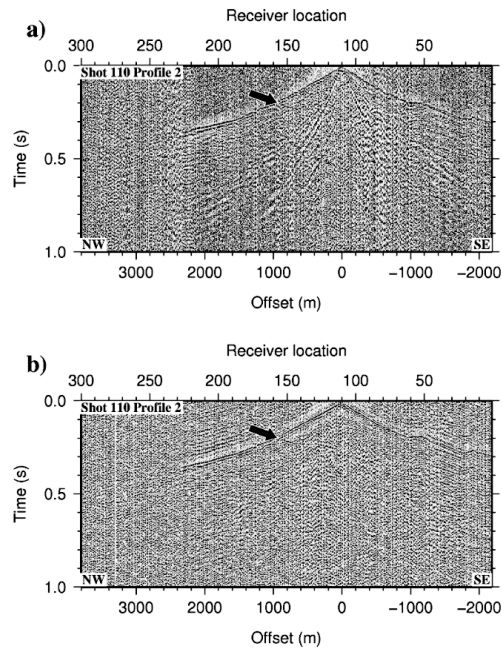
Fig. 5. (a) Raw shot-gather (agc 100 ms window and high pass filter (10 20) was used) from S.P. 2. (b) The same shot-gather processed until step 10 + step 12 and 17. Black arrow marks reflection more clearly seen in the processed shot-gather.

For the 2-D resistivity profiles, we processed and inverted the data using the RES2DINV (version 3.55) software (Loke, 2004). This software lets the operator have full control on data quality, giving the possibility to remove bad data points to improve overall data fit. The measured apparent resistivities with different electrode configurations were converted into 2-D true resistivity profiles. Further details can be found in Nasuti et al. (2009).

5.5 Results

5.5.1 Stacked sections

The strongest reflectivity in S.P. 2 (Fig. 4) forms a gentle antiform between CMP 1100 and 1600 with the hinge located close to CMP 1300 in the near surface. The fold axis from geological map is well correlated with the fold axis in the seismic section (Fig. 2). In the southeastern part of S.P.2, several steeply southeast dipping reflections

are visible and seem to project to the surface between CMP 1500 and 1700. Travel-time modeling of these reflections has been performed. Reflections R1–R5 are all visible on shot 95 from S.P. 2 (Fig. 6), however, additional shot-gathers have been used for constraining the modeled reflector geometry. The calculated travel-times are marked in Fig. 6c and in the unmigrated stacked section (Fig. 7b). Results of the travel-time modeling are given in Table 3. The surface projections of each reflection with the appropriate strike are also marked on the geological map (Figs. 2 and 14). The steep reflection R1 seems to extend down to about 0.9 s, or approximately 1.3 km (using a bedrock velocity of 5200 m s^{-1} and a dip of 55°), in the unmigrated section (Fig. 7). This depth coincides with the approximate maximum depth to where a reflection with that geometry can be traced without extending the existing seismic profile to the southeast. Reflections R3 and R4 are not as well correlated in the stacked section. This is due to that these reflections are best seen in the near surface on shot-gathers and in deeper parts in the stacked section, which makes the fitting of travel-times more difficult. Northwest dipping reflectivity indicated by a black arrow is seen in Fig. 6b. This reflectivity corresponds to the reflectivity between CMP 1750 and 1800 at approximately 0.5s in S.P. 2 Fig. 4a) and may be the continuation of the reflective package, forming the antiform further northwest.

The stack from S.P. 1 (Fig. 3) shows a disrupted reflective package that seems to form a folded structure, resulting in an antiform with a hinge around CMP 450 at about 0.2 s (ca. 0.5 km depth). This structure can be defined between CMP 300–700. The disruptions in this reflective package are most likely caused by the sharp bends in the acquisition line (Fig. 2).
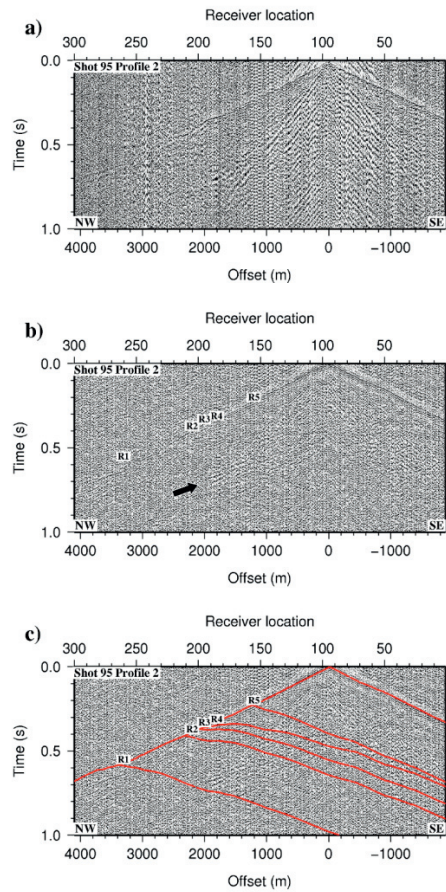
Fig. 6. (a) Raw shot-gather (agc 100 ms window and high pass filter (10 20) was used) from S.P. 2. (b) The same shot-gather processed until step 10 + step 12 and 17. The northwest dipping reflection marked with black arrow correspond to the reflections seen between CMP 1750 and 1800 at about 0.5 s TWT in the stacked section (Fig. 4a). (c) The processed shot-gather with calculated travel-times for reflections R1–R5 plotted.

Table 3. Modeling results.

Reflector	Strike	Dip
R1	55	55 SE
R2	60	55 SE
R3	60	53 SE
R4	70	50 SE
R5	60	65 SE
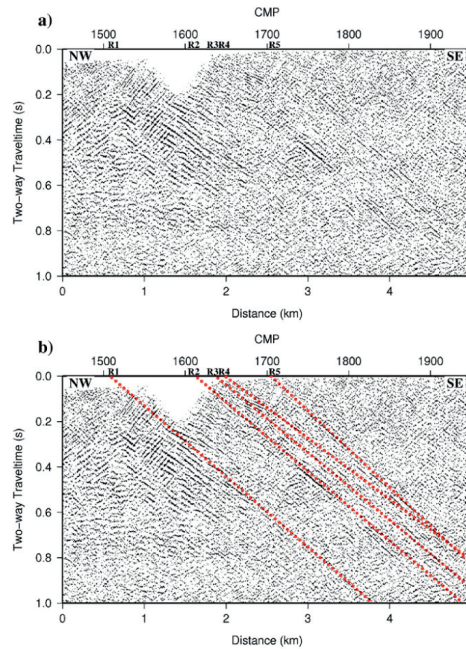
Fig. 7. Parts of unmigrated stack of S.P. 2 using high stacking velocities. (a) Without and (b) with calculated travel-times for reflections R1–R5 plotted.

5.5.2 Source-gather analysis and modeling

Two divergent reflections come to the surface in the central parts of both reflection profiles (Fig. 8). These reflections appear only in a few shots and are most visible at offsets of about 2 km. Reflection S1 on S.P. 2 is visible between receivers 215 and 255 with a gap between receivers 225 and 240. Reflection S2 on S.P. 1 is only visible for about 300 m (on 15 geophones). It is therefore difficult to perform accurate travel-time modeling of these reflections. Modeling, however, clearly shows that S1 is not a P-P reflection from a reflector with a similar geometry to the R1–R5 reflectors. In fact it was not possible to find any suitable reflector geometry that could fit the travel-times of S-1 when a P-P reflection was considered. Therefore, other options had to be tested. Figure 9 shows calculated travel-times for two different scenarios. In Fig. 9, travel-times from a P-P reflection from an 80° southeast dipping reflector are compared with travel-times from a P-S converted reflection from a reflector with the same geometry as the R1 reflection. The P-S converted reflection travel-times most closely fit

the real data (Fig. 9c). Angle dependent reflection coefficients were also calculated in order to understand why the P-S reflection is most apparent in the observed offset range and, perhaps also, to provide a clue as to the origin of the reflection. P-P and P-S reflections from two fault zones (FZ), with different V_p/V_s ratios, and from a mafic rock are compared in Fig. 10. The calculations are based on the same geometry as used for reflection R1 with rock parameters defined in Table 4. The 2-D sketch (Fig. 11) of the P-P and P-S ray tracing (although the 3-D geometry was used in the calculations) illustrates the different ray paths used. The angle of reflection is smaller than the incidence angle for the P-S converted ray path, since the S wave velocity is lower than the P wave velocity. The seismic velocities are typical values from laboratory measurements on rock samples collected along S.P. 2 (A. Nasuti, unpublished data, 2009).
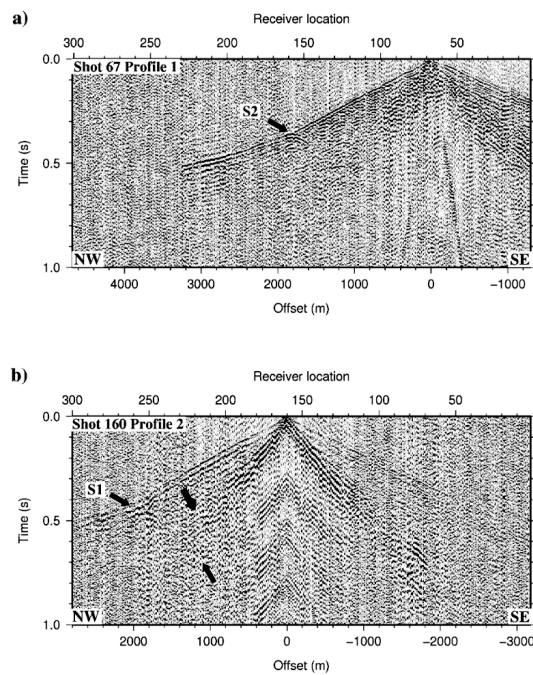
Fig. 8. P-S converted reflections (S2 and S1) in raw shot-gathers on both S.P. 1 (a) and S.P. 2 (b). Dark gray arrow indicates where surface waves disappear.

The slowest velocity (perpendicular to foliation) was used and the host rock is assumed to be intact gneiss. Densities are averages from rock samples collected by Biedermann (2010). The magnitude of the reflection coefficient is used for easier comparison of both positive and negative polarity reflections. In the interval where the P-S converted reflection is visible (receivers 215–255) a P-S reflection from a fault zone with a high V_p/V_s ratio (1.8) has amplitudes almost as high as a P-P reflection from a mafic rock. The reflection coefficient from a P-P reflection from a fault zone with a high V_p/V_s ratio (1.8) in the same interval is low, implying that it is unlikely to see the P-P reflection in this interval, but the P-S reflection should be strong. Since the P-S converted travel-time modeling fits the real data better than a steeply dipping P-P reflection and that a stronger P-S reflection than a P-P reflection can be expected with this reflector geometry, it is reasonable to assume that S1 is the P-S converted reflection from the same reflector as R1 and that these reflections originate from a fault zone boundary.
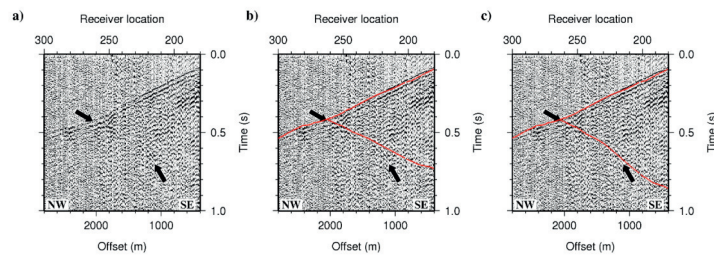
Fig. 9. Comparison of travel-time modeling of reflection S1. (a) without travel-time modeling (b) P-P reflection from a steeply dipping boundary strike 55° and dip 80°. (c) P-S reflection from a boundary with strike 55° and dip 55° (same geometry as for reflection R1).
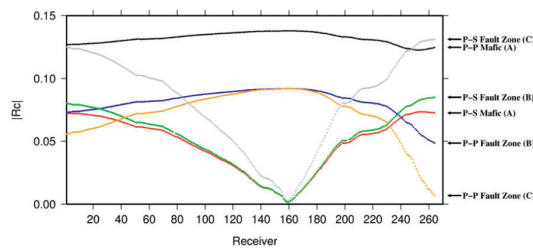
Fig. 10. Comparison of magnitude of reflection coefficient (|Rc|) for different reflecting boundaries. Geometry of boundary as for reflection R1 (strike 55° and dip 55°) and properties of rocks as defined in Table 4.

Table 4. Rock parameters used for calculating reflection coefficients. Velocities are typical values from laboratory measurements on rock samples collected along S.P. 2 (A. Nasuti, unpublished data, 2009). The slowest velocity (perpendicular to foliation) was used and the host rock is assumed to be an intact gneiss. Densities are averages from rock samples collected by Biedermann (2010).

	A. Gneiss (1)/ Mafic (2)	B. Gneiss (1)/ Fault Zone (2)	C. Gneiss (1)/ Fault Zone (2)
V_{P1} (m s^{-1})	4400	4400	4400
V_{S1} (m s^{-1})	2750	2750	2750
V_{P1}/V_{S1}	1.6	1.6	1.6
Density1 (kg m^{-3})	2700	2700	2700
V_{P2} (m s-1)	5600	3800	3800
V_{S2} (m s^{-1})	3200	2375	2100
V_{P2}/V_{S2}	1.75	1.6	1.8
Density2 (kg m^{-3})	2800	2600	2600

In between reflections R1 and R2 (Fig. 4b), two zones display a sharp delay in first arrival times indicating lower velocity in these areas (Fig. 12). We name these zones low-velocity zone A and B (LVA and LVB). The delay in LVB is 0.025 s over a distance of 160 m and the delay in LVA is 0.040 s over a distance of 390 m (Fig. 12). These zones are clearly visible on many shot gathers, and their respective positions correlate well between shot-gathers from the northwestern side of the zones. However, when comparing the position of these zones on shots from the opposite (southeast) side, a slight shift of the positions towards southeast occurs. The locations from shot-gather 302 (Fig. 12) was used to outline these zones on the stacked sections. In addition to significant delays in the first arrivals across these zones, the ground roll also disappears when approaching these zones. This effect is clearly seen in shot 302 where ground roll disappears around receiver 265 (Fig. 12) and in shot 160 (Fig. 8b) where ground roll disappears around receiver 210, corresponding approximately to the southeastern boundary of LVA. No sources were activated in LVA due to soft ground conditions.

5.5.3 Resistivity profiles

The resistivity profiles are interpreted here for the purpose of correlating the observed reflections and the shallow subsurface. Two not previously published resistivity profiles (R.P. 4 and R.P. 5 in Fig. 13) are marked with some possible fault locations. In the inverted profiles, relatively low-resistive zones may indicate fractured and/or water saturated bedrock, while more resistive zones are diagnostic of intact bedrock. Particularly low resistivity (i.e. lower than 1000 Ωm) characterizes clay-filled

fractures and, consequently, also fault gouge (e.g. Ganerød et al., 2008). R.P. 4 is located in the topographic low and shows a sharp lithological contrast (see Figs. 2 and 14).
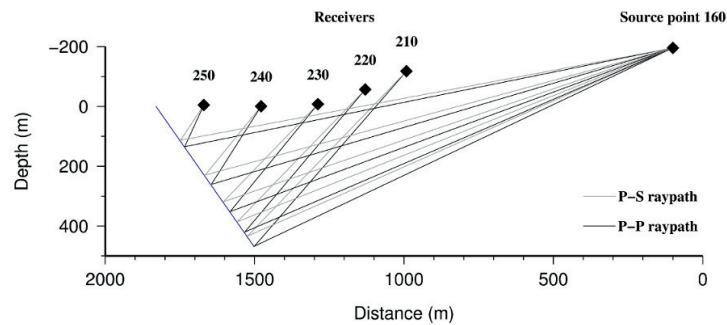
Fig. 11. 2-D sketch of the selected ray paths for a model with a plane dipping 55°. The angle of reflection is larger than the incidence angle for the P-S converted ray path, since the S wave velocity is lower than the P wave velocity. The reflection point for receiver 210 is located at approximately 425 m depth for a P-S converted reflection.
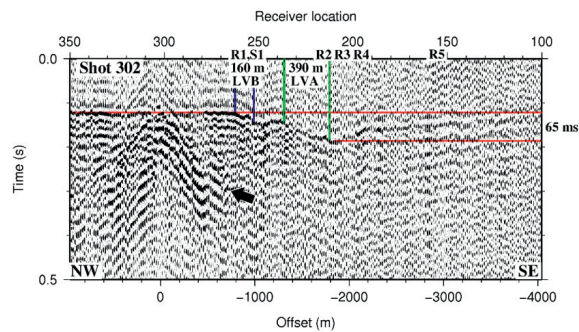
Fig. 12. Shot-gather 302 from S.P. 2 plotted using a reduction velocity of 5000 m s^{-1} and without refraction statics correction. Two zones display a sharp delay in the first arrivals and are marked as LVA and LVB. Total accumulated delay is 65 ms across the two zones. Southeast dipping reflections S1, R1– R5 not seen in this shot-gather, are marked. Black arrow indicates where surface waves disappear.

R.P. 5 has three low resistivity zones marked (P1–P3). R.P. 7 (Nasuti et al., 2011) has now been reinterpreted based on the correlation with the reflection seismic profiles. The northernmost zone (marked P6 in Fig. 13) has been extended with a southeasterly dip. P6 shows a direct correlation with reflections R1, S1 and S2 in the seismic sections (see Figs. 13 and 14). P3 on R.P. 5 possibly correlates with P4 on R.P. 7 (see Figs. 13 and 14).
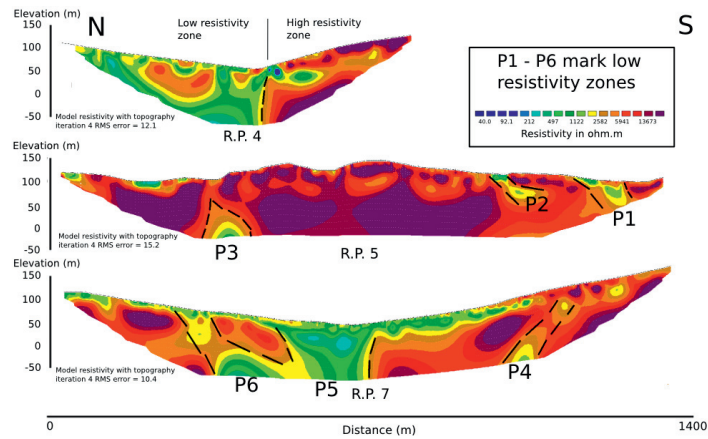
Fig. 13. Resistivity profiles 4, 5 and 7 (R.P. 7 reinterpreted from Nasuti et al., 2011). For low resistivity zones marked P1–P6 see text for discussion. Length to depth ratio approximately 1:1
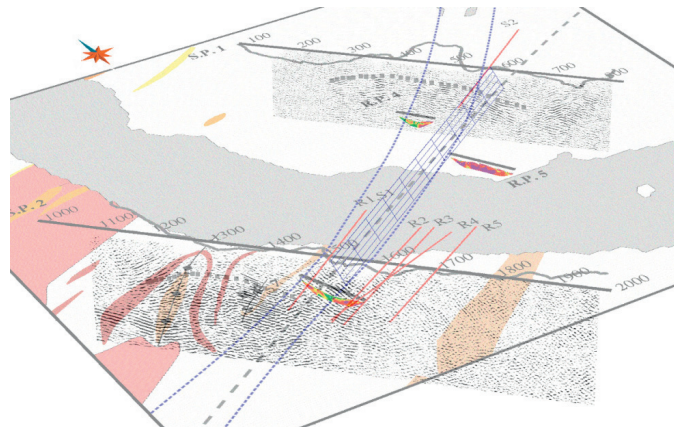
Fig. 14. Seismic profiles 1 and 2 and resistivity profiles 4, 5 and 7 plotted with geology in 3-D perspective view. Blue dashed lines indicates topographic lineament and red solid lines mark reflections S2, S1/R1–R5. See Fig. 2 for locations. The blue plane indicates the modeled fault plane with strike 55∘ and dipping 55∘ towards south east. The plane extends to 400 m depth in this figure. Antiform structures are enhanced with gray squares. The fold hinge line seems to be subparallel to the fault plane.

5.6 Discussion

The main topographic low and the Tjellefonna fault trace (from regional scale geophysics and outcrops) crosses S.P. 2 between CMPs 1500 and 1600, see Figs. 2 and 14. The most likely reflections that may be associated with the Tjellefonna fault are, therefore, reflections R1/S1 and R2. The overall reflectivity pattern can also be used to

separate reflective rock to the northwest of CMP 1550 in S.P. 2 from less reflective rock to the southeast. This difference in reflectivity may be due to a more suitable reflector geometry to the northwest (i.e. flat lying structures), as compared to the steeper structures towards southeast. This change of geometry can be explained by the presence of a steep fault zone. Our modeling indicates that R1 is a P-P reflection and S1 a P-S reflection off a fault zone, assuming reasonable input was used in the modeling and the reflection coefficient calculations. Fracturing and chemical alteration of rock results in lower V_p and V_s and in an increase in the V_p/V_s ratio (e.g. Moos and Zoback, 1983). The V_p/V_s ratio seems to be the most important factor for explaining the strong P-S reflection and the missing (below noise level) P-P reflection in the traces close to where the reflector intersects the surface. At the offsets of interest, fracture zone (C), with a V_p/V_s ratio of 1.8, clearly shows a much larger P-S reflection coefficient than fracture zone (B), with a V_p/V_s ratio of 1.6 (Fig. 10). Note that the host gneissic rock is assumed to have a V_p/V_s ratio of 1.6. The reflection coefficient of a P-S reflection from the mafic rock is almost at the level of the P-S reflection from fracture zone (B), but the modeled strong P-P reflection for the mafic rock is not observed in the data (Fig. 8b). Therefore, we interpret the reflector generating reflections R1/S1 to be a fracture zone with a high V_p/V_s ratio (fluid filled). The reflection point for the reflected energy of S1 at receiver 210 at about 0.7 s TWT can be calculated. It is located at a depth of approximately 425m and indicates the minimum depth extent of the fracture zone. A possible deeper extension of the fault zone to approximately 1.3 km is suggested when tracing the P-P reflection in the stacked section.

Reflection S2 on S.P. 1 has a very similar character as to S1 on S.P. 2 and is located in the strike direction of S1 (Fig. 2). The same reflector geometry as for R1/S1 gives a reasonable fit for a P-S converted reflection, but a corresponding P-P reflection is not seen in the stacked section. If the reflector is steeper on this profile it may explain why it is not imaged on the stacked section. Another possibility is that S.P. 1 is too short towards the southeast to properly image the deeper part of the fault zone. It is reasonable to assume that the Tjellefonna fault continues in the strike direction of reflection S1. The strike of the fault is then also in agreement with previous large scale interpretation of potential field data (see Fig. 7 in Nasuti et al., 2012).

The low velocity zones LVA and LVB are interpreted from shot-gathers without refraction static corrections. Different possible causes for the delays must, therefore, be considered: (1) an increase in the thickness of the low velocity sedimentary cover; (2) a decrease in velocity in the sedimentary cover; (3) a decrease in the bedrock velocity. A decrease in bedrock velocity would be expected across a fracture zone. The lack of ground roll in these zones may be due to changing properties in the sedimentary cover. Alternatively, if the bedrock is heavily fractured and water filled, then ground roll will also be largely attenuated across such a zone. If the delays are caused only by the sedimentary cover, then a quick recovery of the arrival times outside of the zones is expected. This can be seen in Fig. 12 between receivers 195 to 210. There is, however, some delay that is not recovered until at least receiver 100. This remaining delay is about 0.040 s and is more likely due to decreased bedrock velocity. The soft ground conditions found between receiver 198 and 245 during acquisition could indicate that LVA is due only to changes in the sediment cover properties. The remaining delay is, however, larger than the delay in LVB alone (0.025 s) and, therefore, some delay caused by lower bedrock velocity in LVA is also required to fully explain the large total delay. Most likely, LVA and LVB are both low velocity zones with a decreased bedrock velocity, indicating fractured bedrock.

Nasuti et al. (2011) showed the existence of south dipping or sub-vertical fault zones (R.P. 7) approximately 700 m to the southwest (Figs. 2 and 13). Refraction seismic and resistivity profiles indicated two well correlated low velocity/fractured zones. LVA correlates fairly well with the central fracture zone indicated by Nasuti et al. (2011), here P5 (Figs. 13 and 14). The width of LVA is about 390 m, while Nasuti et al. (2011) interpreted the central fault zone to be in the 100–200 m range. The width of LVA may be influenced by the sediment cover and the true width may be less than 390-m. LVB correlates very well with the northwestern most low resistivity zone, here P6 (Figs. 13 and 14). A southeasterly dip of LVB seems to correlate with a possible extension of the low resistivity zone. The width of LVB (160 m) is not influenced by a thick sediment cover, as is LVA, and the mapped width is probably close to the true width of the fractured bedrock. The width of LVB is also similar to the width of the low resistivity zone P6 on R.P. 7. A further consequence of our extended interpretation is that the fracture zones from the resistivity profiles may be connected at a deeper level,

and that they converge into a single wider fault zone causing the reflectivity seen in the reflection seismic stack. stack. P5 and P6 appear to merge into one zone already at a depth of 100 m (Fig. 13).

The strongest reflections in crystalline bedrock environments often correlate with fracture zones (e.g., Green and Mair, 1983; Juhlin and Stephens, 2006) or mafic sheets (e.g., Juhlin, 1990). Reflection R1/S1 can be interpreted as originating from a fracture zone. However, the character of reflections R2–R5 appears different from R1/S1. Reflection R1 is rather weak and discontinuous, while reflections R2–R5 are stronger and more continuous (Fig. 7). Although no geologic correlation to amphibolite rich gneiss or inter-layered mafics can be made for reflections R2–R5, it is possible that these reflections originate from such rocks since they are present in the area. Nasuti et al. (2011) also observed and sampled amphibolites outside the reported area, indicating a lack of detail in the geological maps. The R2–R5 reflections may, however, also represent secondary fracture zones. Secondary fracture zones are indicated in the shallow subsurface by the low resistivity zones P1–P3 in R.P. 5 (Figs. 13 and 14).

The strongest reflectivity in the area corresponds to gentle antiform structures which have a similar shape on both seismic profiles (Fig. 14). A boundary, where an increase in reflectivity occurs, is located at approximately 1 km depth in S.P. 2 and at about 0.5 km in S.P. 1. The antiform structure could be associated with the folded amphibolite rocks present in the northwestern part of S.P. 2. However, these rocks do not appear farther north (on S.P. 1, see Fig. 2) where the antiform is located at a shallower depth in the seismic section. The antiform also appears to be much more gently folded than the folded rocks on the geological map (Fig. 2), and the antiform is marked by strong reflectivity indicating a large impedance contrast (seismic velocity and/or density contrast). Therefore, we interpret this antiform structure as a boundary to a different unit. This unit reflects a significant property change within the gneissic basement rock. One such boundary that could cause a large impedance contrast is the detachment zone separating the lower eclogitic crust from the middle and upper crust exposed in Western Norway (Andersen and Jamtveit, 1990). The fold hinge line of this unit appears to have a strike subparallel to the strike of the Tjellefonna fault (Fig. 14). Unfortunately, it is difficult to determine if the fault structures cut the fold structure or not. Reflection R1/S1 seems to terminate approximately where a continuation of the

southeastern flank of the antiform in S.P. 2 is expected. However, there is no obvious reason to why such a fold flank should not be imaged properly in the seismic section (Fig. 4a). The northwest dipping reflectivity marked by the arrow in shot 95 (Fig. 6b), and seen in the stacked section between CMP 1750 and 1800 at about 0.5 s TWT (Fig. 4a), seems to be the only indication of a continuation of the reflective package towards the southeast. Also on S.P. 1, the fold structure is not imaged southeast of the suggested fault zone (Figs. 3 and 14). Therefore, it seems likely that the fault does cut the antiform structure, although the fault zone is not detected deeper in the seismic section. The depth extent to where reflections R1–R5 can be traced on the stacked section is mainly controlled by the length of the seismic acquisition line and a deeper extension cannot be imaged without extending the seismic profile further southeast. The parallelism of the fold hinge line and the fault trace of the Tjellefonna fault (Fig. 14) suggest that the folding and faulting may have been related. The low topography lineament does not coincide with the Tjellefonna fault in the northeastern side of the Tingvollfjord (Figs. 2 and 14), perhaps indicating that the Tjellefonna fault is less pronounced towards the northeast.

5.7 **Conclusions**

The Tjellefonna Fault was imaged using two reflection seismic profiles located on each side of the Tingvollfjord. The fault extends to a depth of at least 400 m and most likely to at least 1.3 km on the southern side of the fjord where it was imaged most clearly. The fault dips 50–60° towards southeast at depth.

A continuation of the fault on the northeastern side is suggested by correlation of an in-strike P-S converted reflection (generated by a fracture zone) seen on the reflection data on the northeastern side of the Tingvollfjord on S.P. 1. The fault zone is, however, not seen on the stacked section on this profile, perhaps due to the fault zone being steeper on the northeastern side or because the seismic profile was too short to image the deeper part of the fault zone.

The fault seems to diverge into at least two zones of intensely fractured bedrock near the surface on the southern side of the Tingvollfjord (S.P. 2 and R.P. 7). The seismic data correlate well with resistivity and other near surface geophysical data

presented by Nasuti et al. (2011) and in this paper. Also, the strike of the fault is in agreement with previous large scale interpretation of potential field data by Nasuti et al. (2012). However, the main topographic lineament is only in agreement on the south-western side of the Tingvollfjord, perhaps indicating that the Tjellefonna fault is less pronounced towards the northeast.

An antiform can be seen on both seismic sections (S.P. 1 and S.P. 2). Increased amplitudes of reflections from this structure are found at a depth of about 0.5 km on the northeastern profile (S.P. 1) and at about 1 km on the southwestern profile (S.P. 2). The fold hinge line of the antiform is parallel to the suggested Tjellefonna fault, indicating that the folding and faulting may have a causal relationship. The amplitude increase suggests a significant physical property change within the gneissic basement rock. If the antiform structure is penetrated or truncated by the fault or not is, however, not clear.

Acknowledgements.

References

Andersen, T. B. and Jamtveit, B.: Uplift of deep crust during orogenic extensional collapse: a model based on field studies in the Sogn-Sunnfjord region, W. Norway, *Tectonics*, 9, 1097–1111, 1990.

Austrheim, H., Corfu, F., Bryhni, I., and Andersen, T. B.: The Proterozoic Hustad igneous complex: a low strain enclave with a key to the history of the Western Gneiss Region of Norway, *Precambrian Res.*, 120, 149–175, 2003.

Biedermann, A. R.: Magnetic Properties of the Møre-Trøndelag Fault Complex, Msc thesis, ETH Zurich, http://e-collection. library.ethz.ch/view/eth:1986, 2010.

Braathen, A., Nordgulen, Ø., Osmundsen, P. T., Andersen, T. B., Solli, A., and Roberts, D.: Devonian, orogen-parallel, opposed extension in the Central Norwegian Caledonides, *Geology*, 28, 615–618, 2000.

Brekke, H.: The tectonic evolution of the Norwegian Sea continental margin, with emphasis on the Vøring and Møre basins, in: Dynamics of the Norwegian Margin, edited by: Nøttvedt, A., *Geol. Soc. Lond. Spec. Publ.*, 167, 327–378, 2000.

Cosma, C. and Enescu, N.: Characterization of fractured rock in the vicinity of tunnels by the swept impact seismic technique, Int. J. Rock Mech. Min., 38, 815–821, 2001.

Dahlin, T.: 2D resistivity surveying for environmental and engineering applications, *First Break*, 14, 275–284, 1996.

Dehghannejad, M., Juhlin, C., Malehmir, A., Skytta, P., and Weihed, P.: Reflection seismic imaging of the upper crust in the Kristineberg mining area, northern Sweden, *J. Appl. Geophys.*, 71, 125–136, 2010.

Faleide, J. I., Kyrkjebø, R., Kjennerud, T., Gabrielsen, R. H., Jordt, H., Fanavoll, S., and Bjerke, M. D.: Tectonic impact on sedimentary processes during Cenozoic evolution of the northern North Sea and surrounding areas, *Geol. Soc. Lond. Spec. Publ.*, 196, 235–269, 2002.

Gabrielsen, R. H., Odinsen, T., and Grunnaleite, I.: Structuring of the Northern Viking Graben and the Møre Basin; the influence of basement structural grain, and the particular role of the Møre-Trøndelag Fault Complex, *Mar. Petrol. Geol.*, 16, 443–465, 1999.

Ganerød, G. V., Grøneng, G., Rønning, J. S., Dalsegg, E., Elvebakk, H., Tønnesen, J. F., Kveldsvik, V., Eiken, T., Blikra, L. H., and Braathen, A.: Geological model of the Åknes rockslide, western Norway, *Eng. Geol.*, 102, 1–18, 2008.

Green, A. G. and Mair, J. A.: Subhorizontal fractures in a granitic pluton: Their detection and implications for radioactive waste disposal, *Geophysics*, 48, 1428–1449, 1983.

Grønlie, A. and Roberts, D.: Resurgent strike-slip duplex development along the Hitra-Snåsa and Verran Faults, Møre-Trøndelag Fault Zone, Central Norway, *J. Struct. Geol.,* 11, 295–305, 1989.

Grunnaleite, I. and Gabrielsen, R. H.: Structure of the Møre Basin, mid-Norway continental margin, *Tectonophysics*, 252, 22I–251, 1995.

Hacker, B. R., Andersen, T. B., Johnston, S., Kylander-Clark, A. R. C., Peterman, E. M., Walsh, E. O., and Young, D.: High-temperature deformation during continental-margin subduction & exhumation: The ultrahigh-pressure Western Gneiss Region of Norway, *Tectonophysics*, 480, 149–171, 2010.

Hurich, C. A.: Kinematic evolution of the lower plate during intracontinental subduction: An example from the Scandinavian Caledonides, *Tectonics*, 15, 1248–1263, 1996.

Hurich, C. A. and Roberts, D.: A seismic reflection profile from Stjørdalen to Outer Fosen, Central Norway: a note on the principal results, *Norg. Geol. Unders.* B., 433, 18–19, 1997.

Juhlin, C.: Interpretation of the reflections in the Siljan Ring area based on results from the Gravberg-I borehole, *Tectonophysics*, 173, 345–360, 1990.

Juhlin, C.: Imaging of fracture zones in the Finnsjön area, central Sweden, using the seismic reflection method, *Geophysics*, 60, 66–75, 1995.

Juhlin, C. and Stephens, M. B.: Gently dipping fracture zones in Paleoproterozoic metagranite, Sweden: Evidence from reflection seismic and cored borehole data and implications for the disposal of nuclear waste, *J. Geophys. Res.*, 111, B09302, doi:10.1029/2005JB003887, 2006.

Juhlin, C., Dehghannejad, M., Lund, B., Malehmir, A., and Pratt, G.: Reflection seismic imaging of the end-glacial P¨arvie Fault system, northern Sweden, *J. Appl. Geophys.*, 70, 307–316, 2010.

Juhlin, C. and Lund, B.: Reflection seismic studies over the end-glacial Burtr¨ask fault, Skellefteå, Sweden, *Solid Earth*, 2, 9–16, doi:10.5194/se-2-9-2011, 2011.

Loke, M. H.: Tutorial: 2-D and 3-D electrical imaging surveys, 136 pp., 2004.

Lundberg, E. and Juhlin, C.: High resolution reflection seismic imaging of the Ullared Deformation Zone, southern Sweden, *Precambrian Res.*, 190, 25–34, 2011.

Moos, D. and Zoback, M. D.: In Situ Studies of Velocity in Fractured Crystalline Rocks, *J. Geophys. Res.*, 88, 2345–2358, 1983.

Mosar, J., Eide, E. A., Osmundsen, P. T., Sommaruga, A., and Torsvik, T. H.: Greenland – Norway separation: A geodynamic model for the North Atlantic, *Norw. J. Geol.,* 82, 281–298, 2002.

Mykkeltveit, S.: A Seismic Profile in Southern Norway, *Pure Appl. Geophys.*, 118, 1310–1325, 1980.

Nasuti, A., Chawshin, K., Dalsegg, E., Tønnesen, J. F., Ebbing, J., and Gellein, J.: Electrical resistivity and refraction seismics over a segment of the Møre-Trøndelag Fault Complex, NGU report 2009.037, 37 pp., 2009.

Nasuti, A., Pascal, C., Ebbing, J., and Tønnesen, J. F.: Geophysical characterisation of two segments of the Møre-Trøndelag Fault Complex, Mid Norway, *Solid Earth*, 2, 125–134, doi:10.5194/se-2-125-2011, 2011.

Nasuti, A., Pascal, C., and Ebbing, J.: Onshore-offshore potential field analysis of the Møre-Trøndelag Fault Complex and adjacent structures of Mid Norway, *Tectonophysics*, 518–521, 17–28, 2012.

Olesen, O., Blikra, L. H., Braathen, A., Dehls, J. F., Olsen, L., Rise, L., Roberts, D., Riis, F., Faleide, J. I., and Anda, E.: Neotectonic deformation in Norway and its implications: a review, *Norw. J. Geol.*, 84, 3–34, 2004.

Osmundsen, P. T., Eide, E. A., Haabesland, N. E., Roberts, D., Andersen, T. B., Kendrick, M., Bingen, B., Braathen, A., and Redfield, T. F.: Kinematics of the Høybakken detachment zone and the Møre-Trøndelag Fault Complex, central Norway, *J. Geol. Soc. London*, 163, 303–318, 2006.

Pascal, C. and Gabrielsen, R. H.: Numerical modeling of Cenozoic stress patterns in the mid-Norwegian margin and the northern North Sea, *Tectonics*, 20, 585–599, 2001.

Redfield, T. F. and Osmundsen, P. T.: The Tjellefonna Fault system of Western Norway: Linking late-Caledonian extension, post-Caledonian normal faulting, and Tertiary rock column uplift with the landslide-generated tsunami event of 1756, *Tectonophysics*, 474, 106–123, 2009.

Redfield, T. F., Braahten, A., Gabrielsen, R. H., Osmundsen, P. T., Torsvik, T. H., and Andriessen, P. A. M.: Late Mesozoic to Early Cenozoic components of vertical separation across the Møre-Trøndelag Fault Complex, Norway, *Tectonophysics*, 395, 233– 249, 2005a.

Redfield, T. F., Osmundsen, P. T., and Hendriks, W. H.: The role of fault reactivation and growth in the uplift of western Fennoscandia, *J. Geol. Soc. London*, 162, 1013–1030, 2005b.

Roberts, D.: High-strain zones from meso-to macro-scale at different structural levels, Central Norwegian Caledonides, *J. Struct. Geol.*, 20, 111–119, 1998.

Sherlock, S. C., Watts, L. M., Holdsworth, R. E., and Roberts, D.: Dating fault reactivation by Ar/Ar laserprobe; an alternative view of apparently cogenetic mylonite-pseudotachylite assemblages, J. Geol. Soc. London, 161, 335–338, 2004.

Séranne, M., 1992. Late Paleozoic kinematics of the Møre-Trøndelag Fault Zone and adjacent areas, central Norway. *Norsk Geologisk Tidsskrift* 72, 141-158.

Skår, Ø. and Pedersen, R. B.: Relations between granitoid magmatism and migmatization: U-Pb geochronological evidence from the Western Gneiss Complex, Norway, *J. Geol. Soc. London*, 160, 935–946, 2003.

Sommaruga, A. and Bøe, R.: Geometry and subcrop maps of shallow Jurassic basins along the Mid-Norway coast, *Mar. Petrol. Geol.*, 19, 1029–1042, 2002.

Terry, M. P. and Robinson, P.: Evolution of amphibolite-facies structural features and boundary conditions for deformation during exhumation of high-and ultrahigh-pressure rocks, Nordøyane, Western Gneiss Region, Norway, *Tectonics,* 22, 1036, doi:10.1029/2001TC001349, 2003.

Tveten, E., Lutro, O., and Thorsnes, T.: Berggrunnskart Alesund, 1:250 000, (Alesund, western Norway), Geological Survey of Norway, Trondheim (bedrock map), 1998.

Wain, A.: New evidence for coesite in eclogite and gneisses: Defining an ultrahigh-pressure province in the Western Gneiss region of Norway, *Geology*, 25, 927–930, 1997.

Chapter 6. Paper IV. 3D mechanical modeling of nucleation and propagation of brittle faulting; case study from the Møre-Trøndelag Fault Complex, Norway

Aziz Nasuti[1, 2], Christophe Pascal[3]

[1] Department of Petroleum Engineering and Applied Geophysics, Norwegian University of Science and Technology, 7491 Trondheim, Norway
[2] NGU, Geological Survey of Norway, 7491 Trondheim, Norway
[3] Institute of Geology, Mineralogy & Geophysics, Ruhr University Bochum, Germany

ARTICLE INFO	ABSTRACT
Article history: In preparation *Keywords:* Numerical Model Møre-Trøndelag Fault Complex Flac[3D] Stress Strain	The Møre-Trøndelag Fault Complex (MTFC) is one of the most prominent fault zones in Norway, onshore and offshore. The MTFC strikes ENE-WSW, paralleling the coastline of south central Norway, and separates the northern North Sea Basin from the deep Mesozoic Møre and Vøring basins. Onshore, features perpendicular to the main segments of the MTFC, outlined by pronounced topographic lineaments were probably created by mechanical linkage of these segments. The aim of this numerical modeling study is to investigate the mechanical consistency of this hypothesis. The commercial numerical modeling software FLAC[3D] was used. FLAC[3D] stands for Fast Lagrangian Analysis of Continua in 3D and is a commercial finite difference code for continuum mechanics computations. Two segments of the MTFC, the Verran and Hitra-Snåsa faults are considered. The two faults are parallel but dip in opposite directions. We systematically varied their respective dips. Three possible configurations for separation of the faults were assumed. The 3D models can give a deeper understanding of the evolution of the MTFC and, in particular, of the development of their postulated relay zones.

6.1 **Introduction**

The Møre-Trøndelag Fault Complex (MTFC) is one of the major fault zones in Mid Norway that spread from the mainland on to the shelf (Oftedahl 1975; Gabrielsen and Ramberg 1979; Bukovics et al. 1984). Considering the surrounding damage zones, the MTFC exhibits polyphased deformation including sinistral ductile shear in Devonian times, and normal faulting post-dating the middle Jurassic (Grønlie & Roberts 1989; Grønlie et al. 1991, 1994; Gabrielsen et al. 1999; Redfield et al. 2004, 2005). The MTFC consists of several major segments which have been mapped by Landsat and aerial images, surface geology and geophysics (Gabrielsen & Ramberg 1979; Gabrielsen et al. 2002, Redfield et al. 2004, 2005, Nasuti et al. 2011, 2012). On the Fosen Peninsula (Fig. 1), the MTFC consists of two marked strands, the Hitra-Snåsa (HSF) and Verran Faults (VF), with a surrounding network of accommodation fault zones, which are all well displayed on satellite images (e.g. Grønlie et al. 1991). The ENE-WSW to NE-SW grain of the MTFC basically affects a crustal section from Trondheim in the south to Vikna and Leka in the north (Rindstad & Grønlie 1987; Titus et al. 2002; Redfield et al. 2004, 2005, Nasuti et al. 2012). Based on the previous studies, the main lineament trends in the northeastearn part of the MTFC are ENE-WSW, NW-SE and there are subordinate E-W and N-S populations (Rindstad & Grønlie 1987, Gabrielsen et al. 2002) (Fig. 1). The N-S trend is also explained as faults in the near-shore Jurassic basins, apparently interacting with NE-SW master structures, whereas NW-SE faults considered as transfer structures within the basin realm (e.g. Sommeruga & Bøe 2002).

In order to explain the observed lineament pattern a sinistral displacement along the master faults of the MTFC has been proposed by previous authors based on geological mapping and structural interpretation (e.g. Titus et al., 2002). In this study, we used a numerical approach to explore the possibility that the lineaments perpendicular to the main strands of the MTFC are indeed brittle structures. We examine the effect of the geometry of the two major faults of the MTFC, the HSF and VF, in producing secondary faults along and between these faults. The commercial software, FLAC^{3D} (Itasca 2009), was used to model different fault configurations.
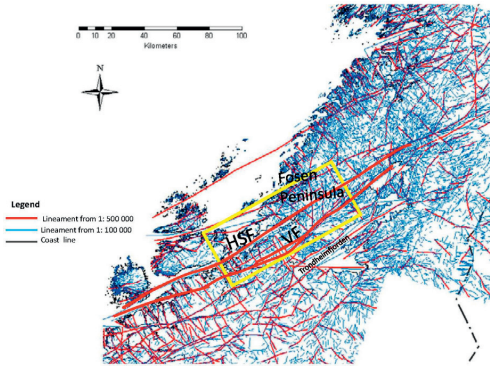
Fig.1 Lineament map of the Møre-Trøndelag region. Major lineaments are shown as red lines, whereas smaller lineaments are displayed in blue (Redrawn and modified from Olsen et al. 2007). The study area is assigned, by yellow box. HSF, Hitra-Snåsa Fault; VF, Verran Fault.

6.2 **Methodology**

6.2.1 **FLAC^{3D} and fault modeling**

In FLAC^{3D} (Itasca 2009), the medium is divided into distinct blocks. Blocks interact at their contacts, where constitutive laws are defined (Fig. 2). Numerical models are defined in terms of: (1) model structure; (2) material properties assigned and (3) boundary conditions. The mechanical behavior of faults can be simulated in FLAC^{3D} using special mechanical interfaces involving a combination of mechanical interfaces and solid elements (Fig. 2). Interfaces involve friction, cohesion, dilation, normal and shear stiffness, tensile and, shear bond strength (Fig. 2). The purpose of our numerical modeling is to calculate stress and strain along and between the faults in order to isolate zones in the model where new faults, fractures or damage zones could eventually nucleate.
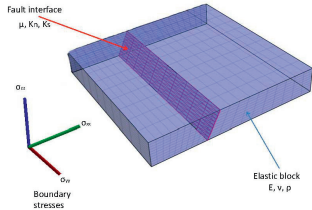
Fig.2 Fault modeling in FLAC^{3D}. Principle of the FLAC^{3D}. Active faults split elastic blocks apart (red mesh). Blocks deform internally and are free to move along the faults when boundary stresses are applied.

6.2.2   Fault damage zone and model geometry

There have been a series of detailed descriptions of fault linking zones and their related damage zones (e.g. Faulds & Varga 1998, Martel and Boger, 1998, Peacock 2002, Kim et al., 2000, 2001, 2003). For example, Kim et al. (2004) present a thorough description of damage zones particularly around strike-slip faults. They have systematically classified the damaged zones around the fault zones. Following their terminology, fault damage zones are divided in three main types: 1) wall, 2) linking, and 3) tip damage zones (Fig. 3). Also we have considered three types of fault segment configuration, zero-stepping, under-stepping and over-stepping segments (Fig. 3). The linkage damage zone is known as relay zone or, eventually, relay ramp (e.g. Peacock and Sanderson, 1994, Faulds & Varga, 1998). A relay zone is defined as an intervening zone between adjacent echelon normal fault segments that are over-stepping or understepping. Based on the dips of fault segments, the step length, and the shape of the faults the geometry of relay zones are different (Peacock and Sanderson, 1991, 1994). In this paper, our initial 3D numerical models focused on the interactions between planar faults which are embedded in a linear elastic medium. We have constructed several FLAC^{3D} models that represent these three types of configurations. The fault zone architecture is generally complex, depending on the history of faulting (temperature, pressure, stress conditions, strain rate) (Heermance et al., 2003) and lithology (Mandl, 2000, Berg & Skar, 2005); however, here we have focused on the dipping and stepping factors of the studied faults.
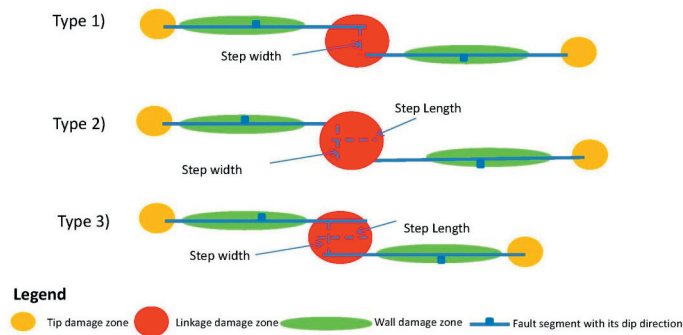
Fig. 3 Segment configurations, three types of fault models, Type 1 non-stepping, type 2 understepping and type 3 overstepping segments. Different damage zones with respect to their locations are shown in different shape and colors.

6.2.3   Model parameters

Dimension of the models are: a block of crust 100 km wide, 200 km long and 16 km thick, (Fig. 4). The dimensions, orientation and geometry of the model represent the simplified geology of the Fosen Peninsula (Fig. 1)

Two ENE-WSW (X-direction in the models) "Verran" and "Hitra-Snåsa" faults are simulated by interfaces with similar properties (Table 1). Their natural counterparts were both normal faults during their latest reactivation phase but with opposite dip directions (Fig. 4). The HSF dips NW while the VF dips SE (e.g. Bøe and Bjerkli 1989, Grønlie et al. 1991, Watts 2001). In each of the constructed models only parts of the HSF and VF faults are assumed to move. The scale (i.e. 200 km) of the models was designed in order to mimic the real scale of the MTFC. In order to simulate the stress state, we have attributed contrasting values for the maximum principal stresses (i.e. $\sigma_1 \neq \sigma_2 \neq \sigma_3$, Table 1).

Different dip values were used for both the HSF and the VF, ranging from moderate (i.e. $50°$) to steep (i.e. $80°$). Considering three types ofcoupling for the two faults (Fig. 3), 30 combinations were built in total. Because we have assumed the same properties for the blocks (hangingwall and footwall) and also for interfaces we avoid repeating some combinations for example a segment coupling with HSF $60°$ and VF $50°$ will be the same as HSF $50°$ and VF $60°$.

Table 1Parameters used in the modeling

Blocks rheology	
Young modulus	E – 80 GPa
Poisson's ratio	v = 0.25
Density	ρ – 2700 kg/m^3
Fault properties	
Friction in angel	10
Cohesion	C_0=0
Normal and shear stiffness	k_n =200, k_s = 100 GPa/m
Dilation in angel	0
Tension	5MPa
Boundary stresses	
Differential stress	(σ_{zz}= 20 MPa, σ_{xx} = 10 MPa, σ_{yy}=5 MPa)
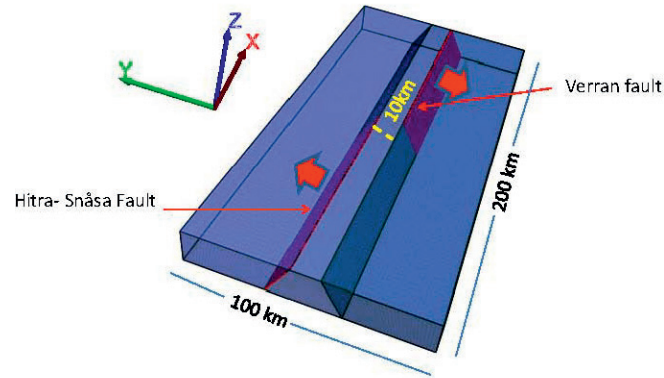
Fig. 4. Model geometry.

6.3 **Analysis of the results**

As mentioned before, we have constructed three types of fault configuration with respect to their step length (Fig. 3). Considering the boundary conditions and applying σ_{xx}, σ_{yy}, σ_{zz} (Table 1) the stress and strain distributions are calculated. With the FLAC^{3D} we are able to calculate all the components of stress and strain, however, only the maximum principal stress and strain are discussed here. Maximum principal stress theory, credited to W. J. M. Rankine (1820–1872), is useful for brittle materials; according to the theory that failure will occur when the maximum principal stress in a system reaches the value of the maximum strength at elastic limit in simple tension/compression systems. It has to be noted that in FLAC^{3D}, positive stresses indicate tension and negative stresses compression (Itasca 2009). Figure 5-7 show the results of maximum principal stress together with maximum principal strain increments.

6.3.1 **Zero-stepping faults**

Figure 5 shows the stress and strain patterns for the model "type 1" which we called zero-stepping (non-overlapping) segments. In this configuration there will be no step in length (in X direction) but a 12 km distance between two faults in width (in Y direction) (see Fig. 3).

The stress accumulation is clear along the strike of the faults. There is a 1-2 MPa stress difference between the fault adjacent areas and the areas that are further away

from the fault planes (Fig. 5). There are some similarities and also differences among the stress patterns of the paired segments with different dips. The maximum absolute value of the stress is seen for the faults dipping 60° and the lowest value for 80°. The relay zone (linkage damage zone) shows a stress concentration for all fault configurations with least concentration for pairs of faults with 50° -50°. However, the faults dipping 50° show more stress concentrations in their tips (see Fig.5).

For zero-stepping faults, the strain increment is dip-dependent and maxima occur along the strike of the faults. Similar to stress patterns, the strain for the faults dipping 50° show obvious increments at their tips, while this is not visible in models with other dip values (Fig. 5). The faults dipping 60° show a strain increment subparallel to the areas that are the most deformed. These increments are not seen with other modeled dip values. The relay zone in zero-stepping faults does not show a significant strain contrast with respect to the rest of the model, except at the vicinity of the fault tips (Fig.5).
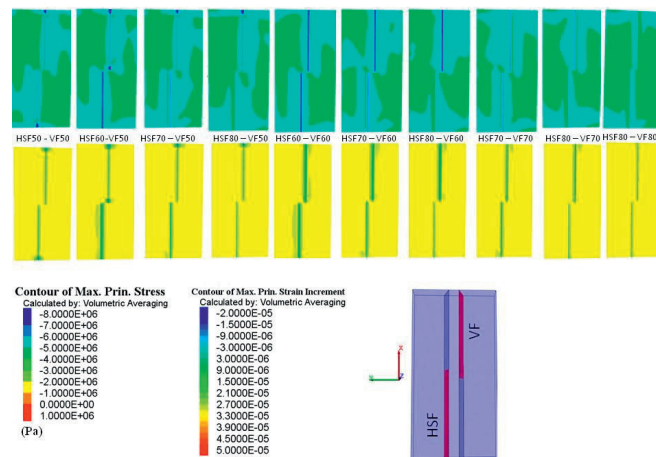
Fig. 5, View of the stress (top) and strain (bottom) distribution for models of type 1 with different fault dips (check Fig. 3). HSF, Hitra-snåsa Fault; VF, Verran Fault. The small numbers beside HSF and VF faults show their dips in degree.

6.3.2 Under-stepping faults

Figure 6 shows the stress and strain patterns for the model "type 2" which we called under-stepping segments. In this configuration there is a step of 10 km in X

direction and a separation distance of 12 km between the two faults in Y direction (see Fig. 3).

The stress pattern of under-stepping faults is very similar to those of zero-stepping faults except for the relay zones (Figs. 5 & 6). In contrast to the zero-stepping faults cases, the relay zone does not show stress concentrations for under-stepping faults.

The strain evolution of the under-stepping faults is also similar to the strains of zero-stepping faults. However, there is no strain path in the relay zone of the faults that can connect them.
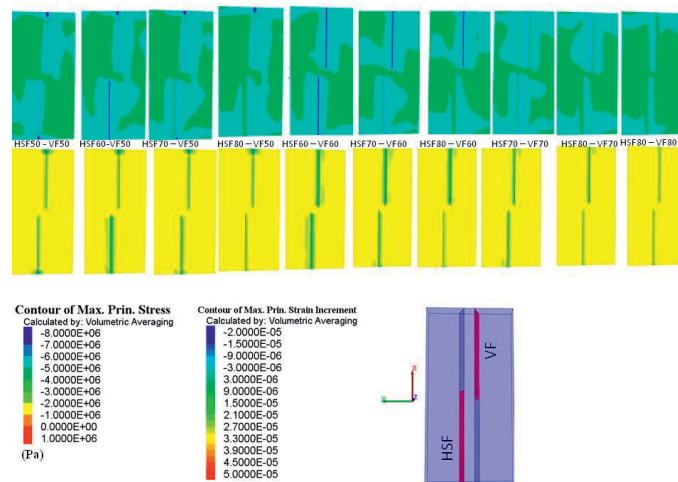
Fig. 6 View of the stress (top) and strain (bottom) distribution for models of type 2 with different fault dips (check Fig. 3). HSF, Hitra-snåsa Fault; VF, Verran Fault. The small numbers beside HSF and VF faults show their dips in degree.

6.3.3 Over-stepping faults

Figure 7 shows the stress and strain patterns for the model "type 3" called over-stepping segments. In this configuration there is step with 10 km length (in X direction) the fault (overlapping) and a 12 km distance between two faults in width (in Y direction) (see Fig. 3).

The results of strain and stress patterns for over-stepping faults indicate a stress concentration in the relay zone and also a strain path that connects the two faults. The outside stress and strain patterns are similar to the zero and under-stepping faults cases.
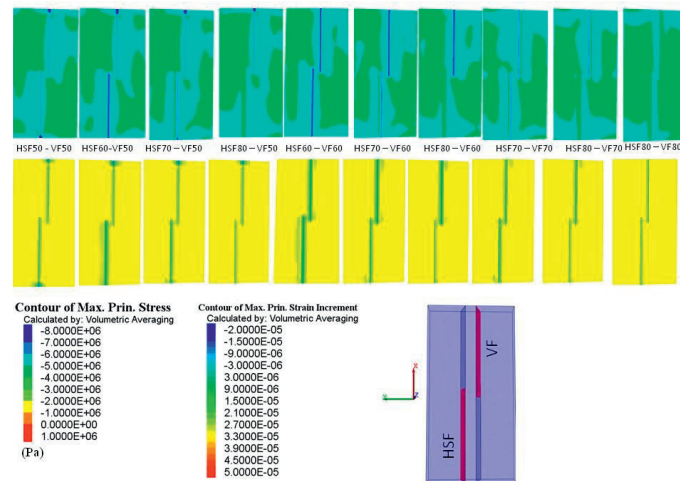
Fig. 7 View of the stress (top) and strain (bottom) distribution for models of type 3 with different fault dips (check Fig. 3). (check Fig. 3). HSF, Hitra-snåsa Fault; VF, Verran Fault. The small numbers beside HSF and VF faults show their dips in degree.

6.4 Discussion

The results presented in this paper are three dimensional numerical models that we have developed to investigate the role of mechanical interaction between regional-scale fault segments. It should be noted that the results discussed below are for an isotropic lithology. Horizontal layering is an important factor in the evolution of strain at different structural levels (e.g., Soliva & Benedicto, 2005; Rykkelid & Fossen, 2002), however, its effect can be neglected in the present case because layering (i.e. metamorphic foliation) appears to be subvertical (e.g. Watts 2001). Our analyses include models with varying (1) step length between the segments and (2) fault surface dips (50° to 80°). Model results suggest that, in general, strain maxima occur along the strike of the faults. Deformation and stress accumulation are a function of the dip of the fault. There are many similarities but also differences between the stress and strain patterns modelled for the three types of fault configurations. The results suggest that in all of these three types the faults dipping 50° show the highest stress and strain concentrations at their tips. Maximum stress concentrations are seen for the faults dipping 60°. As previously mentioned there are strain concentrations for faults dipping 60°, sub-parallel to the main faults which suggest nucleation of secondary fractures. The

3D models show a clear difference in the relay zones for the three types of configurations. The results show that stress is developed in relay zones for the zero and over-stepping faults but do not develop for the under-stepping faults. Continuous strain paterns between the faults can only be observed for the over-stepping faults. Figure 8 shows a depth transect of the stress and strain models for the three fault types. This figure indicates that even for the over-stepping faults strain and stress distribute at relatively shallow depths, suggesting that secondary fractures are rooted at shallow depths as well.
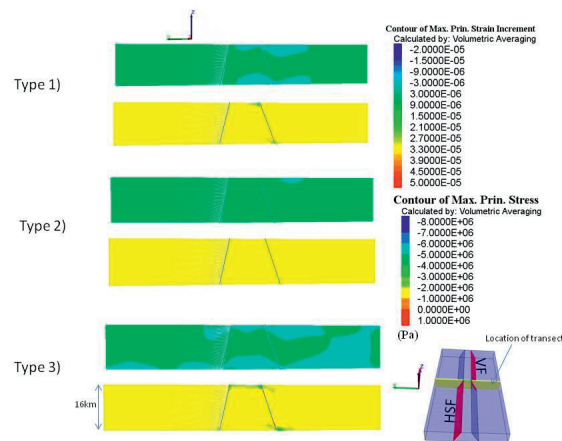
Fig. 8 A transect of the model, maximum principal stress and maximum principal strain increment of the model for VF 70 and HSF 80. HSF, Hitra-snåsa Fault; VF, Verran Fault.

6.5 **Conclusion and implication for the MTFC**

The geometric elements of our three dimensional numerical models correspond to the generalized surface geometries of the Hitra-Snåsa Fault (HSF) and Verran Fault (VF) as two major strands of MTFC fault zone. This study depicts the role of mechanical interaction between the HSF and the VF on the evolution of the stress and strain fields in these segments. It is shown that if the faults dip oppositely with having overlapping areas new faults/fracture zones may develop. These fractures are expected to have relatively shallow depth extend. In general, the nucleation of the new faults/fractures is dependent on the dips of the existing faults but also on the overlap between the major faults. It is also shown for the normal faults that are dipping 60° there will be areas sub-parallel to the main faults, with a high potential to develop secondary

fractures. Such structures and lineament can be recognized in the lineament pattern of the study area (Fig. 1). In summary the model results are able to account for the observed lineaments both perpendicular and parallel to the MTFC.

References

Berg, S. S. & Skar, T. 2005. Controls on damage zone asymmetry of a normal fault zone: outcrop analyses of a segment of the Moab fault, SE Utah. *Journal of Structural Geology*, 27, 1803–1822.

Bøe, R., & Bjerkli, K. 1989. Mesozoic sedimentary rocks in Edøyfjorden and Beitstadfjorden, Central Norway: Implications for the structural history of the Møre–Trøndelag fault zone. *Marine Geology*, 87, 287–299.

Bukovics, C., Cartier, E.G., Shaw, P.A. & Ziegler, P.A. 1984. Structure and development of the Mid-Norway continental margin. In: Society, N.P. (ed.) Petroleum Geology of the North European Margin. Graham & Trotman, London, 407–423

Faulds, J.E., Varga, R.J., 1998. The role of accommodation zones and transfer zones in the regional segmentation of extended terranes. In: Faulds, J.E., Stewart, J.H. (Eds.), accommodation Zones and Transfer Zones: The Regional Segmentation of the Basin and Range Province. Geological Society of America Special Publication, vol. 323, pp. 1 – 45.

Gabrielsen, R.H., Odinsen, T. and Grunnaleite, I., 1999. Structuring of the Northern Viking Graben and the Møre Basin; the influence of basement structural grain, and the particular role of the Møre-Trøndelag Fault Complex. Marine and Petroleum Geology, 16: 443-465.

Gabrielsen, R.H. and Ramberg I.B., 1979. Fracture patterns in Norway from LANDSAT imagery: results and potential use. In: Proceedings of the Norwegian Sea Symposium, NSS/20, Tromsø. Norwegian Petroleum Society (NPF), pp. 1-10.

Gabrielsen, R.H., Braathen, A., Dehls, J. & Roberts, D. 2002: Tectonic lineaments of Norway. Norwegian Journal of Geology 82, 153-174.

Grønlie, A. and Roberts, D., 1989. Resurgent strike-slip duplex development along the Hitra-Snåsa and Verran Faults, More- Trøndelag Fault Zone, Central Norway. Journal of Structural Geology, 11 (3): 295-305

Grønlie, A., Nilsen, B. & Roberts, D. 1991: Brittle deformation history of fault rocks on the Fosen Peninsula, Trøndelag, Central Norway. Norges geologiske undersøkelse Bulletin 421, 39-57

Grønlie, A., Naeser, C.W., Naeser, N.D., Mitchell, J.G., Sturt, B.A. & Ineson, P. 1994. Fission track and K/Ar dating of tectonic activity in a transect across the Møre–Trøndelag Fault Zone, Central Norway. Norwegian Journal of Geology, 74, 24–34.

Heermance, R., Shipton, Z.K., Evans, J.P., 2003. Fault structure control on fault slip and ground motion during the 1999 rupture of the ChelungpuFault, Taiwan. Bulletin of the Seismological Society of America 93 (3),1034–1050.

Itasca, 2009. FLAC^{3D}, Fast Lagrangian Analysis of Continua in 3 Dimensions, Version 4.0. Minneapolis, Minnesota, Itasca Consulting Group, 438pp.

Kim, Y.-S., Andrews, J.R., Sanderson, D.J., 2000. Damage zones around strike–slip fault systems and strike–slip fault evolution, Crackington Haven, southwest England. Geoscience Journal 4, 53–72.

Kim, Y.-S., Andrews, J.R., Sanderson, D.J., 2001. Secondary faults and segment linkage in strike–slip fault systems at Rame Head,southern Cornwall. Geoscience in South-West England 10,123–133.

Kim, Y.-S., Peacock, D.C.P., Sanderson, D.J., 2003. Mesoscale strike–slip faults and damage zones at Marsalforn, Gozo Island, Malta. Journal of Structural Geology 25, 793– 812.

Kim, Y.-S., Peacock, D.C.P., Sanderson, D.J., 2004. Fault damage zones. Journal of Structural Geology 26, 503–517.

Mandl, G., 2000. Faulting in Brittle Rocks. An Introduction to the Mechanics of Tectonic Faults. Springer, Berlin.

Martel, S.J., Boger, W.A., 1998. Geometry and mechanics of secondary fracturing around small three-dimensional faults in granitic rock.*Journal of Geophysical Research* 103, 21299–21314.

Nasuti, A., Pascal, C., Ebbing, J. and Tønnesen, J. F, 2011.: Geophysical characterisation of two segments of the Møre-Trøndelag Fault Complex, Mid Norway, Solid Earth, 2, 125–134, 2011.

Nasuti, A., Pascal, C., Ebbing, J., 2012. Onshore–offshore potential field analysis of the Møre–Trøndelag Fault Complex and adjacent structures of Mid Norway, Tectonophysics, 518-521, 17-28.

Oftedahl. C. 1975. Middle Jurassic graben tectonics in Mid Norway. Proc. Jurassic Northern North Sea Symposium 21, 1-13.

Olsen,E., Gabrielsen,R.H., Braathen,A. & Redfield,T.F., 2007: Fault systems marginal to the Møre Trøndelag Fault Complex, Osen-Vikna area, Central Norway. *Norwegian Journal of Geology*, 87, 59-73

Peacock, D.C.P., Sanderson, D.J., 1991. Displacements, segment linkage and relay ramps in normal fault zones. Journal of Structural Geology 13, 721–733.

Peacock, D.C.P., Sanderson, D.J., 1994. Geometry and development of relay ramps in normal fault systems. Bulletin of the American Association of Petroleum Geologists 78, 147– 165.

Peacock, D.C.P., 2002. Propagation, interaction and linkage in normal fault systems. Earth-Science Reviews 58, 121–142.

Redfield, T.F., Torsvik, T.H., Andriessen, P.A.M. & Gabrielsen, R.H. 2004. Mesozoic and Cenozoic tectonics of the Møre Trøndelag Fault Complex, central Norway: constraints from new apatite fission track data. *Physics and Chemistry of the Earth*, 10(29), 673–682.

Redfield, T.F., Osmundsen, P.T., Hendriks, B.W.H., 2005. The role of fault reactivation and growth in the uplift of western Fennoscandia. *Journal of the Geological Society, London,* 162, 1013–1030.

Rindstad, B. & Grønlie, A. 1987: Landsat TM data used in the mapping of large-scale geological structures in coastal areas of Trøndelag,central Norway. *Proceedings, Earthnet Pilot Project on Landsat Thematicm Mapper Applications,* Frascati, Italy 1987, 169-181.

Rykkelid, E., and Fossen, H., 2002, Layer rotation around vertical fault overlap zones: observations from seismic data, field examples, and physical experiments, Marine and Petroleum Geology**,** v. 19, pp. 181–192

Sommeruga, A. & Bøe, R. 2002: Geometry and subcrop maps of shallow Jurassic basins along the Mid-Norway coast. *Marine and Petroleum Geology 19*, 1029-1042.

Soliva, R., and Benedicto, A., 2005, Geometry, scaling relation and spacing of vertically restricted normal faults, Journal of Structural Geology, v. 27, pp. 317–325.

Titus, S.J, Fossen, H., Pedersen, R.B., Vigneresse, J.L. and Tikoff, B., 2002. Pull-apart formation and strike-slip partitioning in an obliquely divergent setting, Leka Ophiolite, Norway. *Tectonophysics*, 354: 101–1019.

Watts, L.M., 2001. The Walls Boundary fault zone and the Møre-Trøndelag Fault Complex: a case study of two reactivated fault zones. Unpublished PhD thesis, Department of Geological Sciences, University of Durham.

Chapter 7. Concluding remarks

The Møre-Trøndelag Fault Complex (MTFC) has been studied as a key structural element of the geology of Mid Norway. The fault complex extends from north of the Shetland Isles, UK, to northern Trøndelag, onshore Norway. Studying such a fault zone with several hundred kilometers length together with its long geological history gave the opportunity to explore the evolution of Mid Norway. This study integrated geology and geophysics in order to characterize the fault zones at both local and regional scales. Furthermore, three dimensional numerical modeling was used to understand secondary faults/fractures perpendicular to the main trend of the MTFC.

7.1 Regional study

For the regional study, potential field methods together with petrophysical data were used to map the segments of the MTFC. The analysis of regional gravity and magnetic data provides a valuable tool to investigate the large- to medium-scale tectonic structures of Mid Norway. These data are particularly interesting for studying the link of the MTFC and adjacent structures. The study revealed new fault candidates and attempted to depict the nature of the onshore-offshore link of the MTFC. In the absence of seismic data near-coastal areas of Mid Norway, potential field data have been used to fill this gap of information. Potential field data analysis helps to define the boundaries of deep-seated structures and geological complexes on the mainland (e.g. TIB) and also offshore (e.g. Frøya High). This study shows that the offshore–onshore link of the MTFC is obscured by gravity and magnetic signals related to adjacent structures, in particular to the Frøya High. Comparison of the results with petrophysical data explains the source of the potential field anomalies and assists in understanding of the spatial relationships between mineralised zones and geological structures.

7.2 Local study

For the local study, multiple geophysical data sets were used to build 2D and 3D geophysical and geological models for two segments of the MTFC. The Bæverdalen and Tjellefonna faults. Based on non-reflection seismic data, the Tjellefonna fault is

interpreted as a 100-200 m-wide zone of gouge and/or water-saturated, fractured bedrock dipping steeply to the south. This fault zone appears to be flanked by two additional but minor damage zones but only one of them can be determined with sufficient confidence. A secondary normal fault also dipping steeply to the south but involving indurated breccias has been detected ~1 km farther north. The Bæverdalen fault is interpreted as a ~700 m-wide and highly deformed zone involving fault gouge, densely fractured rocks and intact bedrock, embedded within the fault rock products, and as such it is probably the most important fault segment in the studied area and accommodated most of the strain during the inferred late Jurassic normal faulting. The geophysical data suggest that the Bæverdalen fault dips steeply towards the south, in agreement with the average orientation of the local tectonic grain. The Tjellefonna fault was also imaged using two reflection seismic profiles located on each side of Tingvollfjord. The fault extends to a depth of at least 400 m and most likely to at least 1.4 km on the southern side of the fjord where it was clearly imaged. The fault dips 50-60° towards southeast at depth. This dip is in agreement with the 2D model based on gravity and magnetic data. A continuation of the fault on the north-eastern side is suggested by correlation of an in-strike P-S converted reflection (generated by a fracture zone). The fault seems to diverge into at least two zones of intensely fractured bedrock near the surface on the southern side of the Tingvollfjord.

7.3 Three dimensional numerical modeling

3D numerical modeling was used to understand the evolution of strain and stress of two segments of MTFC, the Verran and Hitra-Snåsa faults. The study focused on the natural relay zones (linkage zone between the fault segments). The 3D models provide insights into possible trends of secondary faults and fractures within relay zones. This study depicts the possible faults/fractures perpendicular to the main faults in terms of overlap of the two segments. Furthermore, this study also shows that the resulting faults/fractures would have a relatively shallow depth.

7.4 Further recommendations

As mentioned in the thesis the large scale study of the MTFC is based on regional gravity and magnetic data, these data are rather too coarse in some areas

especially in coastal areas, therefore in order to have a better interpretation with more detail we need higher resolution data. Also acquisition of more seismic profiles and the use of deep geophysical methods, such as MT, are crucially needed for a better understanding of the geometry of the MTFC fault zone. For example, in order to resolve the depth extension of the fault and how it connects to the other fault zones in the near coast we need regional scale seismic profiles with sufficient resolution. The constructed 3D numerical models presented in this thesis are simplistic with respect to the geological complexity of the area and calibration of the results using data from field mapping is still lacking. As an improvement a more complex model should be constructed using additional constrains obtained in the field.

Appendix A

New gravity and magnetic data

In order to detect the changes associated with structural offsets or fault rocks along single fault segments of the MTFC, the distance between gravity stations crossing the fault segments must be decreased. Two gravimeters were used for the survey, the Scintrex CG-3 and the LaCoste & Romberg model G569 (Fig. A 1). The Autograv Scintrex CG-3 measures the gravity in mGal with a theoretical accuracy of 0.005 mGal. The LaCoste & Romberg model g-Gravimeter (Serial No. 569), has a theoretical precision of about 0.01 mGal. Corrections are made for instrument drift by comparing repeated readings at base stations, and theoretical Earth tide corrections are made to account for the distortion of the Earth caused by the gravitational pull of the Sun and the Moon as well as the other planets which occupy relatively much smaller component.
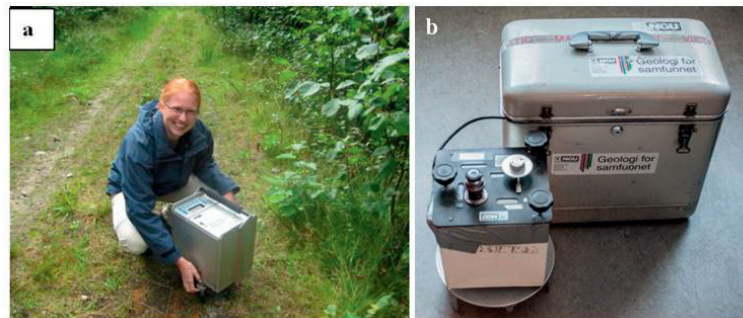
Fig. A 1 Gravimeters, (a) Scintrex CG-3, (b) LaCoste & Romberg Model G

Both gravimeters do not measure absolute gravity but measure changes in gravitational acceleration from station to station. During a gravity survey, one uses a base station network, for which the values of absolute gravity are known, and links the local measurements to this network. The primary base stations used for our survey, are located in Oppdal, Molde and Sunndalsøra (Fig. A 2). These stations are part of the Norwegian Gravity Reference Network and tied to the IGSN71. The closest reference station to the survey area was in Sunndalsøra. However, due to recent rebuilding the exact location of the gravity point could not be found. Therefore, we used both the stations in Oppdal and Molde to re-establish a gravity station in Sunndalsøra and linked

this point to our camp site in Trædal, near Sunndalsøra. Table A 1 summarizes the information about the absolute gravity points.

Readings at the base station in Trædal were taken every morning and evening on the days of measuring. A second field base station was established directly in the survey area (station Eidsøra in Fig. A 2). Readings were repeated several times during each day of measurements.
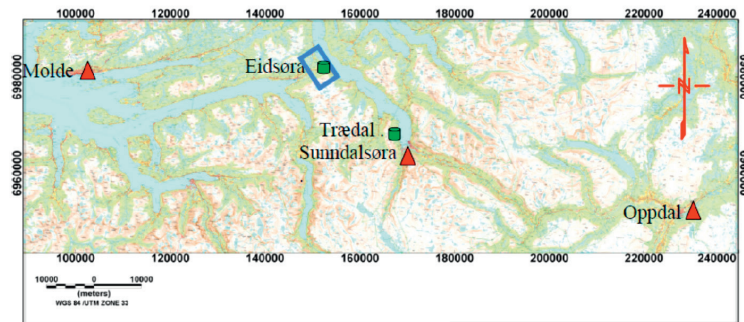
Fig. A 2 The IGSN71 base stations shown (red triangles) and the base station established for our gravity survey (green cylindre). The blue frame depicts the gravity survey area.

Table A 1 Gravity base stations used for data collected.

Base name	Latitude N	Longitude W	Elevation (m)	Absolute gravity (mGal)
Oppdal P	62° 35;72	9° 41;72	544,146	981950,242
Sunndalsøra	62° 40;46	8° 33;85	7,037	982034,004
Trædal	62° 39;65	8° 32;03	49,0	982028.114
Molde	62°44;30	7°09;61	5,6	982113,424

LEVELING

Detailed information on the vertical and horizontal position of the measurements is important for the data processing. Especially for gravity, the accuracy of the elevation estimates must be in the centimeter scale to resolve Bouguer anomalies in the order of 20 microGal (μGal). Horizontal accuracy is not as crucial as vertical accuracy in the gravity processing. GPS typically provides a horizontal accuracy (<10 m) that is acceptable for gravity surveys but for vertical positioning we used a total station survey camera with a precision of 1 mm (Fig. A 3).

Fig. A 3 Leveling instruments: (a) Total station survey camera for height measurements, (b) GPSMap 60Cx used for horizontal location of the gravity points.

Fig. A 4 shows the stations established in the study area. For the stations labeled L01 to L13 only GPS was used for estimation of the elevation and location. For all other stations the elevation was determined by total station leveling. Table A 2 lists the loop closing error during leveling. In order to correct the large errors (>10 cm), we remeasured some of the loops. Nevertheless, rough topography makes some areas inaccessible and prohibited us to measure loops for all data points. Table A2 shows the stations that loops began with and ended. Some of the staions were eliminated because of large uncertainity (e.g., F30-F35).
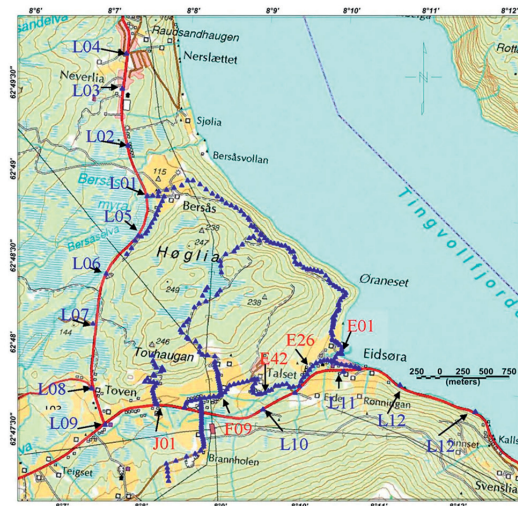
Fig. A 4 Locations of gravity points (dark blue triangles). Stations L01 to L12 are regional gravity stations with location/height measured with GPS only. Some stations which have been relocated and re-measured are shown with red labels.

Table A 2 Loop errors and measurements for quality control of leveling. Elevation 1 and 2 show remeasurements of the station elevation. See Fig. A 4 for station location.

Station name	Longitude	Latitude	Elevation 1 (m)	Elevation 2 (m)	Difference(m)
E01	8.10.05	62.48.05	2,270	2,229	0.05
E26	8.09.43	62.47.55	19,503	19,703	0.20
E42	8.08.50	62.47.49	43,343	43,328	0.02
F01	8.08.25	62.47.44	98,505	98,610	0.10
F09	8.08.38	62.47.43	101,173	101,131	0.04
F14	8.09.12	62.47.42	101,129	100,544	0.58
F32	8.09.48	62.47.53	79,783	79,211	0.57
F35	8.08.23	62.47.25	49,398	48,416	0.98
F133	8.08.04	62.47.44	130,667	130,620	0.05
J01	8.08.13	62.47.44	98,553	98,433	0.12

The gravity data were collected perpendicular to the fault zone with a distance between the stations from 20 to 80 meters. In the vicinity of the faults, we reduced station spacing. For data collection the so-called 'Jump-Step method' (Fig. A 5) was used and every station was measured at least twice. This procedure is used in microgravity surveys when high accuracy is required. The new gravity data that was measured in this project is shown in Table A 3.
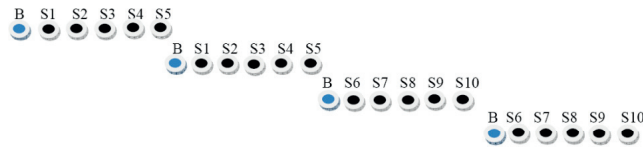
Fig. A 5 Jump-step method for gravity data acquisition. S1-S10 shows the gravity stations and B is showing the gravity base station.

Table A 3 Gravity data acquired in Eidsøra region (see Fig. A 4 for location). Station = Station name, Longitude, Latitude = geographical coordinates [WGS 84], Elevation = height above mean sea level [m], ABSG= Absolute gravity [mGal], TC= Terrain correction [mGal], FA= Free air anomaly [mGal], BA= Simple Bouguer anomaly [mGal], CBA= Complete Bouguer anomaly [mGal].

Station	Longitude	Latitude	Elevation	ABSG	TC	FA	BA	CBA
A01	8.13401	62.7958	98.42	982072.01	3.82	-28.64	-40.29	-36.47
A02	8.13387	62.796	99.35	982071.92	3.85	-28.46	-40.22	-36.37
A03	8.13368	62.7963	101.32	982071.64	3.88	-28.15	-40.14	-36.27
A04	8.13346	62.7966	104.76	982071.06	3.88	-27.69	-40.09	-36.21
A05	8.13324	62.7968	109.5	982070.28	3.87	-27.03	-39.99	-36.11
A06	8.13334	62.7971	113.27	982069.60	3.91	-26.56	-39.97	-36.05
A07	8.13368	62.7973	117.95	982068.72	3.89	-26.02	-39.98	-36.08
A08	8.13402	62.7976	123.13	982067.77	3.97	-25.39	-39.96	-35.99
A09	8.1333	62.7976	127.15	982067.04	3.94	-24.88	-39.93	-35.99
A10	8.1325	62.7976	132.37	982066.08	3.82	-24.22	-39.89	-36.07

A11	8.13142	62.7976	138.14	982065.09	3.73	-23.43	-39.78	-36.06
A12	8.13189	62.7979	143.1	982064.21	3.66	-22.81	-39.74	-36.08
A13	8.13333	62.7983	152.05	982062.55	3.77	-21.73	-39.72	-35.96
A14	8.13311	62.7984	154.8	982062.12	3.71	-21.32	-39.63	-35.92
A15	8.13447	62.7987	166.66	982059.70	3.64	-20.1	-39.82	-36.19
A16	8.13516	62.7989	173.01	982058.50	3.63	-19.36	-39.83	-36.2
A17	8.13476	62.7991	175.92	982058.00	3.5	-18.98	-39.79	-36.29
A18	8.13354	62.7991	180.04	982057.30	3.48	-18.41	-39.71	-36.23
A19	8.13314	62.7994	186.91	982056.12	3.39	-17.48	-39.6	-36.21
A20	8.1327	62.7997	194.44	982054.81	3.35	-16.5	-39.5	-36.15
A21	8.13242	62.8002	204.97	982052.96	3.35	-15.13	-39.39	-36.04
B01	8.13008	62.8156	121.43	982071.03	3.2	-23.97	-38.34	-35.14
B02	8.13131	62.8156	124.63	982070.31	3.33	-23.71	-38.46	-35.13
B03	8.13103	62.8151	124.27	982070.33	3.3	-23.77	-38.48	-35.18
B04	8.13068	62.8147	124.78	982070.21	3.27	-23.7	-38.46	-35.19
B05	8.13036	62.8142	125.92	982069.88	3.27	-23.64	-38.54	-35.27
B06	8.13002	62.8138	126.79	982069.63	3.26	-23.6	-38.6	-35.34
B07	8.12982	62.8134	125.3	982069.80	3.31	-23.85	-38.68	-35.37
B08	8.12933	62.8129	123.93	982070.04	3.29	-24	-38.67	-35.38
B09	8.12898	62.8125	122.62	982070.17	3.32	-24.25	-38.76	-35.43
B10	8.12858	62.8121	122.97	982070.02	3.34	-24.26	-38.81	-35.48
B11	8.12824	62.8118	125.03	982069.68	3.32	-23.94	-38.74	-35.42
B12	8.12741	62.8115	128.24	982069.17	3.23	-23.44	-38.62	-35.39
B13	8.1262	62.8111	133.61	982068.28	3.04	-22.63	-38.44	-35.41
B14	8.12562	62.8103	144.97	982066.14	3.03	-21.22	-38.37	-35.34
B15	8.12475	62.8097	154.55	982064.30	2.97	-20.05	-38.34	-35.37
C01	8.17069	62.8066	40.11	982081.91	5.98	-37.54	-42.29	-36.31
C02	8.17049	62.8069	43.18	982081.45	5.93	-37.07	-42.18	-36.25
C03	8.17051	62.8071	44.6	982081.16	5.96	-36.94	-42.22	-36.26
C04	8.17075	62.8075	47.68	982080.62	5.96	-36.55	-42.2	-36.24
C05	8.17124	62.8077	51.31	982079.74	6.03	-36.33	-42.41	-36.37
C06	8.17166	62.808	55.18	982078.74	6.25	-36.15	-42.68	-36.43
C07	8.1718	62.8082	56.53	982078.40	6.4	-36.09	-42.78	-36.38
C08	8.17119	62.8084	57.4	982078.61	6.32	-35.63	-42.42	-36.1
C09	8.17037	62.8085	59.74	982078.51	6.26	-35.02	-42.09	-35.83
C10	8.16973	62.8087	58.81	982078.80	6.24	-35.02	-41.98	-35.75
C11	8.16908	62.8088	59.25	982078.88	6.24	-34.82	-41.83	-35.59
C12	8.16838	62.809	60.88	982078.51	6.31	-34.7	-41.9	-35.6
C13	8.16787	62.8093	61.84	982078.14	6.53	-34.79	-42.11	-35.58
C14	8.16715	62.8097	57.7	982078.69	6.88	-35.55	-42.38	-35.5
C15	8.16619	62.81	56.25	982078.77	7.06	-35.93	-42.59	-35.53
C16	8.16535	62.81	60.37	982077.89	7.13	-35.55	-42.69	-35.57
C17	8.16457	62.8101	62.18	982077.56	7.18	-35.33	-42.69	-35.51

C18	8.16378	62.8101	65.16	982077.02	7.19	-34.95	-42.66	-35.46
C19	8.16313	62.8101	69.17	982076.33	7.13	-34.4	-42.59	-35.45
C20	8.16239	62.8102	70.97	982076.15	7.03	-34.04	-42.44	-35.41
C21	8.16151	62.8105	71.46	982076.18	6.85	-33.87	-42.33	-35.48
C22	8.16088	62.8104	72.81	982075.97	6.76	-33.66	-42.28	-35.52
C23	8.16036	62.8107	72.03	982076.12	6.73	-33.76	-42.29	-35.56
C24	8.16018	62.8111	69.65	982076.40	6.88	-34.26	-42.5	-35.62
C25	8.15978	62.8116	69.37	982076.18	7.31	-34.6	-42.81	-35.5
C26	8.15925	62.8116	67.54	982076.38	7.14	-34.96	-42.95	-35.81
C27	8.15877	62.8119	64.02	982077.03	7.39	-35.42	-43	-35.61
C28	8.15797	62.8121	64.64	982076.92	7.53	-35.36	-43.01	-35.48
C29	8.15716	62.8121	68.59	982076.15	7.49	-34.91	-43.03	-35.54
C30	8.1564	62.8122	70.3	982075.95	7.47	-34.58	-42.91	-35.44
C31	8.15557	62.8122	73.12	982075.47	7.35	-34.2	-42.85	-35.5
C32	8.15486	62.8123	76.27	982074.95	7.18	-33.75	-42.78	-35.61
C33	8.15403	62.8124	80.16	982074.46	6.88	-33.05	-42.54	-35.66
C34	8.15346	62.8126	81.67	982074.43	6.7	-32.63	-42.3	-35.6
C35	8.15283	62.8129	84.72	982073.93	6.56	-32.21	-42.24	-35.68
C36	8.15248	62.813	86.63	982073.37	6.52	-32.19	-42.44	-35.92
C37	8.15162	62.8133	90	982072.80	6.53	-31.74	-42.39	-35.86
C38	8.15096	62.8136	91.2	982072.53	6.66	-31.66	-42.45	-35.79
C39	8.15031	62.8137	92.13	982072.44	6.54	-31.47	-42.37	-35.83
C40	8.14985	62.8142	91.66	982072.26	6.97	-31.84	-42.69	-35.72
C41	8.14954	62.8144	90.14	982072.35	6.99	-32.22	-42.89	-35.91
C42	8.14859	62.8147	90.95	982072.45	6.88	-31.9	-42.66	-35.78
C43	8.14786	62.815	91.66	982071.98	7.15	-32.17	-43.02	-35.86
C44	8.14673	62.8153	90.35	982072.36	7.17	-32.22	-42.91	-35.74
C45	8.14568	62.8154	91.31	982072.49	6.92	-31.81	-42.61	-35.7
C46	8.14457	62.8156	90.55	982073.19	6.41	-31.35	-42.07	-35.66
C47	8.14354	62.8159	90.17	982073.41	6.21	-31.27	-41.94	-35.73
C48	8.14257	62.8162	90.49	982073.66	6.01	-30.94	-41.65	-35.64
C49	8.14141	62.8164	89.57	982074.20	5.67	-30.7	-41.3	-35.63
C50	8.14	62.8167	98.04	982073.28	5.36	-29.03	-40.63	-35.27
C51	8.13861	62.8171	106.01	982072.07	5.2	-27.81	-40.35	-35.15
C52	8.13705	62.8174	114.96	982070.65	4.93	-26.49	-40.09	-35.16
C53	8.13593	62.8174	122.99	982069.58	4.58	-25.08	-39.63	-35.05
C54	8.13479	62.8168	127.82	982069.10	4.07	-24.03	-39.16	-35.09
C55	8.13322	62.8165	127.24	982069.58	3.71	-23.71	-38.77	-35.06
C56	8.13169	62.8163	122.58	982070.70	3.41	-24	-38.51	-35.09
C57	8.1301	62.816	119.29	982071.52	3.22	-24.18	-38.3	-35.08
C58	8.12888	62.8155	118.79	982071.68	3.1	-24.14	-38.2	-35.09
C59	8.12782	62.8155	117.03	982072.16	3.05	-24.2	-38.05	-35.01
D01	8.14585	62.7999	124.9	982067.43	3.97	-25.35	-40.13	-36.16

D02	8.14572	62.8002	132.54	982066.05	3.94	-24.4	-40.08	-36.14
D03	8.14561	62.8007	144.71	982063.90	3.87	-22.83	-39.96	-36.09
D04	8.14402	62.8008	156.69	982061.79	3.67	-21.25	-39.79	-36.12
D05	8.14298	62.8008	164.14	982060.42	3.54	-20.31	-39.74	-36.2
D06	8.14226	62.801	173.61	982058.72	3.38	-19.11	-39.65	-36.27
D07	8.14222	62.8015	181.4	982057.36	3.34	-18.11	-39.57	-36.23
D08	8.14124	62.802	189.94	982056.01	3.24	-16.85	-39.33	-36.08
D09	8.13965	62.8021	205.86	982052.96	3.26	-15	-39.36	-36.1
D10	8.13923	62.8022	210.36	982052.27	3.27	-14.31	-39.2	-35.93
D11	8.13803	62.8027	222.91	982049.99	3.29	-12.75	-39.13	-35.84
D12	8.13773	62.8029	223.54	982049.87	3.22	-12.69	-39.14	-35.92
D13	8.1383	62.8034	223.57	982049.75	3.2	-12.84	-39.29	-36.09
D14	8.13888	62.8038	223.53	982049.71	3.2	-12.92	-39.37	-36.17
D15	8.13928	62.804	220.41	982050.41	3.16	-13.2	-39.28	-36.12
D16	8.1402	62.8052	209.37	982052.82	3.06	-14.28	-39.06	-36
D17	8.14108	62.8057	214.23	982051.66	3.16	-13.98	-39.33	-36.17
D18	8.14165	62.8065	210.31	982052.71	3.21	-14.19	-39.08	-35.87
D19	8.14213	62.807	210.36	982052.82	3.29	-14.11	-39	-35.7
D20	8.14247	62.8073	210.92	982052.78	3.35	-14	-38.95	-35.61
D29	8.14509	62.8089	204.75	982053.06	3.82	-15.74	-39.97	-36.15
D30	8.14482	62.8095	202.64	982053.52	3.98	-15.98	-39.95	-35.97
D31	8.14458	62.81	200.42	982053.59	4.05	-16.63	-40.35	-36.3
D32	8.14558	62.8107	188.16	982056.01	4.37	-18.05	-40.31	-35.94
D33	8.1473	62.811	174.89	982058.37	4.75	-19.8	-40.5	-35.75
D34	8.14787	62.8114	167.26	982059.50	4.94	-21.06	-40.85	-35.91
D35	8.14888	62.8118	151.95	982062.15	5.23	-23.16	-41.14	-35.91
D40	8.15022	62.8125	124.6	982066.88	5.66	-26.92	-41.67	-36.01
D41	8.15106	62.8127	114.26	982068.56	6.01	-28.44	-41.96	-35.95
D42	8.15239	62.8124	102.56	982070.48	6.28	-30.11	-42.25	-35.96
E01	8.17237	62.8023	2.27	982088.64	5.88	-42.16	-42.43	-36.55
E010	8.16993	62.8036	10.1	982087.65	5.61	-40.84	-42.03	-36.42
E011	8.16996	62.804	12.7	982087.19	5.59	-40.52	-42.02	-36.43
E012	8.16971	62.8042	14.63	982086.93	5.61	-40.2	-41.93	-36.32
E013	8.16956	62.8044	16.9	982086.59	5.63	-39.84	-41.85	-36.22
E014A	8.16976	62.8047	17.64	982086.51	5.69	-39.73	-41.81	-36.13
E015	8.16975	62.8049	19.57	982086.11	5.71	-39.55	-41.87	-36.16
E015A	8.16981	62.8052	21.96	982085.67	5.73	-39.27	-41.87	-36.14
E015B	8.16979	62.8051	20.79	982085.86	5.72	-39.43	-41.89	-36.17
E015C	8.16976	62.8054	22.88	982085.45	5.76	-39.21	-41.92	-36.16
E016	8.1699	62.8055	23.91	982085.19	5.78	-39.17	-42	-36.22
E016A	8.16996	62.8055	26.33	982084.71	5.78	-38.91	-42.02	-36.25
E016B	8.16957	62.8057	27.22	982084.49	5.82	-38.86	-42.08	-36.26
E016C	8.1698	62.8055	25.18	982084.96	5.8	-39.01	-41.99	-36.19

E017	8.17	62.8059	28.67	982084.20	5.84	-38.72	-42.11	-36.28
E017A	8.16999	62.806	31.94	982083.57	5.84	-38.35	-42.13	-36.3
E018	8.17025	62.8063	33.87	982083.15	5.86	-38.2	-42.21	-36.34
E019	8.17062	62.8064	38.43	982082.18	5.96	-37.77	-42.31	-36.36
E03	8.17198	62.8025	2.02	982088.75	5.81	-42.15	-42.38	-36.57
E04	8.1722	62.8027	2.24	982088.67	5.79	-42.17	-42.44	-36.65
E05	8.17218	62.8029	2.37	982088.64	5.75	-42.17	-42.45	-36.7
E06	8.17167	62.8031	3.32	982088.55	5.71	-41.99	-42.38	-36.68
E07	8.17121	62.8033	5.58	982088.20	5.68	-41.65	-42.31	-36.64
E08	8.17072	62.8034	7.32	982088.04	5.65	-41.29	-42.15	-36.51
E09	8.17009	62.8035	8.28	982087.98	5.64	-41.06	-42.04	-36.4
E20	8.17143	62.8023	3.19	982088.60	5.84	-41.91	-42.29	-36.45
E21	8.17101	62.8019	7.13	982087.90	5.84	-41.37	-42.21	-36.38
E22	8.17073	62.8016	11.74	982087.06	5.8	-40.77	-42.16	-36.36
E23	8.17018	62.8015	14.17	982086.63	5.74	-40.44	-42.12	-36.37
E24	8.16941	62.8016	16.05	982086.36	5.66	-40.13	-42.03	-36.37
E25	8.16867	62.8015	17.4	982086.12	5.64	-39.95	-42.01	-36.38
E26	8.16794	62.8014	19.5	982085.72	5.62	-39.69	-42	-36.38
E27	8.17053	62.8014	13.44	982086.70	5.79	-40.59	-42.18	-36.39
E28	8.1715	62.8013	11.05	982087.03	5.94	-40.99	-42.3	-36.37
E29	8.17248	62.8013	9.04	982087.26	6.05	-41.37	-42.44	-36.39
E30	8.17348	62.8012	8.16	982087.25	6.16	-41.66	-42.62	-36.46
E31	8.17448	62.8012	8.07	982087.13	6.23	-41.8	-42.76	-36.53
E32	8.17542	62.8012	8.87	982086.79	6.3	-41.89	-42.94	-36.65
E33	8.17618	62.8011	10.67	982086.28	6.37	-41.84	-43.1	-36.73
E34	8.16708	62.8011	22.08	982085.18	5.69	-39.42	-42.04	-36.35
E35	8.16642	62.8008	25.28	982084.62	5.59	-38.97	-41.96	-36.38
E36	8.16585	62.8004	27.63	982084.04	5.58	-38.8	-42.07	-36.5
E37	8.16549	62.8	31.26	982083.21	5.6	-38.47	-42.17	-36.58
E38	8.16479	62.7997	33.28	982082.69	5.58	-38.35	-42.29	-36.72
E39	8.16432	62.7993	35.43	982082.12	5.64	-38.23	-42.42	-36.77
E40	8.16404	62.7988	37.65	982081.67	5.78	-37.95	-42.41	-36.63
E41	8.16283	62.7986	41.14	982081.17	5.61	-37.37	-42.23	-36.62
E42	8.16201	62.7986	43.34	982080.84	5.54	-37.01	-42.14	-36.6
E43	8.16137	62.7988	45.62	982080.44	5.38	-36.73	-42.13	-36.75
E44	8.16046	62.7987	48	982080.05	5.32	-36.38	-42.06	-36.74
E45	8.15968	62.7986	50.35	982079.75	5.26	-35.93	-41.89	-36.64
E46	8.15903	62.7985	52.72	982079.43	5.18	-35.53	-41.77	-36.59
E47	8.15827	62.7981	55.41	982078.84	5.17	-35.26	-41.82	-36.65
E48	8.15765	62.798	57.98	982078.40	5.12	-34.89	-41.75	-36.63
E49	8.15696	62.7977	60.21	982077.98	5.09	-34.61	-41.73	-36.64
E50	8.15619	62.7976	62.04	982077.70	5.06	-34.31	-41.65	-36.59
E51	8.15556	62.7975	64.29	982077.40	5.01	-33.91	-41.52	-36.51

E52	8.15458	62.7976	66.8	982077.29	4.9	-33.25	-41.16	-36.26
E53	8.15423	62.7979	68.01	982077.18	4.86	-33.01	-41.06	-36.2
E54	8.15425	62.7982	69.93	982076.99	4.79	-32.63	-40.9	-36.12
E55	8.15468	62.7986	72	982076.69	4.71	-32.32	-40.84	-36.13
E56A	8.15507	62.799	74.55	982076.23	4.64	-32.02	-40.85	-36.21
E57	8.15456	62.7989	76.02	982076.07	4.61	-31.73	-40.72	-36.12
E58	8.15395	62.7989	77.6	982075.80	4.59	-31.5	-40.69	-36.1
E59	8.15297	62.7987	80.51	982075.32	4.54	-31.07	-40.6	-36.05
E60	8.15206	62.7985	83.22	982074.80	4.48	-30.74	-40.59	-36.11
E61	8.15116	62.7984	85.94	982074.26	4.39	-30.43	-40.6	-36.21
E62	8.15026	62.7983	88.09	982073.93	4.33	-30.09	-40.52	-36.19
E63	8.14936	62.7981	90.87	982073.43	4.24	-29.72	-40.48	-36.24
E64	8.1489	62.7977	93.73	982072.84	4.18	-29.4	-40.49	-36.32
E65	8.14853	62.7974	95.42	982072.45	4.15	-29.25	-40.54	-36.39
E66	8.14784	62.7971	97.74	982071.97	4.09	-28.99	-40.56	-36.46
E67	8.14768	62.7973	97.11	982072.22	4.07	-28.95	-40.44	-36.37
E68	8.14754	62.7975	97.78	982072.18	4.04	-28.8	-40.37	-36.33
E69	8.14738	62.7978	98.61	982072.14	4.03	-28.6	-40.27	-36.23
E70	8.14728	62.798	99.72	982072.02	4.03	-28.39	-40.2	-36.17
E71	8.14716	62.7982	101.29	982071.78	4.02	-28.16	-40.15	-36.13
E72	8.147	62.7984	102.97	982071.52	4.01	-27.92	-40.11	-36.1
E73	8.14683	62.7986	104.58	982071.24	4.01	-27.71	-40.09	-36.08
E74	8.14667	62.7988	106.99	982070.80	4	-27.43	-40.09	-36.09
E75	8.14666	62.7991	110.31	982070.15	3.99	-27.07	-40.13	-36.14
E76	8.14652	62.7993	113.59	982069.61	3.98	-26.61	-40.06	-36.08
E77	8.14627	62.7995	117.84	982068.88	3.98	-26.05	-40	-36.02
E78	8.14601	62.7997	122.16	982068.08	3.98	-25.53	-39.99	-36
F01	8.14723	62.797	98.5	982071.83	4.06	-28.88	-40.54	-36.48
F02	8.14627	62.7969	98.89	982071.74	4.03	-28.84	-40.55	-36.52
F03	8.14529	62.7967	99.59	982071.66	4	-28.7	-40.49	-36.49
F04	8.14432	62.7966	100.08	982071.59	3.98	-28.61	-40.45	-36.47
F05	8.14339	62.7965	100.96	982071.51	3.96	-28.42	-40.36	-36.4
F06	8.14244	62.7964	101.47	982071.47	3.94	-28.28	-40.29	-36.35
F07	8.1415	62.7962	101.04	982071.46	3.93	-28.41	-40.37	-36.44
F08	8.14062	62.796	100.76	982071.53	3.92	-28.42	-40.34	-36.42
F09	8.14038	62.7955	101.17	982071.43	3.95	-28.35	-40.33	-36.38
F10	8.14378	62.7962	101.74	982071.28	3.96	-28.38	-40.42	-36.46
F11	8.14381	62.796	103.02	982070.98	3.96	-28.26	-40.45	-36.49
F12	8.14393	62.7958	102.89	982070.94	4	-28.33	-40.5	-36.51
F13	8.14395	62.7955	102.14	982071.06	4.03	-28.42	-40.51	-36.48
F130	8.14471	62.7916	121.46	982066.84	4.85	-26.39	-40.76	-35.91
F131	8.14364	62.7912	123.16	982066.50	4.91	-26.17	-40.75	-35.84
F132	8.14186	62.7908	127.11	982065.79	4.8	-25.65	-40.69	-35.89

F133	8.13973	62.7903	130.67	982065.25	4.68	-25.05	-40.51	-35.84
F14	8.14402	62.7953	100.54	982071.21	4.09	-28.75	-40.65	-36.56
F15	8.14407	62.7951	101.63	982071.18	4.11	-28.43	-40.46	-36.35
F16	8.14412	62.7949	102.34	982070.97	4.13	-28.41	-40.52	-36.39
F17	8.14419	62.7946	102.63	982070.88	4.16	-28.39	-40.53	-36.37
F18	8.14425	62.7944	102.88	982070.78	4.21	-28.39	-40.57	-36.36
F19	8.14434	62.7942	103.58	982070.62	4.24	-28.32	-40.58	-36.33
F20	8.14429	62.794	104.55	982070.43	4.27	-28.19	-40.56	-36.29
F21	8.14437	62.7938	105.93	982070.11	4.31	-28.07	-40.61	-36.3
F22	8.14442	62.7936	107.52	982069.87	4.36	-27.81	-40.53	-36.18
F23	8.14445	62.7934	108.99	982069.59	4.39	-27.61	-40.51	-36.12
F24	8.14468	62.7932	109.77	982069.42	4.46	-27.54	-40.53	-36.07
F25	8.14484	62.7929	110.87	982069.20	4.53	-27.4	-40.52	-35.99
F26	8.14499	62.7927	112	982068.90	4.6	-27.33	-40.58	-35.98
F27	8.14514	62.7925	113.18	982068.62	4.68	-27.23	-40.62	-35.94
F28	8.14525	62.7922	114.92	982068.23	4.75	-27.07	-40.67	-35.91
F29	8.14527	62.792	117.33	982067.70	4.81	-26.83	-40.72	-35.91
H01	8.13776	62.79	132.77	982064.87	4.6	-24.75	-40.46	-35.87
H02	8.13808	62.7896	136.56	982064.05	4.7	-24.37	-40.53	-35.83
H03	8.13822	62.7892	140.17	982063.25	4.81	-24.03	-40.62	-35.81
H04	8.13843	62.7888	145.51	982062.03	4.94	-23.57	-40.78	-35.85
H05	8.13865	62.7883	151.46	982060.67	5.08	-23.06	-40.98	-35.9
J01	8.13446	62.7956	98.55	982071.84	3.8	-28.75	-40.41	-36.61
J02	8.13422	62.7955	98.36	982071.88	3.8	-28.77	-40.41	-36.62
L01	8.12772	62.8154	122	982072.01	3.03	-22.82	-37.26	-34.22
L02	8.12254	62.8201	120	982072.87	3.12	-22.92	-37.12	-34
L03	8.12006	62.8255	134	982070.30	3.5	-21.57	-37.42	-33.92
L04	8.12013	62.8289	112	982074.06	3.93	-24.85	-38.1	-34.17
L05	8.12672	62.8116	138	982069.43	3.01	-20.17	-36.5	-33.49
L06	8.12084	62.8076	156	982066.81	2.71	-16.94	-35.4	-32.69
L07	8.1192	62.8026	143	982067.36	2.59	-20.04	-36.96	-34.37
L08	8.12037	62.7964	107	982072.57	3.28	-25.47	-38.14	-34.86
L09	8.12406	62.793	95	982074.02	3.72	-27.48	-38.72	-35
L10	8.15694	62.7961	67.52	982076.57	5.45	-33.63	-41.63	-36.17
L11	8.17304	62.8006	22	982084.77	6.11	-39.82	-42.42	-36.31
L12	8.18526	62.7999	17	982084.91	7.27	-41.17	-43.18	-35.91
L13	8.20174	62.7981	11	982083.98	6.88	-43.82	-45.12	-38.24

MAGNETIC DATA ACQUISITION

Magnetic data have been acquired along a series of profiles crossing two segments of the MTFC (Fig. A 6). In total, fifteen profiles were measured: Profiles 1 to 8 are located across the proposed location of the Tjellefjonna fault and Profiles 10 to 15 across the Fannefjorden fault. Profile 9 is located in between the two segments to study the existence of possible minor faults related to the larger segments (Fig. A 6). The measurements were conducted using an advanced GEM magnetometer GSM-19 with two sensors separated vertically by 56 cm in order to measure vertical gradients and the total magnetic field simultaneously (Fig. A 7). The magnetometer records the magnetic field and gradient in different modes. We used the Walkgrad mode to measure vertical gradient and magnetic field continuously. The data acquisition is done with 5 Hz. To correct for the effect of diurnal variations a second magnetometer was deployed in the area. The base magnetometer was located close to the survey area. We used a Scintrex ENVI-MAG magnetometer and set up it to record the magnetic field every 5 seconds continuously during the day (Fig. A 8). Two locations for the base stations were used (Fig. A 6). Base 2 was used for Profile 8 only. The coordinates of the base stations are shown in Table A 4.

Magnetic data processing

A significant number of power lines and different infrastructures (pipes, houses, etc.) exist in the survey area. Therefore, relatively high noise levels were recorded along some of the profiles. Such high-amplitude noise overprints the anomalies related to geological structures and must be removed before processing. During the measurements the location of the infrastructures was noted (Table A 5), but additional structures in the subsurface (e.g., pipelines) could exist. Cultural noise sources such as barbed-wire

fences were also noted. Some parts of the profiles had to be completely disregarded due to a high-noise level. The magnetic data were further corrected for diurnal variations using the base station readings, and the International Geomagnetic Reference Field 2005 (IGRF 2005) was removed.
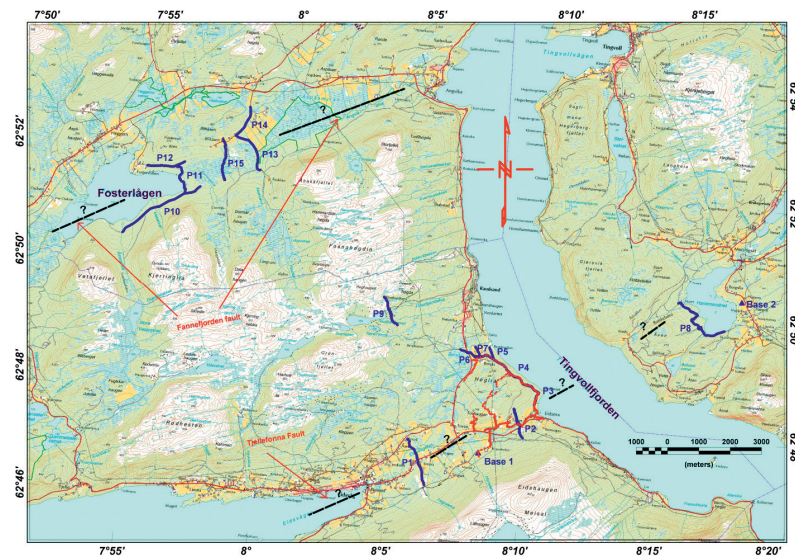
Fig. A 6 Gravity and magnetic surveys depicted as red dots and blue lines, respectively. Base stations for magnetic measurement are indicated with blue triangles. The proposed segments of the MTFC, Tjellefonna and Fannefjorden faults, are shown with the dashed, black line.

Fig. A 7 GSM-19 V magnetometer used here as portable magnetometer.

Fig. A 8 ENVI_MAG magnetometer used here as base magnetometer.

Table A 4 Base stations used for the magnetic survey

Base Station	Longitude	Latitude
Base 1	08.08.17	62.47.21
Base 2	08.17.32	62.50.23

Table A 5 Locations of power lines and other kind of infrastructures

Profile	X (Degree)	Y (Degree)	Descriptions
L.1	8.06.03	62.47.07	Buildings
L.1	8.05.39	62.47.26	Buildings
L.1	8.05.36	62.47.27	Buildings
L.1	8.05.33	62.47.27	Buildings and power lines
L.1	8.05.27	62.47.27	Road and some pipe lines
L.2	8.09.44	62.47.47	Electric fence
L.2	8.09.43	62.47.48	Road and power line
L.2	8.09.43	62.47.54	Road and power line
L.3	8.10.13	62.48.26	Pipeline
L.3	8.10.12	62.48.22	Pipeline
L.3	8.10.12	62.48.20	Pipeline
L. 3	8.10.11	62.48.19	Pipeline
L.3	8.10.17	62.48.28	Pipeline
L.3	8.10.13	62.48.26	Pipeline
L.6	8.08.09	62.49.02	Strong power line
L.6	8.07.32	62.49.03	Metallic bridge
L.8	8.15.34	62.50.11	Agricultural equipments
L.10	7.54.07	62.50.28	Bridge-this part is removed
L.10	7.55.04	62.50.55	Pipeline
L.10	7.55.11	62.50.57	Pipeline
L.12	7.54.46	62.51.39	Buildings-this part is removed
L.13	7.58.50	62.52.02	Power line
L.13	7.58.23	62.52.17	Power line
L.13	7.58.52	62.51.49	Parking place
L.14	7.58.23	62.52.39	Power line
L.14	7.58.00	62.52.22	Power line

Magnetic results

Diurnal variations, reduced magnetic data, and the vertical gradient of the total magnetic field are presented for the individual profiles in Fig. A 9 to Fig. A 23. The corrections, for all the profile are less than 15 nT which means that the survey has been carried out under relatively quiet magnetic conditions. In the reminder we present the profiles and discuss the most significant anomalies.

Profile 1

This profile is conducted to cross the suspected fault zone (Tjellefonna fault) perpendicularly. Because of the presence of power lines and other kinds of infrastructures we skipped measurements along sections (1) and (3) (Fig. 9b). Number (2) indicates a low magnetic anomaly with a short wavelength probably related to a powerline. Fig. A 9c shows the vertical gradient. Numbers (1) and (3) outline the skipped sections. Anomaly number (2) is probably the effect of a power line and anomaly number (4) is related to some near-surface infrastructure. No anomaly could be clearly related to a fault segment.
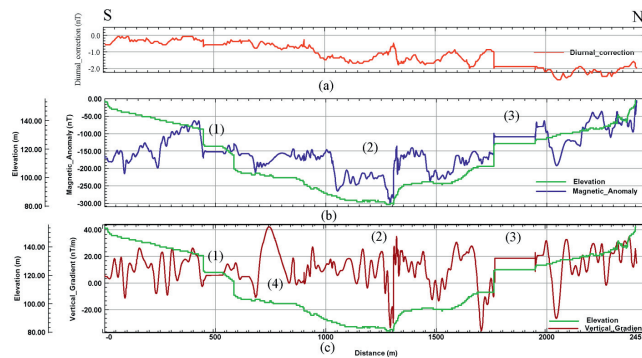
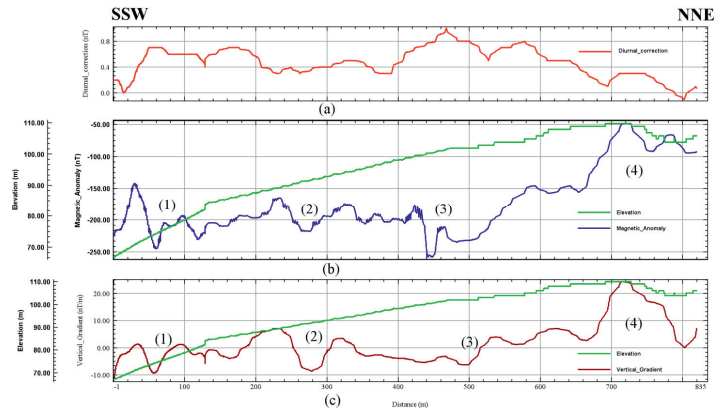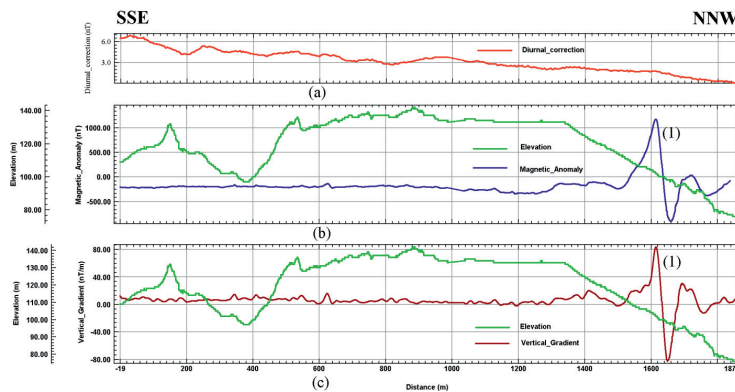*Fig. A 9 Magnetic profile 1 (a) Diurnal variation of the total magnetic field of the Earth during the measurements, (b) magnetic anomaly and (c) vertical gradient of total magnetic field.*

Profile 2

This profile is almost 1500 meter long and located ~2 km west of Eidsøra. The profile crosses through a densely forested valley. We expected to cross the fault perpendicularly. Magnetic anomalies are shown in Fig. A 10b. Due to field conditions very high frequency signals were recorded. In order to remove the high frequency noise (short wavelength) a low-pass filter was applied to the recorded magnetic anomalies

(Fig. A 10c). Afterwards, an anomaly with amplitude of 80 nT can be clearly distinguished (number (1) in Fig. A 10c). This anomaly is probably related to brittle structures present in the bedrock. A section numbered (2) represents a part of the profile which has been skipped because of a road crossing. The vertical gradient appears to be relatively noisy (Fig. A 10d). The reason for this is the rugged topographic path followed by the operator across the forest and implying inevitable changes in magnetometer height.
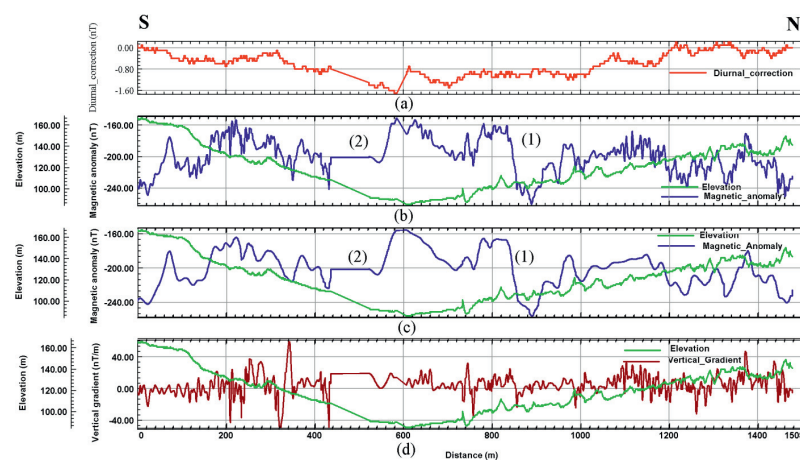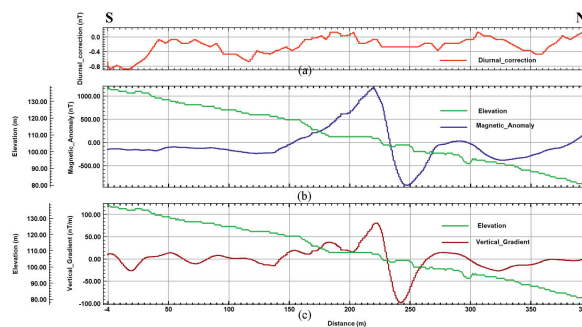

Fig. A 10 Magnetic profile 2, (a) Diurnal variation of the total magnetic field of the Earth during the measurements, (b) magnetic anomaly and (c) vertical gradient of total magnetic field.

Profile 3

This profile is ~840 meter long and located near Eidsøra (Fig. A 6). Pronounced magnetic anomalies were detected ((1), (2), (3) and (4) in Fig. A 11b). NE of anomaly (3), magnetic values increase gradually whereas SW of it they remain relatively constant. The vertical gradient shows the same anomalies as represented by the total magnetic field.

Fig. A 11 Magnetic profile 3, (a) Diurnal variation of the total magnetic field of the Earth during the measurements, (b) magnetic anomaly and (c) vertical gradient of total magnetic field.

Profile 4

This profile is almost 1800 m long and is located near Eidsøra. A very high-amplitude magnetic anomaly of 1500 nT is seen along this profile (Fig. A 12b). This anomaly is probably related to the presence of an amphibolite body. An outcrop of this highly magnetic body has been detected along this profile. A similar anomaly, but with smaller amplitude, is also seen on the vertical gradient of the magnetic field (Fig. A 12c).
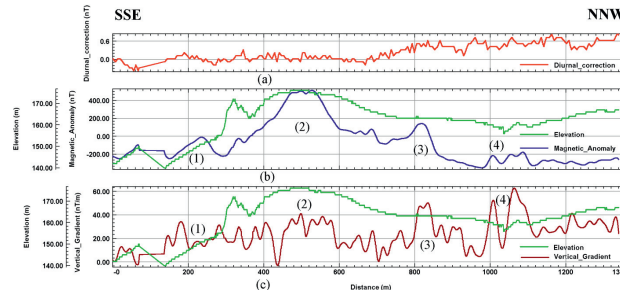

Fig. A 12 Magnetic profile 4, (a) Diurnal variation of the total magnetic field of the Earth during the measurements, (b) magnetic anomaly and (c) vertical gradient of total magnetic field.

Profile 5

This profile is 400 meter long. The aim here was to focus on the high amplitude magnetic body (Fig. A 13). Here, the anomaly is located in the middle of the profile and very pronounced with an amplitude of 1500 nT. This anomaly could be caused by a magnetite rich body. The magnetic values adjacent to the anomaly are similar, which points to a homogeneous geological background. In addition, the shape of the anomaly resembles very much the ones commonly associated to magnetized dykes.
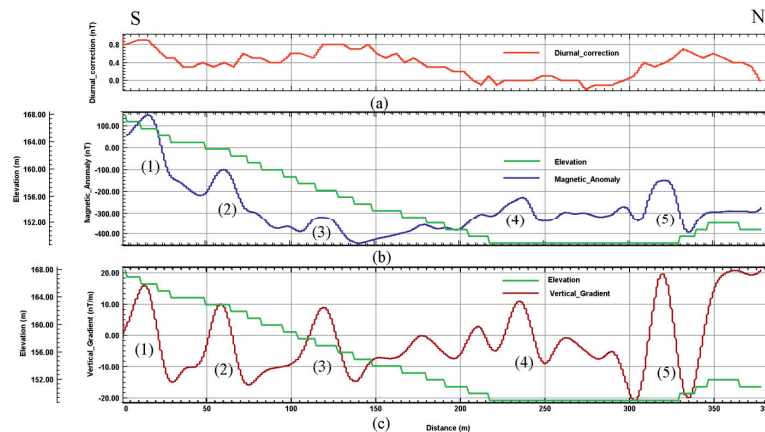

Fig. A 13 Magnetic profile 5, (a) Diurnal variation of the total magnetic field of the Earth during the measurements, (b) magnetic anomaly and (c) vertical gradient of total magnetic field.

Profile 6

This profile starts at the southern end of Profile 4 (Fig. A 6). Diurnal variations in the Earth's magnetic field were negligible during the recording time (Fig. A 14a). Four distinct anomalies can be detected. A very high amplitude magnetic anomaly number (2) with a symmetric shape is shown in Fig. A 14b (number (2)). This anomaly is probably related to the same structure which has already been mentioned for Profiles 4 and 5 but here it has a symmetric shape. There are some other magnetic anomalies labeled (1), (3) and (4) in Fig. A 14b. Vertical gradient values remain positive all along the profile which emphasis the symmetric anomalies. All magnetic anomalies except anomaly (1) find their counterparts in the variations of the vertical gradient.
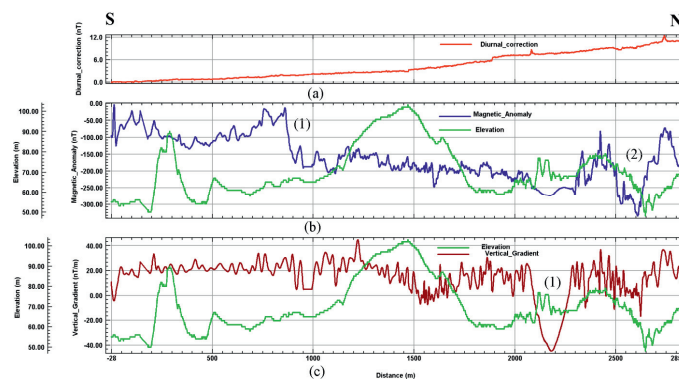
Fig. A 14 Magnetic profile 6, (a) Diurnal variation of the total magnetic field of the Earth during the measurements, (b) magnetic anomaly and (c) vertical gradient of total magnetic field.

Profile 7

This profile was conducted parallel to profile 5 (Fig. A 15). Fig. A 15 shows several magnetic anomalies. By comparing the variations in magnetic values and topography we clearly see that the magnetic trend from anomaly number (1) to (3) is influenced by the topography. The vertical gradient shows similar anomalies (Fig. A 15c).
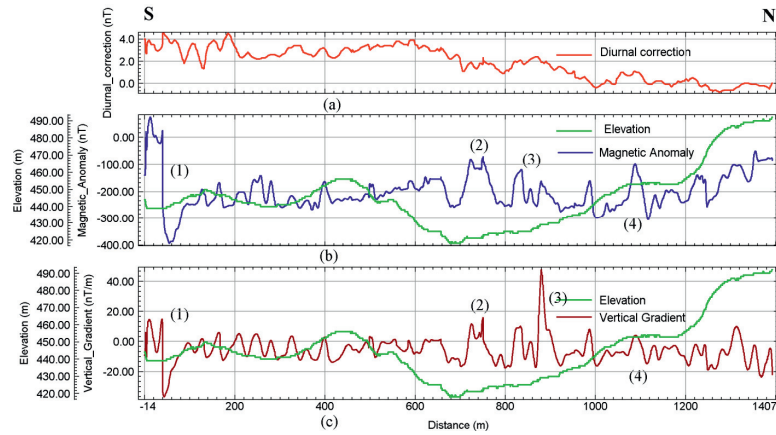

Fig. A 15 Magnetic profile 7, (a) Diurnal variation of the total magnetic field of the Earth during the measurements, (b) magnetic anomaly and (c) vertical gradient of total magnetic field.

Profile 8

This profile is located on the eastern side of Tinvollfjorden (Fig. A 6). The magnetic signal along this specific profile is used to constrain interpretations derived from other geophysical methods like resistivity and seismics. Diurnal variations of the magnetic field are less than 12 nT (Fig. 4.16a). Two pronounced anomalies are seen in

Fig. A 16b. Anomaly number (1) shows a step in the magnetic field where the higher value in the southern part is well isolated. Anomaly number (2) is expressed as a depression. The vertical gradient along the profile is very noisy (Fig. A 16c) and this casts some doubts on the significance of the pronounced anomaly seen close to the southern end of the profile. Anomaly number (1) is due to technical problems during recording data and does not reflect a geological anomaly.
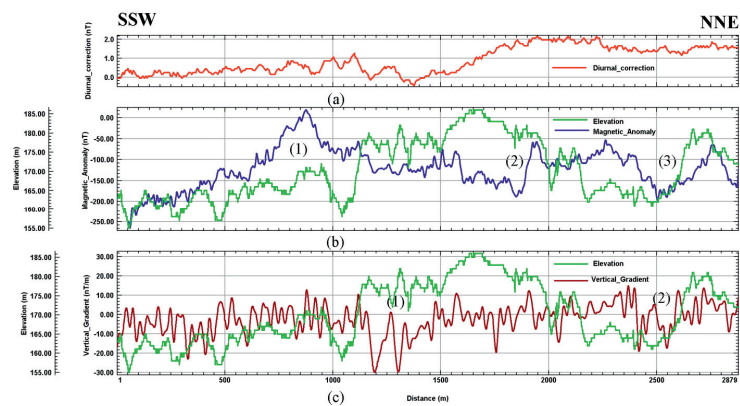

Fig. A 16 Magnetic profile 8(a) Diurnal variation of the total magnetic field of the Earth during the measurements, (b) magnetic anomaly and (c) vertical gradient of total magnetic field.

Profile 9

This Profile is located at relatively high altitudes (i.e. 400-500 m a.s.l., Fig. A 17). Diurnal variations for the Earth magnetic field during the measurements were in the order of 5 nT (Fig. A 17a). A very distinctive anomaly is observed at the beginning of the profile (No. (1), Fig. A 17b) with an amplitude of almost 400 nT. There are also some other modest anomalies. Fig. A 17c shows the vertical gradient of the magnetic field where we can observe the same anomalies as in the magnetic total field. The source of these anomalies is probably located in the shallow subsurface as the anomalies show high amplitudes and short wavelengths.
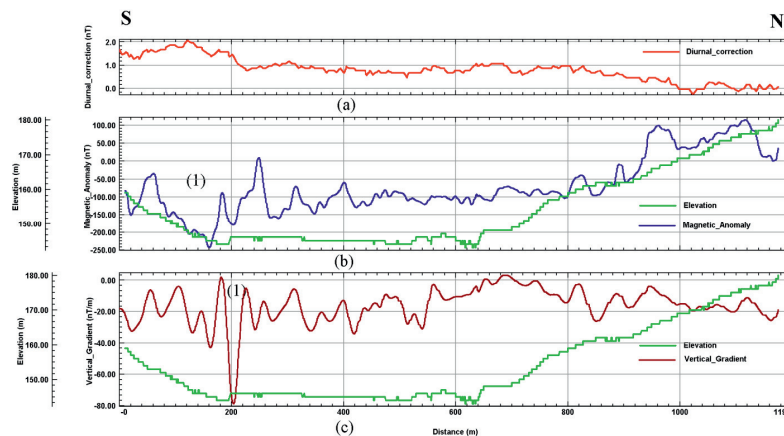
Fig. A 17 Magnetic profile 9. (a) Diurnal variation of the total magnetic field of the Earth during the measurements, (b) magnetic anomaly and (c) vertical gradient of total magnetic field.

Profile 10

This profile is almost 3 km long and is located on the southern shore of the Fosterlågen Lake (Fig. A 18). This profile is following a road with very gentle topography. Three anomalies are depicted in Fig. A 18b. Although the vertical gradient appears to be very noisy, we could isolate two distinct anomalies which are numbered (1) and (2). Gradient anomaly number (2) finds its counterpart in the magnetic anomalies in contrast to anomaly number (1), which is probably related to a shallow source body.
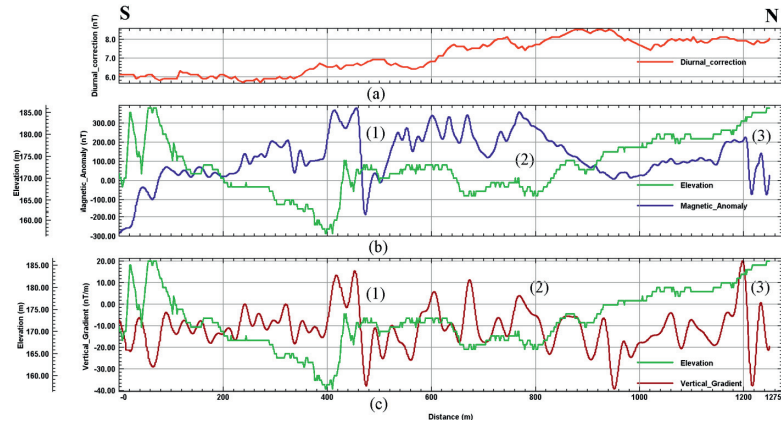

Fig. A 18 Magnetic profile 10, (a) (a) Diurnal variation of the total magnetic field of the Earth during the measurements, (b) magnetic anomaly and (c) vertical gradient of total magnetic field.

Profile 11

This profile strikes almost S-N (Fig. A 19) and is located on the eastern shore of the Fosterlågen Lake. The location of the profile should cross the Fannefjorden fault perpendicularly. A low magnetic anomaly can be isolated with some smaller anomalies nearby ((1) in Fig. A 19b). This profile shows an increase of the anomalies from profile 800 m towards its northern end. In the vertical gradient profile an anomaly with amplitude 80nT/m is distinguished which has its counterpart in the magnetic anomaly. The width of the anomaly indicates a shallow source location (Fig. A 19c).
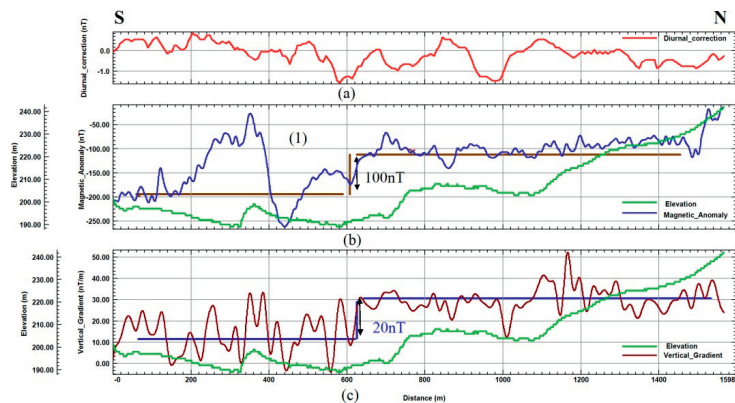

Fig. A 19 Magnetic profile 11, (a) Diurnal variation of the total magnetic field of the Earth during the measurements, (b) magnetic anomaly and (c) vertical gradient of total magnetic field.

Profile 12

This profile strikes W-E and is located northeast of Fosterlågen Lake (Fig. A 6). An anomaly of ~400 nT is seen in Fig. A 20b (i.e. number (1)). The vertical gradient (Fig. A 20c) shows various anomalies. Three high amplitude anomalies correlate with the magnetic anomalies isolated in Fig. A 20b. Anomaly numbered (3) shows a very short wave-length and probably is related to a very shallow or non-geologic structure.

Fig. A 20 Magnetic profile 12, (a) Diurnal variation of the total magnetic field of the Earth during the measurements, (b) magnetic anomaly and (c) vertical gradient of total magnetic field.
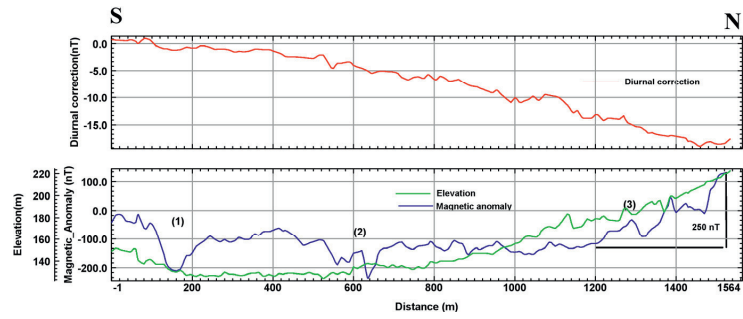
<u>Profile 13</u>

The profile is almost 1600 meter long and runs parallel to Profile 11 and should cross the Fannefjorden fault. Diurnal variations of the Earth's magnetic field do not exceed 3 nT during the measurements of this profile (Fig. A 21a). An anomaly with an amplitude of 200 nT is seen ((1) in Fig. A 21b). Interpretation of the variations in the vertical gradient appears to be hampered by a high noise level (Fig. A 21b, c). Nevertheless both magnetic anomaly and vertical gradient show a step in magnitude that can be related to a fault with a significant vertical displacement.

Fig. A 21 Magnetic profile 13, (a) Diurnal variation of the total magnetic field of the Earth during the measurements, (b) magnetic anomaly and (c) vertical gradient of total magnetic field.

Profile 14

This profile is the continuation of Profile 13. The modest diurnal variations (i.e. less than 2 nT) are shown in Fig. A 22a. Different magnetic anomalies can be isolated (Fig. A 22b). The vertical gradient shows two distinct anomalies with higher amplitudes ((2) and (6) in Fig. A 22c). These two anomalies find their counterparts in the total magnetic field but their amplitude are much more pronounced in the vertical gradient indicating shallow source bodies.

Fig. A 22 Magnetic profile 14, (a) Diurnal variation of the total magnetic field of the Earth during the measurements, (b) magnetic anomaly and (c) vertical gradient of total magnetic field.

Profile 15

This profile is located parallel to Profile 13 to verify the anomaly along the latter. Due to a problem with GPS, we were not able to record the profile continously. For diurnal correction data from base magnetometer at Rørvik (RVK) have been used. The station at Rørvik is part of the geomagnetic reference network for Norway (WWW.tgo.uit.no)

Fig. A 23 shows the measurement results. Three anomalies can be detected: (1) is parallel to the anomaly in Profile 13 and its shape and amplitude (200 nT) are similar. (3) depicts an increase in magnetic value which can also be detected in Profile 13. This anomaly with 250 nT amplitude might be related to a fault.

Fig. A 23 Magnetic profile 15, (a) Diurnal variation of the total magnetic field of the Earth during the measurements, (b) magnetic anomaly.

Appendix B

2D resistivity profiling and shallow refraction data acquisition

The measurements were conducted in 2007 and 2008. In total, one refraction seismic profile with a total length of 1320 m and seven 2D resisistivity profiles with lengths between 800 and 1800 m were acquired in the study area (Fig. B 1). Resistivity profiles 1,4,5, and 7 were measured in areas with rough topography, potentially hinting on of the message of fault segments of the MTFC. GPS has been used for positioning, and the profiles are roughly orientated SSE to NNW, which is perpendicular to the assumed strike of the MTFC. The location of the refraction seismic profile coincides with the resistivity profile 7.
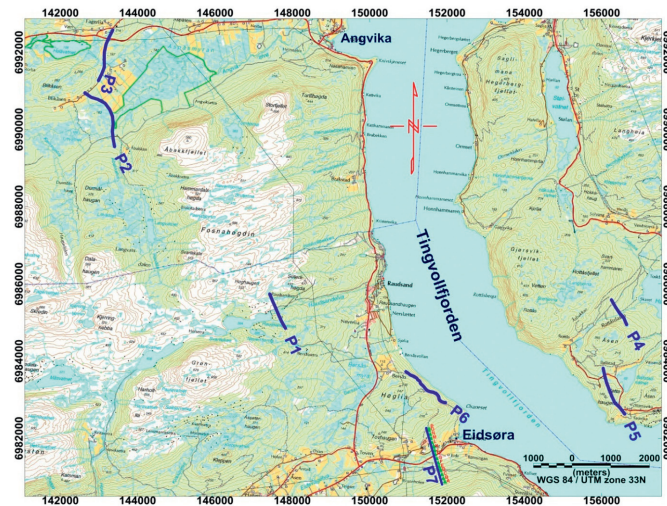
Fig. B 1. Topographic map of the study area with locations of the resistivity profiles (blue lines) and the refraction profile (green line).

Results of 2D resistivity surveys

The results of the data inversion are shown in Fig. B 2 to B 8. As mentioned in chapter 2 of this thesis, resistyivity data processed and inverted by using the RES2DINV (version 3.55) software (Loke 2004). There are different electrode configurations for resistivity measurement which offer advantages and disadvantages

compared to each other in terms of logistics and resolution, and the choice is usually a trade-off between these factors. In this study we used the so-called gradient array electrode configuration. This electrode configuration is well-suited for multi-channel data acquisition systems, so that many data-points can be recorded simultaneously for each current injection, so as to reduce fieldwork time significantly without compromising the data density (Dahlin & Zhou, 2002). Further details about data acquisition can be found in Nasuti et al. (2009).

Profile 1

The first profile has a length of 1000 meters and is located in between the mapped fault segments, but on relatively high elevation with a distinct topography. Four low resistivity zones can be detected by looking at the inverted data which are numbered (1) - (4) (Fig. B 2). The low resistivity zones (2) and (4) have a dip between 45 and 50 degrees towards the south. Low-resistivity zone (3) is almost vertical with a potential northern dip. Low resistivity zone (1) is located t the southern end of the profile and its dip is not resolved.
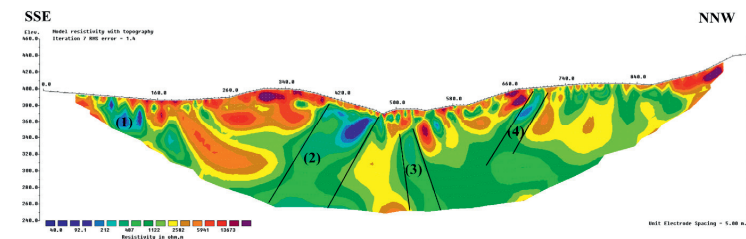
Fig. B 2. Resistivity profile 1. Numbers indicate the low resistive zones. See Fig. B 1 for profile location.

Profile 2

The profile is 1800 meters long and located perpendicular to one of the main segments of the MTFC. The inverted data shows three low-resistivity anomalies and a pronounced low-resistivity layer at the top of the section (Fig. B 3). The latter corresponds to water saturated sediments. The numbered low resistivity anomalies on the profile relate potentially to weak zones caused by the tectonic activity of the MTFC.
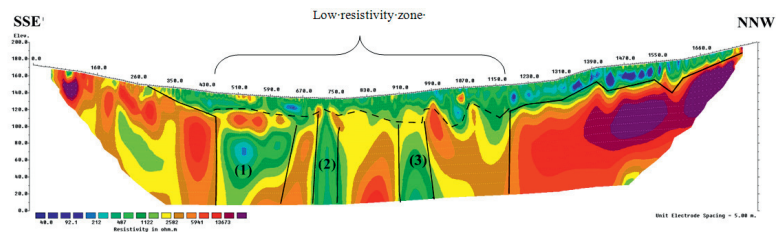
Fig. B 3 Resistivity profile 2. Numbers indicate the low resistive zones, the solid lines depict bedrock boundaries and the dashed line represents the assumed top of the bedrocks where they are not well imaged. See *Fig. B 1* for profile location.

Profile 3

The profile has a length of 1400 meters and is an extension to the north of Profile 2. Except a shallow low-resistivity layer at the top, the resistivity along the profile is resistive and there is not an obvious anomaly that could be distinguished in the inverted data. This indicates that the MTFC is probably located further south, at the location of Profile 2.
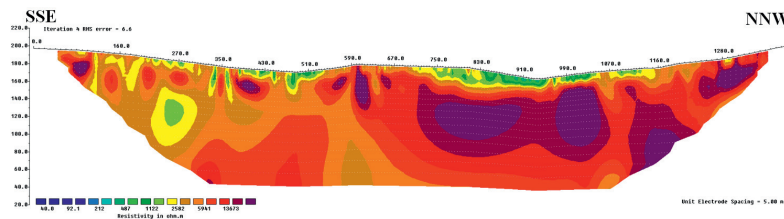
Fig. B 4. Resistivity profile 3. See Fig. B 1 for profile location

Profile 4

This profile is located at the eastern side of Tingvollfjorden and has a length of 800 meters. The profile is located in a depression (Fig. B 5). Between the northern and southern part a large resistivity contrast is observed, which can be interpreted as a signal related to the fault or a sudden contrast in lithology in the basement. An anomaly numbered (1) is probably an artifact which results from the limitation of the method.
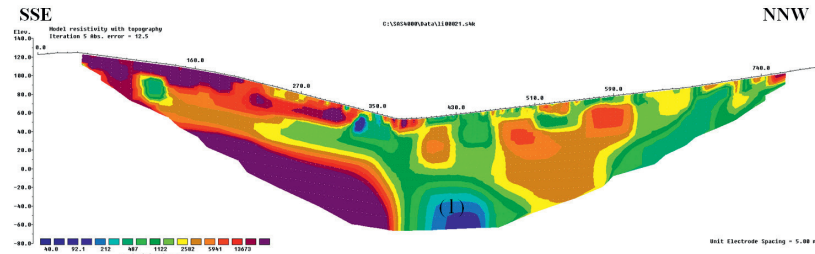
Fig. B 5. Resistivity profile 4. See Fig. B 1 for profile location.

Profile 5

This profile is 1400 meters long and was carried out in a rough topographic setting, and is the prolongates of profile 4, but with a lateral offset of almost 1000 m. The resistivity profile shows three very low anomalies: two of them are very shallow (no. (1) and (2) in Fig. B 6). The first low resistivity zone is located at the southern end of the profile. No information about its depth extension can be derived. The third zone is clearly extending to depth, but should be interpreted carefully, as it is located close to the lower boundary of the resistivity model. Both zones cannot be clearly linked to segments of the MTFC.
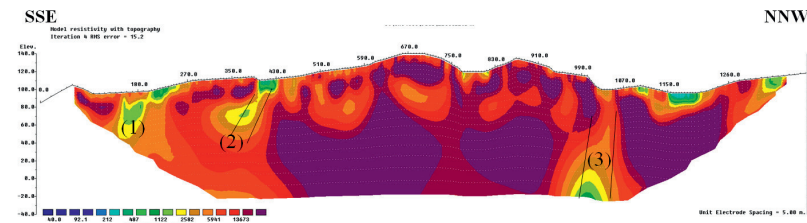
Fig. B 6 Resistivity profile 5. Numbers indicate the low resistive zones. See Fig. B 1 for profile location.

Profile 6

Profiles 6 and 7 are located in the area of Eidsøra, where geological and topographic evidence is given for the existence of a segment of the MTFC (Fig. B 7). Profile 6 has a length of 1400 m and a series of small-scale low resistivity anomalies. This implies many fractures and crushed zones in the bedrock. The profile is located along a road and we can correlate outcrops with the resistivity profile. The zones indicated by numbers (1), (2) and (3) are due to their width and depth extensions, the most likely candidates for anomalies associated with segments of the MTFC.
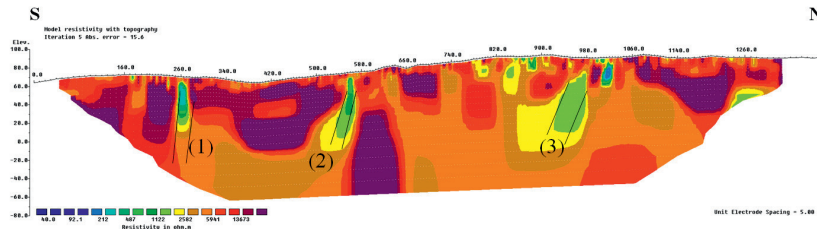
Fig. B 7 Resistivity profile 6. Numbers 1, 2, and 3 indicate the low resistive zones. See Fig. B 1 for profile location.

Profile 7

The profile is almost a continuation of Profile 6 with a slight lateral offset (Fig. B 8) and has a length of 1400 m. The resistivity profile shows a zone of low resistivity close to the surface, which represents water-saturated sedimentary or weathered layer. This layer is separated from the high resistive bedrock as marked by a dashed line (compacted till; Fig. B 8). Low-resistivity zone (1) is located at the southern end of the profile which there no information about its extension to depth can be found. The other low resistivity zones show almost a fault dip towards south. Both zones can potentially be linked to weakness zones of the MTFC.
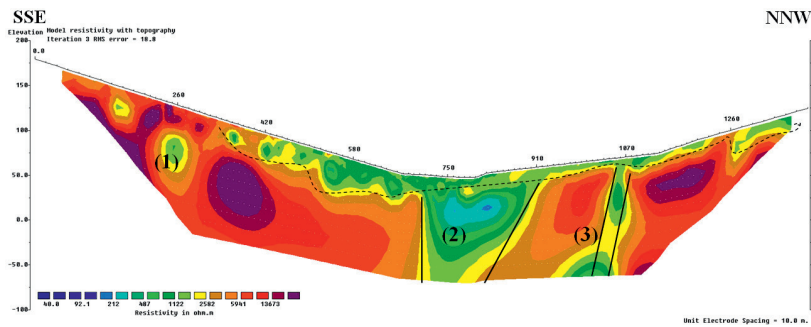
Fig. B 8 Resistivity profile 7. Numbers indicate the low resistive zones, solid lines depict bedrock boundaries and the dashed line separates high resistive fresh bedrock from a low resistivite sedimentary or weathered layer. For profile location see Fig. B 1

REFRACTION SEISMICS

Field work

As mentioned before a 1320 m long refraction seismics profile with almost SSE to NNW strike was measured across the anticipated main fracture zone in the Eidsøra region, along resistivity Profile 7. The data was acquired in October 2007 with the seismics recording system ABEM TERRALOC MK6 with 24 channels (Fig. B 9). The profile was measured with two seismics cables, each with 12 geophone connections. Geophone spacing was 10 m, except at the end of the cables where the spacing was reduced to 5 m. To resolve dipping structures, it becomes necessary to carry out both forward and reverse shooting in order to determine all the parameters required to solve for the reflector geometry (Reynolds 1997).

Fig. B 9 The seismics recording system ABEM TERRALOC MK6.

Five shots were performed each day with distances of (1) 5 meters to the first geophone, (2) 110 meters to the first shot along the profile backwards, (3) of 110 m to the first geophone, (4) 5 meters to the last geophone, and, finally, (5) 110 meters to the last geophone along the profile. This measuring system was repeated six times along the profile line to get full coverage of the length. Totally 32 shot points have been gathered along the profile. Energy source for the shootings was ordinary dynamite with electrical ignition. For short distances we used 100 grams of dynamite, for larger distances from the geophones up to 200 grams have been used. Table B 1 lists the coordinates of the shot points and Fig. B 10 shows the shot locations.

Table B 1 Location of shot points along the seismics profile

Shot points name on the map	Distance from starting point of profile (m)	WGS 84 (UTM zone 32) E	WGS 84 (UTM zone 32) N	Elevation (m)
A	-110	457548.00	6962649.00	204
B	-5	457500.00	6962735.00	177
C	110	457454.00	6962836.00	154
D	220	457406.00	6962938.00	132
E	330	457361.00	6963028.00	109
F	440	457328.00	6963125.00	88
G	550	457284.00	6963232.00	67
H	660	457236.00	6963333.00	52
J	770	457202.00	6963429.00	49
K	880	457171.00	6963524.00	55
L	990	457119.00	6963635.00	70
M	1100	457083.00	6963739.00	83
N	1210	457055.00	6963843.00	98
O	1320	457017.00	6963943.00	117
P	1370	457010.00	6963984.00	125
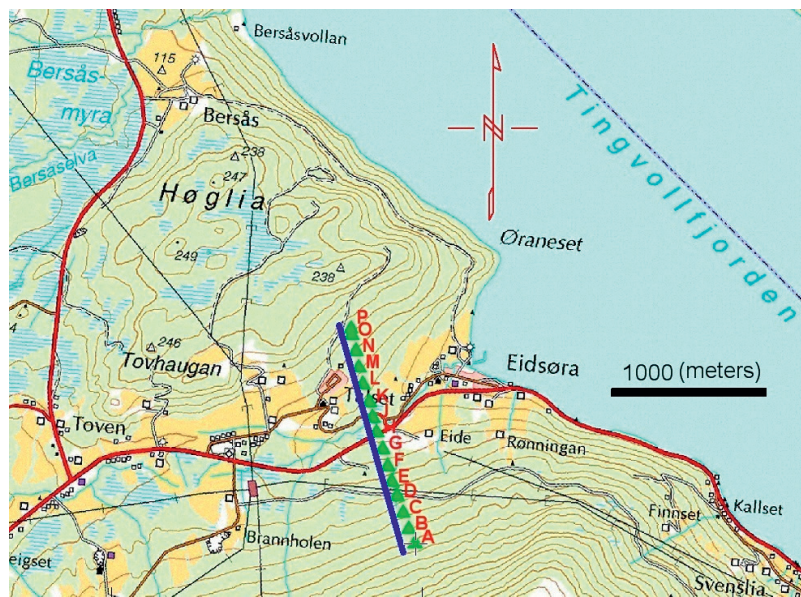
Fig. B 10. Location of the refraction profile. The shot points are shown with green triangles. Letters refer to Table B 1 Location of shot points along the seismics profile. The resistivity Profile 7 is shown in blue.

Processing and interpretation of the refraction seismic profile

The first step in processing/interpreting refraction seismics data is to pick the arrival times of the signal, called first break picking. A plot is then made showing the arrival times against the distance between the shot and geophone. This is called a time-distance graph (Fig. B 11 – B 16). The travel time curves are made by using the well-known ABC-method (Hawkins, 1961), which implies a systematic summation of arrival times from forward and reverse recordings. The method was originally based on a common point on the ground surface and two separate points on the refractor, yielding an average depth. The classical plus-minus method (Hagedoorn, 1959) is used for estimating seismic velocities and layer thickness in combination with estimating layering and thickness from intercept times and crossover distances. The interpretation based on these methods is shown in Fig. B 17.
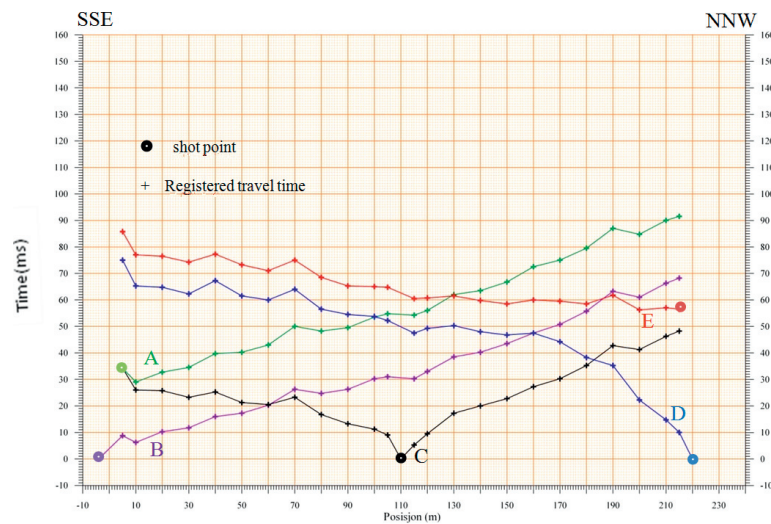
Fig. B 11 Travel times for shot points along the first segment. Different colours show the recorded time for different shot points (see Table b 1 and Fig. B 10). The horizontal axis shows the distance from the starting point of the profile.
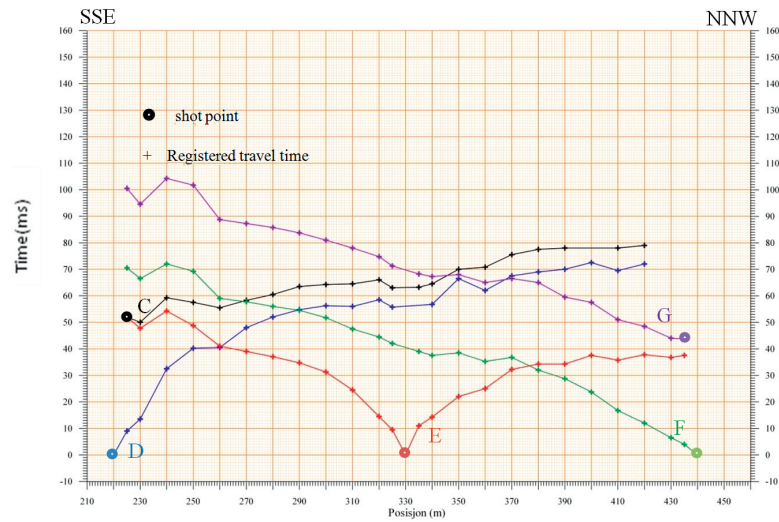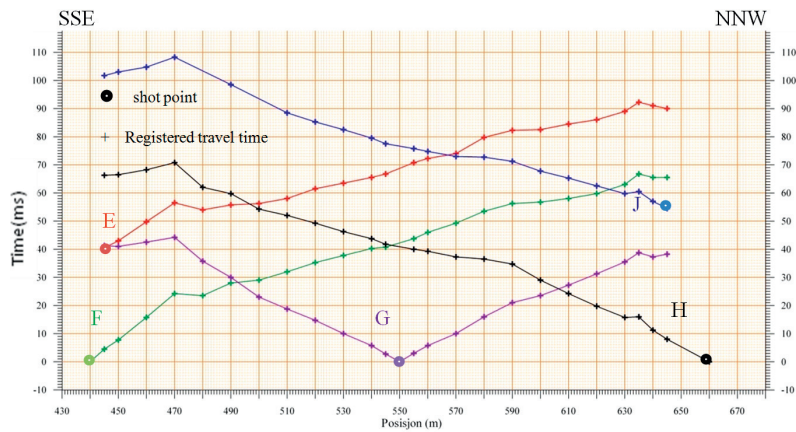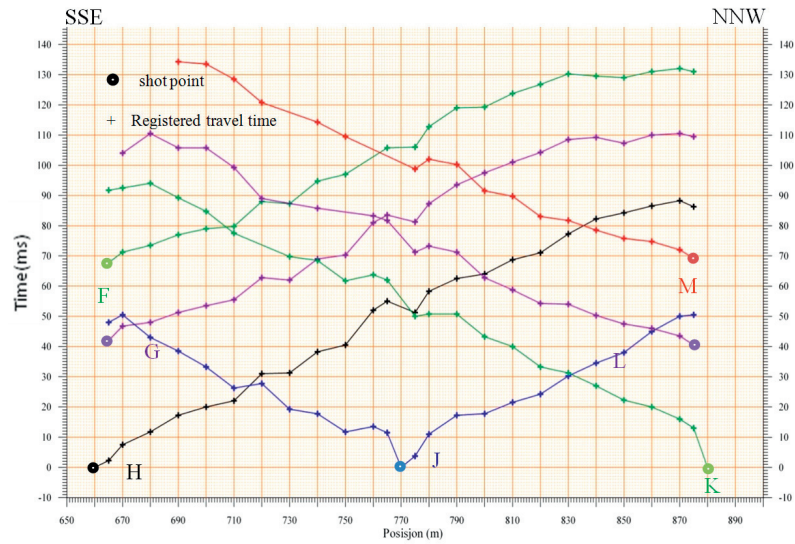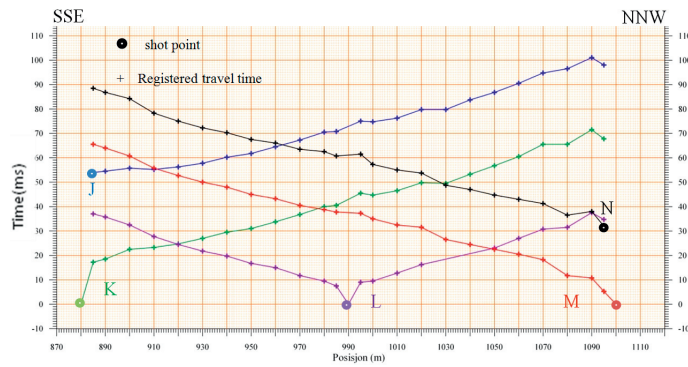
Fig. B 12 Travel times for shot points along the second segment. Different colours show the recorded time for different shot points (see Table B 1 and Fig. B 10). The horizontal axis shows the distance from the starting point of the profile.
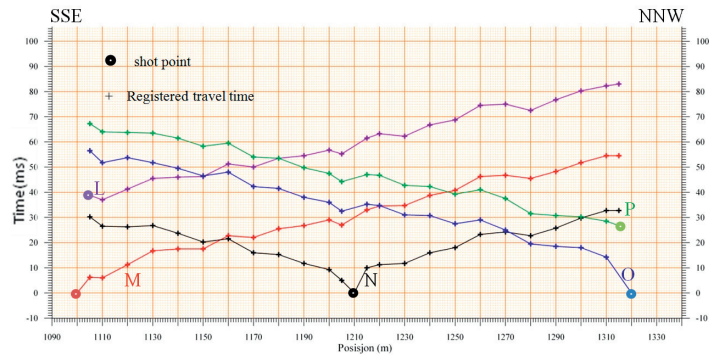

Fig. B 13. Travel times for shot points along the third segment. Different colours show the recorded time for different shot points (see Table b 1 and Fig. B 10). The horizontal axis shows the distance from the starting point of the profile.

Fig. B 14 Travel times for shot points along the fourth segment. Different colours show the recorded time for different shot points (see Table b 1 and Fig. B 10). The horizontal axis shows the distance from the starting point of profile.

Fig. B 15 Travel times for shot points along the fifth segment. Different colours show the recorded time for different shot points (see Table b 1 and Fig. B 10). The horizontal axis shows the distance from the starting point of profile.

Fig. B 16 Travel times for shot points along the sixth segment. Different colours show the recorded time for different shot points (see Table b 1 and Fig. B 10). The horizontal axis shows the distance from the starting point of the profile.
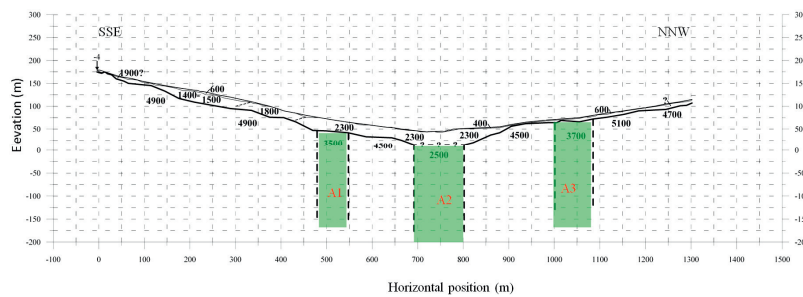

Fig. B 17 Interpreted section along the refraction profile. Velocities of layers are shown in bold numbers in m/s. The profile is corrected for terrain effects. A1, A2 and A3 show the low velocity zones along the profile. The low velocity zones are interpreted to have vertical extension, as no information about the dip or the depth can be obtained from our refraction experiment.

The conducted shallow refraction profile has a length of 1300 m (Fig. B 17). The bottom of the valley has an elevation of 44-45 m (asl) and is located 700-750 m from the starting point of the profile. The first point of the profile is located at height 179 m asl and the last point at 115 m (asl). The bedrock along the profile is covered by superficial deposits of different kinds and thicknesses. Horizontal distances from the starting point of the profile will be used for describing all anomalies and specific positions.

Three different layers can be distinguished in the seismics interpretation (Fig. B 17). At the top a layer of 0.5-5.0 m thickness with very low seismic velocity (400-600 m/s) exists, which represents dry deposits of sand/gravel or loose till. In some places this layer is dominated by swampy bog and peat. In the underlying bedrock seismic

velocity is very variable. Along the central lower part of the profile (450-900 m) the velocity is about 2300 m/s, which could relate to very compact till. Towards the south the velocity is 1800 m/s and decreases to 1400-1500 m/s between 150 and 320 m. The highest value is interpreted as till-dominated deposits, while the lower values can relate to sorted material of sand and gravel (glaciofluvial deposits). The total thickness of the superficial deposits between position 155 m and 870 m along the profile is varying from 15 to about 30 m. In the northern part of the profile the thickness varies from 3 to max. 12 m, and the smallest values are shown at position 905-940 m. Seismic velocity in the third layer, which is interpreted as bedrock, is varying from 2500 to 5100 m/s. Low values (less than 4000 m/s) indicate areas of fractured or crushed bedrock.

There are indications of three distinct low-velocity zones in the bedrock denoted as A1-A3 along the profile. The main zone (with velocities as low as 2500 m/s) is about 110 m wide and is located below the central part of the profile (position 690-800 m). The very low velocity is caused by intensive fracturing and crushing of the bedrock. Another zone is located 200 m north of the main zone and is about 80 m wide (position 1000-1080 m). The seismic velocity is estimated to 3700 m/s and indicates less fracturing than in the main zone. A similar zone is located about 140 m south of the main zone (position 430-550 m) with a width of 70 m and a seismic velocity of 3500-m/s. The seismic velocity of the bedrock in between the low-velocity zones is about 4500 m/s, while it is 4900 m/s in the southern part of the profile and 4700-5100 m/s in the northern part.

Appendix C

Petrophysical laboratory measurements

Rock sampling and petrophysical measurements on densities, magnetic susceptibilities, and seismic velocities provides important constraints for the geophysical models. Detailed analysis of fault rocks and a better field coverage of the target areas will significantly improve our knowledge of the past rheological evolution of the fault segments and will help to interpret the nature of the damage zones imaged by geophysical tools. The rock sampling for the petrophysical measurements was carried out in connection with the geophysical field experiments and reconnaissance fieldwork. The rock samples were partly analysed at the NTNU (P- and S-velocities) and NGU and ETH (magnetic susceptibility, densities) laboratories. The density and susceptibility of the rock samples were measured by Andrea Biedermann in the context of her master thesis (see details in Biedermann, 2010). The results of this study were used for constraining the 2D model of the Tjellefonna fault (see chapter 4 of the thesis).

P- and S- wave velocities

Velocity measurements were made on rock samples that were collected in the study area in the framework of the project. The samples consist mainly of gneisses and amphibolites typical for the area. Samples 1 to 8 were collected along a seismic profile (chapter 6) following the southwestern shore of Tingvollfjorden (Fig. C 1).

If the rock is isotropic, homogeneous, and linearly elastic then there are only two possible types of waves which can travel through the rock: 1) a compressional, acoustic or sonic wave (P-wave) and 2) a shear wave (S-Wave).

The velocity measurements of both compressional, Vp, and shear wave, Vs were carried out in the SINTEF laboratory using the Pulse Transmission method. Pulse transmission is a simple technique for measuring the velocity of waves through rocks, fluids, and other materials.

Fig. C 1 The locations of rock samples for velocity measurements. Small triangles show the rock samples and the red line shows the reflection seismic profile 2 that was acquired in this project (chapter 6).

A schematic layout of the method is shown in Fig. C 2 (Malhotra & Carino, 2004). The instruments in are shown in Fig. C 3. The transducer in this configuration acts as a transmitter. When a voltage is applied to the piezoelectric crystals, they expand creating a mechanical or acoustic wave. Waves propagate through the sample and impinge on the piezoelectric crystals at the opposite side of the sample. The distortion causes the active crystal to output a voltage which is amplified and digitized or recorded on the oscilloscope and stored in the computer. If we start the recording precisely when the voltage is applied to the transmitted crystal and then measure the time, Δt, required to traverse a sample of length, L, we can calculate the associated velocity.

$$V = L/\Delta t$$

This velocity corresponds to either a compressional wave if we excite the P-wave transducer or a shear wave if we excite the S-wave transducer. We note from Fig. C 1 that part of the path from transmitter to receiver is through the end caps. Since we are only interested in the speed through the sample, the transit times through the end caps must be subtracted from the total travel time to derive at the travel time through the sample, Δt:

$$\Delta t = \Delta t_{total} - \Delta t_{endcap}$$

The result of the velocity measurements are shown in Table D1. As this table shows only the results for P-waves we only use one subscript because the wave

propagation is in the same direction of particle motions. For example Vpx means the P-wave that propagates in X direction and the displacements of the particle inside the rock are also in the X direction. When S-waves are subjected to a rock, particles move up and down, or side-to-side--perpendicular to the direction that the wave is traveling in (the direction of wave propagation). Consequently, we denoted the S velocities by Vs_{ij}. The first subscript i indicates the propagation direction, and the second subscript j indicates the polarization direction of the shear wave.

The measured velocities have been used for constraining the seismic reflection profile. Details of the seismic survey can be found in chapter 6.
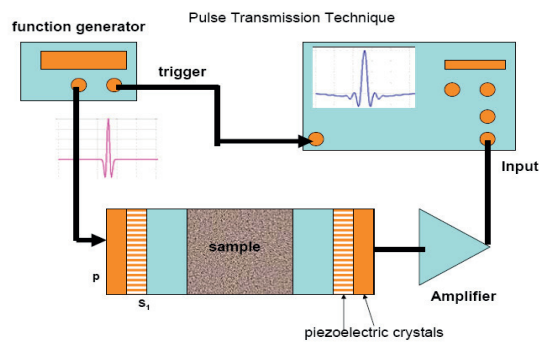
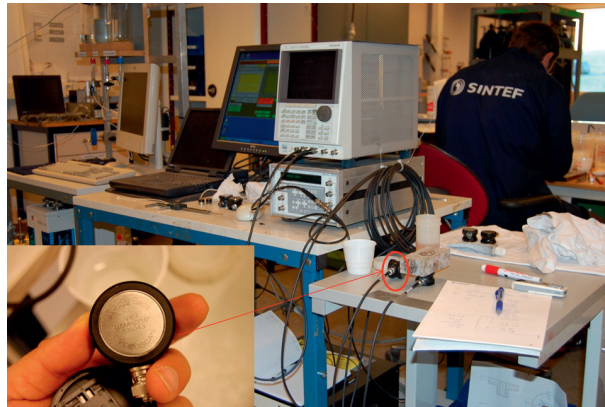*Fig. C 2 A scheme of the Pulse Transmission configuration (http://ic3db.ou.edu/ic3/ic3/index.htm)*
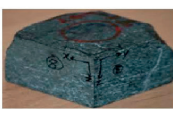
Fig. C 3 Velocity measurements in Sintef laboratory. Pulse Transmission configuration is shown.

Table C1. Velocity and anisotropic properties of collected samples in Eidsøra. ε and γ are Thomsen parameters for anisotropy (Thomsen, 1986). The Parameter ε is essentially the difference between the P-wave velocities in the horizontal and vertical direction. Similarly, parameter γ is essentially the fractional difference between the S-wave velocities in the horizontal and vertical directions for a medium.

Rock	Lithology	Coordinates UTM 32 N WGS 84	P- and S-Velocities	Anisotropic parameter
	Amphibolite	X=459282 Y=6963338	Vpx=6411 m/s Vpz=4557 m/s Vs,xy=3850 m/s Vs,zy=3200 m/s	ε= 0.4896 γ= 0.2238
	Gneiss	X=457723 Y=6964413	Vpx=5120 m/s Vpy=4380 m/s Vs,yx=2750 m/s Vs,zx=3155 m/s	ε = 0.1832 γ = 0.1581
	Gneiss	X=457723 Y=6964413	Vpy=5076 m/s Vpz=4330 m/s Vs,xz=2515 m/s Vs,zy=2808 m/s	ε = 0.1871 γ = 0.1233
	Mafic	X=456075 Y=6965811	Vpy=6300 m/s Vpz=5600 m/s Vs,xy=3486 m/s Vs,zy=3195 m/s	ε = 0.1328 γ = 0.0952
	Gneiss	X=456075 Y=6965811	Vpx=5691 m/s Vpy=4644 m/s Vs,xy=3200 m/s Vsy=?? m/s	ε = 0.2509 γ = ??
	Gneiss	X=456936 Y=6964952	Vpy=5468 m/s Vpz=4180 m/s Vs,yz=2830 m/s Vs,xy=1795 m/s Vs,yx=3256 m/s	ε = 0.3556 γ = 0.1619
	Gneiss	X`=455122 Y=6963656	Vpy=4950 m/s Vpz=4391 m/s Vs,xy=2981 m/s Vsy=2575 m/s	ε = 0.1354 γ = 0.1701
	Amphibolite	X=455181 Y=6964475	Vpx=6800 m/s Vpy=6400 m/s Vpz=??? m/s Vsz=??? m/s	??

References

Biedermann, A.R., 2010. Magnetic Properties of the Møre–Trøndelag Fault Complex. MSc Thesis, ETH Zürich. http://e-collection.library.ethz.ch/view/eth:1986.

Dahlin, T. and Zhou, B., 2002: Gradient and mid-point-referred measurements for multichannel 2D resistivity imaging, *Procs. 8th Meeting Environmental and Engineering Geophysics, Aveiro, Portugal, 8-12 September 2002*, 157-160.

Hagedoorn J.G. 1959: The plus-minus method of interpreting seismics refraction sections. Geophysical Prospecting 7, 158-182.

Hawkins, L.V., 1961, The Reciprocal method of routine shallow seismics refraction investigations: *Geophysics*, **26**, 806–819.

Loke, M. H., 2004: Tutorial: 2-D *and 3-D electrical imagining surveys*. 136 p.

Nasuti, A., Chawshin, K., Dalsegg, E., Tønnesen, J.F., Ebbing, J. and Gellein, J., 2009. Electrical resistivity and refraction seismics over a segment of the Møre-Trøndelag Fault Complex. *Norges geologiske undersøkelse report* 2009.037, 37p.
    http://www.ngu.no/upload/Publikasjoner/Rapporter/2009/2009_037.pdf

Malhotra, V.M. & Carino, N.J., 2004, Handbook on Nondestructive Testing of Concrete 2nd ed. Chapter 8, CRC Press , Boca Raton, Florida.

Reynolds, J. M., 1997: An Introduction to Applied and Environmental Geophysics: John Wiley & Sons.

Thomsen, L., 1986: Weak elastic anisotropy: Geophysics, Soc. Of Expl. Geophys., 51, 1954-1966.